A Thesis submitted to the University of Leoben for the degree of Doctor of
Philosophy in Mining and Metallurgical Sciences

Investigation of particle attraction by steel/refractory and steel/gas interfaces and the associated relevance for clogging in casting processes

presented by

Uxía Diéguez Salgado

Leoben, June 2018

Para ellos

Affidavit

I declare in lieu of oath, that I wrote this thesis and performed the associated research myself, using only cited in this volume.

Uxía Diéguez Salgado

Leoben, 14th June 2018

Acknowledgments

Foremost, I would like to express my deepest gratitude to my Ph.D. supervisor Ao. Univ. Prof. Christian Bernhard. Firstly, for giving me the opportunity to work into his M2CC group and introduce me into the Ferrous Metallurgy world and secondly, for his motivation, trust, and excellent acceptance during the past four years. Because I did not only learn about clogging or other related topics but to put effort and not give up. I also want to thank Ao. Univ. Prof. Christian Weiss, who has been a great discussion partner. His precise work and explanations and the support received have really helped me to write this thesis. My sincere thank you to Ao. Univ. Prof. Susanne Michelic, for her support and motivation, especially in the difficult moments of the investigation.

I should not forget all the colleagues from the Ferrous Metallurgy department. Without them, this experience and the success of this work would not have been the same. Thank you!

The financial support by K1-Met GmbH is gratefully acknowledged. K1-Met is a member of COMET – Competence Center for Excellent Technologies and is finally supported by the Austrian ministries BMVIT, BMVITJ, the provinces of Upper Austria, Styria and Tyrol, SFG and Tiroler Stiftung. COMET is managed by FFG (Austrian research promotion agency).

Por último, no me puedo olvidar de toda esa gente que me ha apoyado desde lejos durante estos cuatro años. Porque para ellos esto es casi tan importante como para mí. Porque, aunque esté lejos ellos saben que estoy ahí. ¡Gracias por vuestra paciencia! As well deserve my recognition, the ones who were here supporting and listening to me every day. This is not only my achievement but as well yours. Special thanks to Amina and Silvia. Not to forget all the people who I have met the past four years, maybe just for short period of time but always with a lesson to learn.

'*However difficult life may seem, there is always something you can do and succeed at. It matters that you just don't give up'*

Contents

Abstract

Clogging in continuous casting of steel is the buildup of particles in the flow control system. Besides other reasons, pre-existing non-metallic inclusions (NMIs) - mostly resulting from ladle treatment - may build up on the refractory wall, interrupting or disturbing the fluid flow conditions. Since the NMIs in the steel cannot be completely avoided, a deeper understanding of their development and evolution during the steelmaking process is required. In particular, this includes the deposition of micro-inclusions to the steel/refractory interface in the submerged entry nozzle (SEN) between the tundish and the mold.

The deposition mechanism for deoxidation products at the SEN wall is investigated in **Chapter 1**. The inclusions, which are transported from the bulk melt to the boundary layer, may adhere to the steel/refractory interface. If they are not removed due to detachment forces related to the fluid flow and materials conditions, they sinter inducing changes on the process and product conditions. The interfacial properties of the system NMI-steel-refractory are believed to play a key role in the NMIs adhesion or detachment at the steel/refractory interface. The clogging mechanism and the forces involved in the adhesion of NMI at the wall are presented. And furthermore, several clogging countermeasures are commented.

In **Chapter 2**, the clogging evaluation methods are summarized. The methods are classified into direct and indirect. While direct methods investigate SEN-samples from industrial plan trials or laboratory scale experiments, the indirect methods analyze isolated related clogging parameters**,** such as the interfacial properties of the system NMI-steel-refractory. In this work, the high-temperature laser scanning confocal microscopy (HT-LSCM) has been selected as a qualitative method to investigate how the wettability of the system NMI-steel-refractory affects the clogging problem. For that purpose, a two-step set-up has been developed. The finality of this experimental investigation is the observation of:

- **(1)** The effect of the NMIs wettability in the deposition of NMIs at a steel/ceramic interface
- **(2)** The effect of the ceramic wettability in the deposition of NMIs at a steel/ceramic interface.

The selected methodology shows a high potential to predict how an interfacial property such as wettability influences the NMI separation tendency at certain refractory interfaces. The results are compared with a theoretical model. Furthermore, high-temperature drop shape analyses (HT-DSA) are performed to confirm the correspondence between the HT-LSCM observations and the wettability.

A detailed model is derived to predict the critical conditions needed for detachment of NMIs from the nozzle wall in **Chapter 3**. This model is based on the local hydrodynamic conditions combined with the specific interfacial properties in the system NMI-steel-refractory. Three detachment criterions are developed in function of the force balances in normal and parallel directions and the torque moment of the NMI at the steel/refractory interface. The detachment model is implemented to investigate how the interfacial properties of the system NMI-steel-refractory may influence the adhesion or detachment of a NMI at the steel/ceramic interface.

The injection of argon gas at the flow control area of the SEN is performed during continuous casting to reduce clogging problems. The behavior of the argon bubbles at the steel/refractory interface and the deposition mechanism of NMI at the steel/gas interface is investigated and commented in **Chapter 4**. Two detachment criteria are developed to investigate the following:

(1) The size of bubbles that may be stable at the steel/refractory interface, and
(2) the detachment of NMIs from the bubbles once they adhere at the steel/gas interface.

The role of argon in the system is discussed in comparison with the model developed for the adhesion of deoxidation products at the steel/refractory interface.

Finally, the relevance of certain clogging parameters onto the NMIs deposition at steel/refractory and steel/gas interfaces is presented on **Chapter 5**. The clogging countermeasure selection is discussed.

1 Clogging

In this chapter, the clogging phenomena are defined and classified following literature sources. The deposition mechanism of non-metallic inclusions (NMIs) coming from steel deoxidation at the nozzle wall is investigated in detail. The analysis of the separation and adhesion steps is the focus of the following work. The NMIs separate at the steel/refractory interface in order to reduce their interfacial energy. They adhere at this interface by a fluid bridge formation and are subjected as well to detachment forces. To finalize this chapter, the most typical clogging countermeasures are introduced. Only the methods related with the decrease of the adhesion force by the modification of the interfacial properties of the system "NMI-Steel-Refractory" are discussed.

NMIs are substances with non-metallic character with different chemical composition compared to the surrounding matrix. A sharp interface is formed between inclusions and matrix. Principally they can be characterized according to the subsequent four criteria[1–3]:

(1) **By source**:
   a) *Endogenous* inclusions: Particles resulting from reactions inside the steel melt, during cooling or during solidification.
   b) *Exogenous* inclusions: Particles intruded from outside, e.g. small parts of refractory material, entrapped slag droplets or particles from reoxidation of the steel by atmosphere.

(2) **By size**:
   a) *Macro* inclusions ($\geq 100\mu m$);
   b) *Meso* inclusions ($\geq 15\mu m$ to $< 100\mu m$);
   c) *Micro* inclusions ($\geq 1\mu m$ to $< 15\mu m$);
   d) *Submicro* inclusions (< 1 µm).

(3) **By type**: When categorizing by type, the nonmetal acting as the bonding partner for the metal phase in the NMIs becomes significant.
   a) *Oxides*
   b) *Sulfides*

   c) *Nitrides*
   d) *Carbides*
   e) *Multiphase:* can consist of two or more phases

(4) **By formation time**: Inclusions can form at various steps, temperatures and different conditions.
   a) *Primary inclusions:* Particles which are formed in the liquid steel by deoxidation or desulfurization reactions
   b) *Secondary inclusions:* Particles which emerge while cooling to liquidus temperature.
   c) *Tertiary inclusions:* Particles which form during solidification between liquid and solid temperature.
   d) *Quaternary inclusions:* Particle which appear in the solid state.

The four criteria to classify the NMIs are summarized in **Table 1**. The possibilities of inclusion categorization reflect the diversity of inclusion appearance.

Table 1. NMIs classification by source, size, type and formation time[3].

Source	Size	Type	Time of formation
Endogenous	*Macro*	*Oxides*	*Primary*
Exogenous	*Meso*	*Sulphides*	*Secondary*
	Micro	*Nitrides*	*Tertiary*
	Sub-micro	*Carbides*	*Quaternary*
		Multiphase	

Initially, these small inclusions collide and agglomerate in liquid steel to form larger particles. Ladle stirring is the most common method to stimulate the agglomeration and flotation of particles and finally to separate the particles into the slag. Nevertheless, a large number of micro-particles stay suspended in the liquid steel and passes on to the next processing stage, the casting process. **Figure 1** gives an overview on possible reactions and interactions of inclusions at different interfaces, where interfacial phenomenas play a crucial role. Over the entire process, interfacial phenomena significantly influence nucleation, agglomeration, flotation, and/or separation of the particles[4–7].

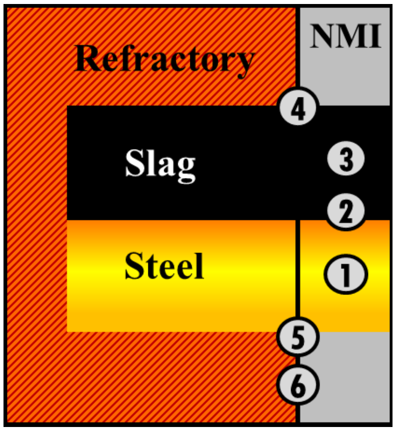

(1) NMI's nucleation, growth and agglomeration in the liquid steel.
(2) Transport of inclusions to steel-slag interface.
(3) Inclusion dissolution in the slag.
(4) Reaction of an inclusion at slag-refractory interface.
(5) Reaction of an inclusion at steel-refractory interface.
(6) Inclusion deposition on the refractory material.

Figure 1. Overview on possible reaction sites in the system steel-slag–refractory. Modified from reference[6].

The casting quality is an issue of central importance for the final product quality. The main quality attributes are the surface quality and the internal quality. NMIs may deteriorate both the surface as well as the internal quality. Micro-inclusions, mostly resulting from deoxidation, are controlled in size and number by ladle refining whereas macro-inclusions may also form during casting. Micro-inclusions adhere under certain conditions in the fluid flow control system and form clogs. The resulting disturbances of the fluid flow as well as detached clogs may worsen the surface quality as well as the cleanness of the cast semis significantly.

One of the main components of the fluid flow control system is the submerged entry nozzle (SEN), which is presented schematically in **Figure 2-a)**. A SEN is a pipe-like refractory component placed between the tundish and the mold in a continuous caster. It prevents the steel from oxygen and nitrogen pick-up and ensures a stable casting operation in the mold[8]. In certain occasions, the inner surface of the pipe is reduced due to material accumulation, formation of complex oxides, or chemical reactions on the nozzle wall[9]. As a consequence, the fluid flow is disrupted causing undesirable flow patters in the mould which cause quality problems in the finished product[9]. These events reduce the net casting throughput and thereby reduce productivity, resulting as well in additional costs. The phenomenon described is known as clogging[8–13].

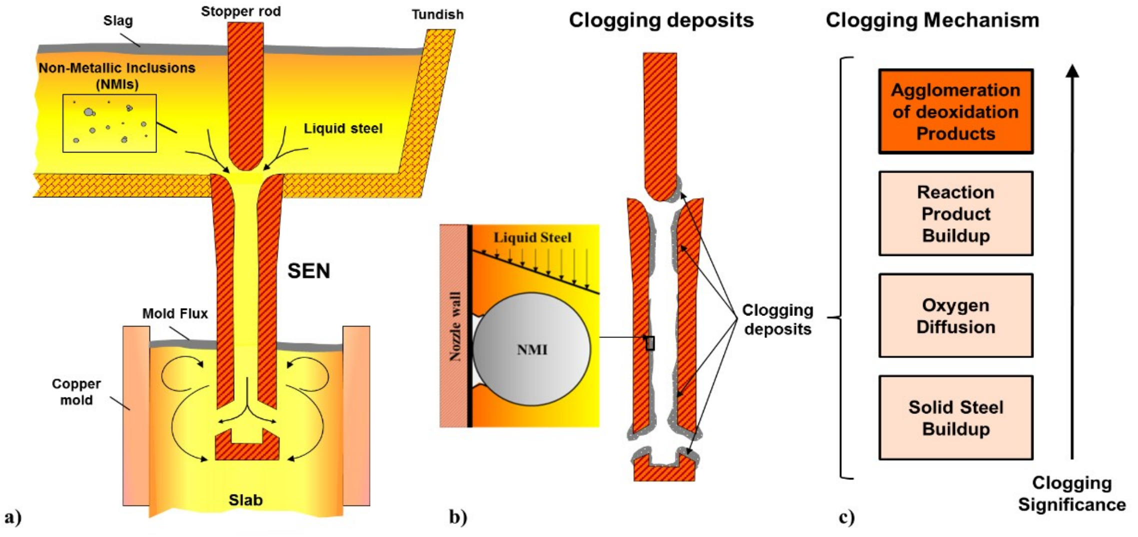

Figure 2. a) Schematic representation of the SEN, **b)** representation of the clogging deposits inside the SEN and **c)** clogging mechanisms.

To compensate for clogging, the flow control device must be regulated during the process. If clogging becomes severe, the flow control device will no longer be able to compensate and then, either a decrease in casting speed or replacement of the nozzle must result. Depending on the casting, some portions of the clogged nozzles (e.g., SEN) can be independently replaced during casting. However other clogged pieces (e.g., stopper rod) can only be replaced by changing tundishes[9].

Clogging results in an uneven reduction of the inner diameter of the nozzle, and consequently the caster operation may be seriously disrupted[9], possibly having –as already mentioned- a considerable impact on the final product quality[14]. The deposits are found along the SEN as well as in areas of the stopper rod, as shown in **Figure 2-b)**.

Numerous studies have been carried out in order to elucidate the clogging mechanisms during continuous casting. Singh et al. and later, Rackers et al. and Thomas et al. summarized them as follows[9,12,15]:

(1) **Deposition of deoxidation products** at the steel/refractory interface due to fluid flow and interfacial tension effects[11–13,16–18].

(2) **Air aspiration** into the nozzle and subsequent reoxidation of the steel at the steel/refractory interface[19–25]. The aspirated oxygen may create a surface tension gradient in the steel near the wall and therefore increase the attractive force towards the wall.

(3) **Chemical reactions** between the nozzle refractory and the steel[19,25–38]. This type of clogging is attributed to reactions between diffused oxygen coming from the refractory and aluminum from the steel.

(4) **Solid steel buildup** during the start of casting when the preheating of the nozzle is inadequate, or within a clog matrix where the flow rate is very slow[22,31,39–42].

Nevertheless, a nozzle deposit is also often the result of more than one of the above-mentioned mechanisms. The present work focuses on the clogging caused by the deposition of deoxidation products at the SEN wall due to its great significance on the initial steps of clogging phenomena as represented in **Figure 2-c)**. The NMIs found in the clogging deposits are from endogenous sources, with a diameter below 20 µm. These oxides form from steel deoxidation and subsequent interaction with ladle slag and ladle lining.

In the following sections, the deposition mechanism of micro-oxides is discussed. Special attention is given to the NMIs separation and adhesion at the steel/refractory interface. Furthermore, possible clogging countermeasures applied during the steelmaking process will be summarized, focusing in the methods related with the modification of the interfacial properties of the system “NMI-steel-refractory”.

1.1 Deposition of NMIs at a steel/refractory interface

Generally, two spherical inclusions approaching each other in the molten steel will tend to agglomerate to form larger particles due to interfacial contact forces as well as to reduce their surface energy. The same behavior is expected for inclusions approaching the nozzle wall[43]. A similar mechanism is also applicable to particle deposition in steel filtration by a ceramic filter[44–46].

In literature, the deposition behavior of NMIs at a steel/refractory interface has been divided into three steps: transport, adhesion and sintering. **Table 2** summarized some of the research done in the deposition of inclusions at interfaces in the steel. Although, there exists common agreement on the deposition of NMIs as an empirical fact, debate considering transport and adhesion mechanism by which inclusions are enabled to adhere at the wall still remains unsettled.

Table 2. Summary of the research done about NMIs deposition at a steel/refractory interface.

References	Deposition steps			Details
	T	A	S	
Singh[12]	X	x	x	General description of the process steps; boundary layer theory
Wilson et al.[11]	X			Local eddy transport phenomena
Dawson et al.[22]	X			Local eddy transport phenomena
Uemura et al.[44]		X	X	Filtration mechanism of NMI in steel at a ceramic filter
Sasai et al.[43,47]		X	X	Al_2O_3 adhesion at a nozzle with steel reoxidation
Kawecka et al.[45]		X		Filtration of NMI in molten steel
Mizoguchi et al. [48,49]		X		Influence of iron oxide in adhesion force
Zheng et al. [50,51]		X		Effect of NMI morphology in adhesion force
Xuan et al.[52]		X	X	Attraction force of Al_2O_3 particle agglomerations in the melt

T = transport, A = adhesion, and S = sintering.

In this work, a more detailed deposition mechanism is illustrated in **Figure** 3. The deposition of NMIs at the steel/refractory interface may consist of five steps and is described as follows:

(1) **Transport**: The NMIs are transported from the bulk region to the boundary layer to the steel/refractory interface upon formation of a thin film of molten steel between the NMI and the refractory wall.

(2) **Separation**: The thin steel film between the NMI and the refractory wall phase will drain to a critical thickness at which rupture occurs. The energy required to force back the metal can result from either the inertial force of the particle or from the decrease in interfacial energy resulting from the adhesion of the inclusion to the wall[53].

(3) **Adhesion**: The inclusions adhere to the refractory wall by interfacial forces, eventually leading to a fluid cavity formation around the contact point. The cavity shape depends on the wettability properties of the materials involved with the molten steel as can be seen in **Detail A** from **Figure 3**.

(4) **Detachment**: The NMIs are subjected to external forces due to the material properties or fluid flow conditions that may detach the inclusions from the steel/refractory interface.

(5) **Sintering**: If the NMIs are not detached, they will sinter forming a solid structure due to the high temperatures involved.

Further inclusions collide and attach to each other, forming a strong network and continuously reduce the inner diameter of the SEN[11,12].

Deposition of NMI at a steel/refractory interface mechanism

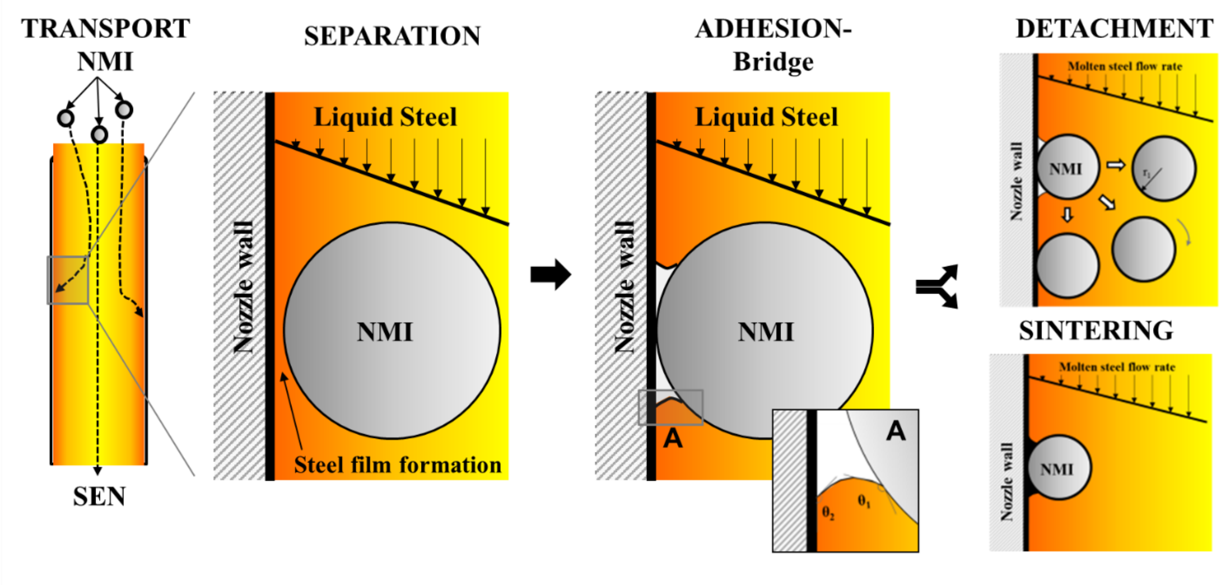

Figure 3. The deposition mechanism of NMIs transported from the bulk flow region into the boundary layer at the steel/refractory interface: Transport, separation, adhesion, and detachment or sintering; **Detail A** represents the cavity contour, which is determined by and the contact angle between the NMI and the steel, θ_1, and the contact angle between the nozzle wall and the steel, θ_2[43–45,47,48,51].

In this section, the deposition mechanism of deoxidation products at the SEN wall has been introduced. In the following, the separation, adhesion and detachment steps are investigated in detail. In these steps, the interfacial properties of the system "NMI-molten steel-refractory" are believed to play a key role. No further analysis of the transport or sintering steps is given.

1.1.1 Separation of NMIs at a steel/refractory interface

When a micro-oxide is brought to the vicinity of a refractory wall, it is necessary for the particle to force back the thin film of metal covering the wall before it can make contact with the surface. The energy required to force back the metal can result from either the inertial force of the particle or from the decrease in interfacial energy resulting from the adhesion of the inclusion to the wall[53]. The free energy change, ΔG, for the separation of a particle in a refractory wall is represented in **Equation (1)**,

$$\Delta G = \sigma \cdot [\cos(\theta_1) + \cos(\theta_2)] \quad (1)$$

where σ is the surface tension of the molten steel, θ_1 is the contact angle of the inclusion with the molten steel and θ_2 is the contact angle between the refractory and the molten steel. More detail on how to obtain **Equation (1)** is given in **Appendix A**.

If $\Delta G < 0$ the separation is thermodinamically feasible and thus the micro-oxides will separate at the steel/refractory interface. Inclusions with large contact angles ($\theta > 90$ deg. in **Figure 4**), which are non-wetted by the molten steel, will have larger negative ΔG values than inclusions with low θ values and therefore they will separate easier from the liquid steel[53–55].

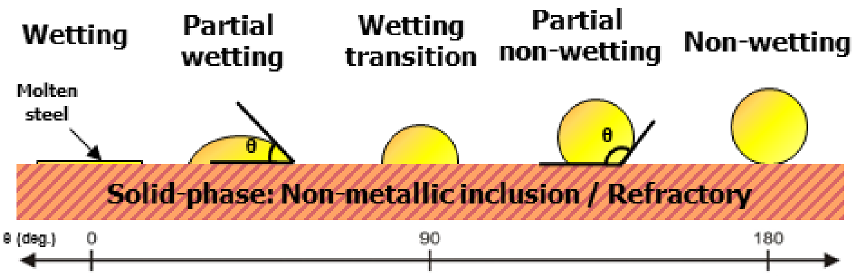

Figure 4. Evolution of the contact angle from 0 deg. (complete wetting) to 180 deg. (non-wetting).

The contact angle of solid oxides and molten steel is found to be non-wetting in most cases. In **Table 3**, the contact angles for different oxides are presented; e.g. 137 deg. between Al_2O_3/pure iron and 110 deg. for ZrO_2/pure iron[11,12,53,54].

Table 3. Contact angles between different solid or liquid oxides and liquid iron.

Material		**Contact angle deg.**	**Material**		**Contact angle, deg.**
Liquid metal/Liquid Substrate			**Liquid metal/Solid Substrate**		
Steel/ Liquid[54]	$CaO{\cdot}Al_2O_3$ 36/64	65	Pure Fe/ Solid[53,54]	Al_2O_3	137±10
				Mullit	130±10
				MgO	125±10
	$CaO{\cdot}Al_2O_3$ 50/50	44[56]-58		CaO	125±10
				MnO	113±10
				SiO_2	113
	$CaO{\cdot}Al_2O_3$ 58/42	54		ZrO_2	110±10
				TiO_2	80

In **Figure 5**, the free energy change, given by **Equation (1)**, is presented for the separation of an alumina NMI at:

(1) A steel/Al_2O_3-based refractory interface in Point (A-A). The Al_2O_3-based refractory has a contact angle with steel of approximately 137 deg.

(2) A steel/ZrO_2-based refractory interface in Point (Z-A). The ZrO_2-based refractory has a contact angle with steel of approximately 110 deg.

Both points indicate that the free energy change is negative, and thus that the separation is thermodynamically feasible. However, the selection of a ZrO_2-based material, in Point (Z-A), reduces the separation tendency of alumina inclusions in comparison with the selection of an Al_2O_3-based material in Point (A-A). The reason for the lower tendency of separation of alumina inclusions at the ZrO_2-based refractory is its better wettability with the steel in comparison with the alumina-based refractory.

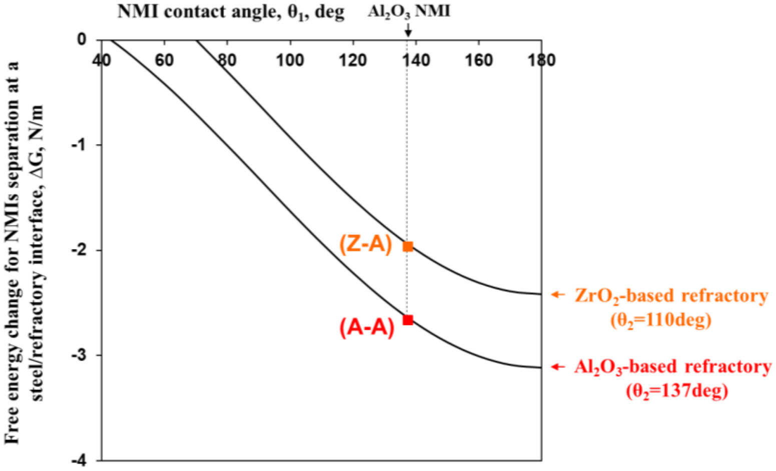

Figure 5. Free energy change when an alumina NMI separation at two different refractories: **(1)** An Al_2O_3-based refractory in **Point (A-A)**, and **(2)** a ZrO_2-based refractory in **Point (Z-A),** given by **Equation (1)**.

Unlike solid oxides, the contact angle between liquid oxides and molten steel is commonly found to be wetting. **Table 3** indicates that liquid calcium aluminates have a contact angle with molten steel between 40-65 deg.[11,12,54]. **Figure 6** presents the free energy change (given by **Equation (1)**) when two different NMIs separate at an Al_2O_3-based refractory. Those NMIs inclusions are listed here:

(1) Solid Al_2O_3

(2) Liquid $CaO \cdot Al_2O_3$.

While the solid alumina NMI shows a negative change of free energy of -3,5 N/m in Point (A-A); the liquid calcium aluminate shows a positive change of free energy of + 0.2 N/m in Point (A-CA). $\Delta G > 0$ indicates that the separation of these inclusions is not favorable thermodynamically. Liquid inclusions may present an advantage for the reduction of clogging problems during continuous casting in comparison with solid inclusions.

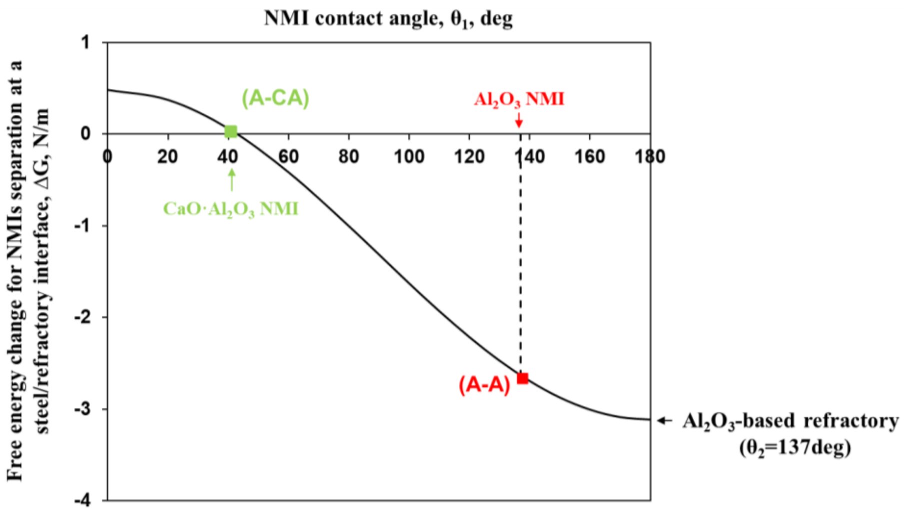

Figure 6. Free energy change, ΔG, when two different NMIs: **(1)** solid Al_2O_3 in Point (A-A), and **(2)** liquid $CaO{\cdot}Al_2O_3$ in Point (A-CA), separate at an Al_2O_3-based SEN refractory given by **Equation (1)**.

The behavior of solid and liquid inclusions regarding the clogging problem is proved to be different due to their different wettability behavior with the molten steel. Solid inclusions normally present contact angles higher than 90 deg. while liquid inclusions present a contact angle between 40-60 deg..

1.1.2 Adhesion of NMIs at a steel/refractory interface

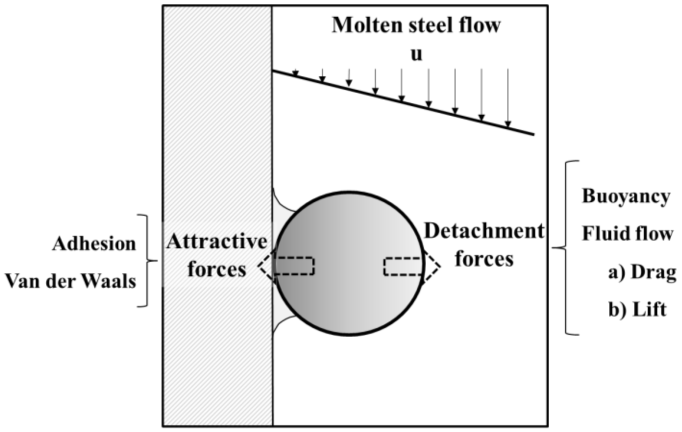

Figure 7. Attractive and detachment forces acting on a NMI adhered at the steel/refractory interface.

The NMIs adhered at a steel/refractory interface may be subjected to attractive forces, which keep the particles at the wall, and to other external forces which force the NMIs to be detached, as shown in Figure

7. Two different attractive forces will be investigated: Adhesion and Van der Waals forces. The detachment forces analyzed are related to the inclusion material properties, such as buoyancy force and to the fluid flow such as drag and lift force.

(1) **Adhesion force:**

If a spherical inclusion approaches a nozzle wall, the steel in the contact area withdraws, leaving a cavity as it is represented in **Figure 3**[43–45,47]. The adhesion of particles in terms of capillary or cavity forces is a direct consequence of the surface contour of the bridge-fluid phase[57,58] and it is attributed to the fact that steel is unlikely to wet solid non-metallic inclusions. The cavity might be filled with:

(1) gaseous components originally dissolved in the melt
(2) gaseous components coming from the refractory
(3) melt vapor, or
(4) liquid phases forming due to a local rise in the oxygen concentration.

Fisher[59] expressed the adhesion force, F_A, in terms of a cavity formation, considering the tension exerted by the steel-fluid interface and the resultant force when the cavity pressure is lower than in the steel. Two methods are established for the calculation of adhesion forces, and they differ in the point at which the forces are applied[57,58,60,61]. For the boundary method, the force is calculated on the contact line between solid, liquid, and gas, whereas the force is calculated at the thinnest point of the cavity for the neck method. Both methods show reasonable accuracy theoretically, experimentally, and numerically[62]. In this work, the adhesion force will be calculated at the thinnest point of the cavity.

If R_2 is the radius at the thinnest point of the neck of fluid connecting the two bodies, the tension exerted by the interface at the neck is $2\pi R_2 \sigma$, and the tensile force due to the pressure difference is $\pi R_2^2 \Delta P$. The force balance calculated at the thinnest point of the neck is written as follows:

$$F_A = 2\pi R_2 \sigma + \pi R_2^2 \Delta P \tag{2}$$

where σ is the surface tension of molten steel and ΔP is the pressure difference between the steel and the cavity phases[43–45,47,48,50,63].

The mechanical equilibrium of the bridge interface is given by the Young-Laplace equation (**Equation (3)**), which relates the pressure difference across the interface to both the mean curvature of the interface and the interfacial tension between the contacting fluids[7,58,60].

$$\Delta P = \sigma \cdot \left(\frac{1}{R_1} - \frac{1}{R_2}\right) \qquad (3)$$

where R_1 and R_2 are the cavity radii. The Young-Laplace equation is required for calculating the adhesion force. However, both the mean curvature and the pressure difference across the steel/cavity interface are not directly known due to the lack of in situ observations. In this case, the difference pressure will be estimated and the cavity geometry is approximated.

The pressure inside the cavity is assumed to be lower than the molten steel pressure and it is chosen[47] the vapor pressure of iron at 1600°C is 6.7 Pa, and the outer pressure will be defined as the atmospheric pressure plus the local ferrostatic pressure. A pressure difference of $1.8 \cdot 10^5$ Pa at 1 m depth[43] is assumed here as a rough estimate for the current work. In **Appendix B**, more details regarding the selection of the pressure value are given.

The mean curvature of the bridge, given by R_1 and R_2 in **Figure 8**, can be calculated based on two different approximations: **(1)** the toroidal approximation that assumes a constant curvature of the contour [57,58] and **(2)** the bridge volume approximation[50,51,64] determined by minimizing the Gibbs free energy of the gas cavity. More details about both approximations and a comparison between them are given in **Appendix C**. Both approaches show good accuracy. In this work, the cavity contour, defined by R_1 and R_2, will be calculated using the **Approach (1),** by solving **Equation (4)**, **(5)** and **(6)**

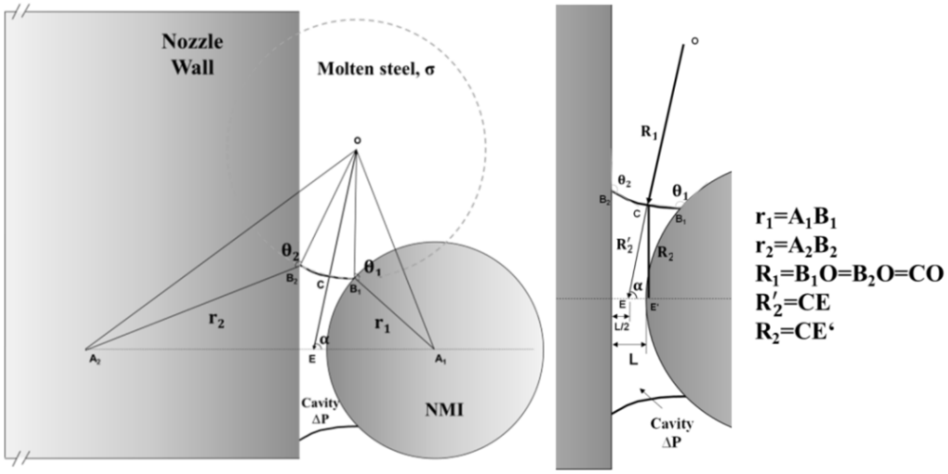

Figure 8. Attraction force between a NMI and a nozzle wall by a bridge formation for particle distance $d \ll r_1$.

$$
\begin{aligned}
&-\Delta P(r_1{+}r_2)\cdot\mathbf{R}_2'^3 \\
&-3\sigma(r_1{+}r_2)\cdot\mathbf{R}_2'^2+\Bigg\{[-2r_1r_2\sigma(\cos\theta_1+\cos\theta_2)]-[2r_1r_2L\Delta P]-[L^2(r_1+r_2)\Delta P] \\
&+\left[\frac{L\sigma(r_1-r_2)(r_2\cos\theta_2-r_1\cos\theta_1)+\Delta PL^2(r_1-r_2)^2}{(r_1+r_2+d)}\right]\Bigg\}\mathbf{R}_2'+L\sigma\Bigg[-2r_1r_2+L(r_1+r_2) \\
&+\frac{L(r_1-r_2)^2}{(r_1+r_2+L)}\Bigg]=0\ \rightarrow\ \mathbf{R}_2'
\end{aligned}
\tag{4}
$$

$$R_2 = R_2'\cdot\sin\alpha \tag{5}$$

$$R_1=\frac{R_2'\sigma}{\sigma+\Delta P\cdot R_2'} \tag{6}$$

where r_1 and r_2 are the inclusion and the refractory radii, respectively; θ_1 and θ_2 are the contact angle between the inclusion and the molten steel and the wall and the molten steel, respectively; α is an auxiliary angle, R_2' is an auxiliary radius and L is the particle distance from the wall.

The bridge force between two particles reaches a more or less constant value when increasing the size of one particle, keeping the second one at a constant size. To explore this configuration in detail, we consider the adhesion force between two spherical particles approaching each other. Assume that the first particle has a 2.5 µm radius (r_1) and is a non-metallic inclusion formed due to steel deoxidation and assume the second particle (r_2) originates from the refractory material. Both particles are aluminum oxides with a corresponding contact angle of 137 deg. with the molten steel. In **Figure 9**, the influence of the size of the second particle on the adhesion force is shown as a function of r_2 at a melt depth of 1 m and 1.8 N/m of molten steel surface tension, and this curve was plotted by solving **Equations (2-6)**. When the size of the refractory particle (r_2) is increased, the force rises until it reaches a constant value when the diameter is greater than approximately 50 µm. In other words, if the refractory particle is much bigger than the non-metallic inclusion ($r_1 << r_2$), the adhesion force between a non-metallic inclusion and a refractory wall can be calculated explicitly. This approach will be used for the rest of the adhesion force calculations in this work.

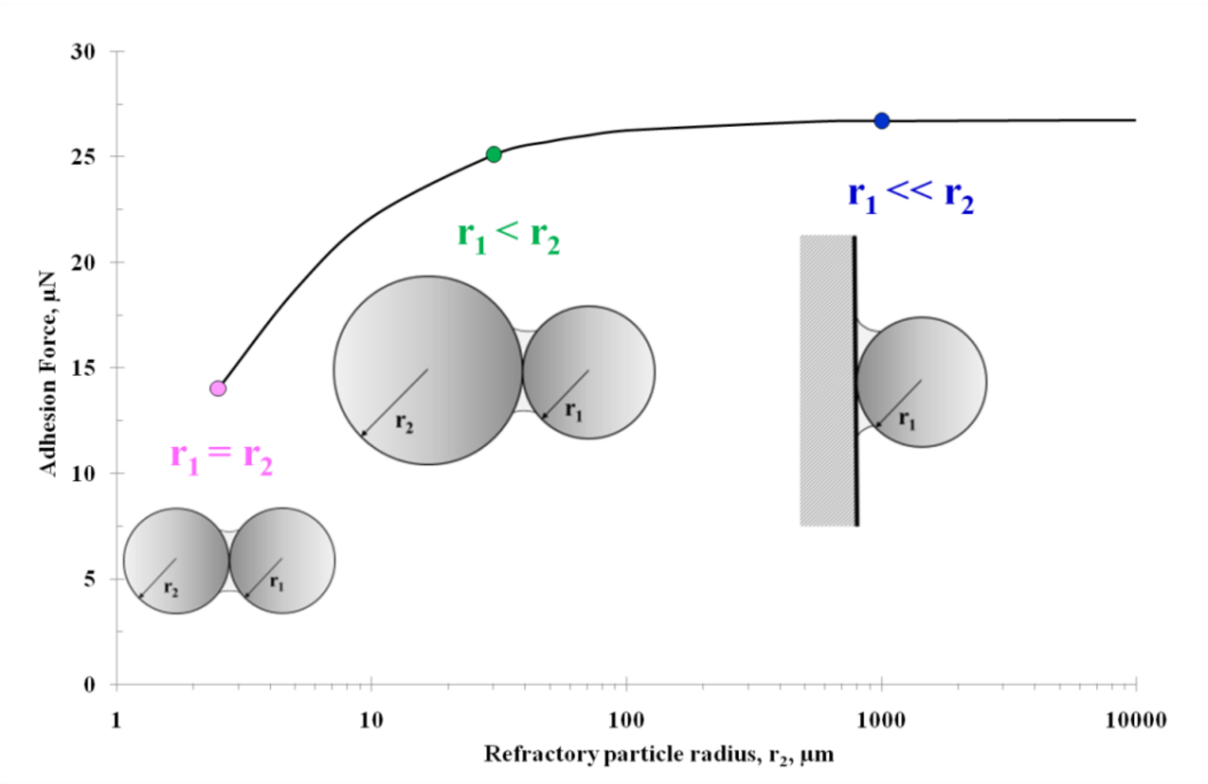

Figure 9. Influence of the size of the second particle, r_2, on the adhesion force.

(2) Van der Waals force

The second attractive force considered is the van der Waals force, which is always present at distances from several nm to the size of the interatomic spacings. When the interparticle distance is smaller than the inclusions size, the van der Waals force acting between two spherical inclusions of different sizes is given by the **Equation (7)**:

$$F_{vdW} = -A_H \frac{1}{6L^2} \cdot \frac{r_1 r_2}{r_1 + r_2} \ \forall \ L \ll r_1 \tag{7}$$

where r_i is the radius of the spherical particle (i=1,2) (m), L is the interparticle distance (m) and A_H is the Hamaker constant (J)[43,65]. Van der Waals forces greatly change with the interparticle distance and the particle size. If the radius of the second particle is much larger than the first particle ($r_1 \ll r_2$)[65], the van der Waals force will be given by **Equation (8)**:

$$F_{vdW} = -A_H \cdot \frac{r_1}{6L^2} \ \forall \ L \ll r_1 \,\& r_1 \ll r_2 \tag{8}$$

As can be seen from **Equations (7)** and **(8),** the van der Waals force is directly proportional to the Hamaker constant. Different values for the Hamaker constant (A_H) are found in bibliography, see **Table 4**. The difference between these four Hamaker constant values is hidden on the selection of the solid iron Hamaker constant, called A_{11}. Sasai et al.[43,47] and Mizoguchi et al. [48] used $21.2 \cdot 10^{-20}$ J which is the solid iron Hamaker constant at room temperature as an approximation. However, Xuan et al. discussed that the Hamaker constant of solid iron cannot represent the one of liquid iron. Lin et at. have used it but they did not consider the parameters of the different oxides inclusions. The Hamaker constant depends on the material properties and the steel temperature, and the value was corrected and used in this work is the one offered by Xuan et al.[52].

Table 4. Hamaker constant for van der Waals calculation.

Reference	**A_H** **J**
Lin et al.[52]	$3.98 \cdot 10^{-19}$
Sasai et al.[43,47]	$0.23 \cdot 10^{-19}$
Mizoguchi et al.[48]	$0.045 \cdot 10^{-19}$
Xuan et al.[52]	$14.3 \cdot 10^{-19}$

Although the exact distance of the bridge formation is unknown due to the difficulties of in situ observation of molten steel, the results of calculations in **Figure 10** barely show any change in the adhesion force at small distances. At intermolecular distances, the van der Waals forces will be significant and will rapidly increase with a decrease in distance between the molecules. Note the regime discrimination between the molecular and the continuum capillary forces at a cut-off distance of roughly 10 nm, in accordance with the mean free path of the molecules. Additionally, it should be mentioned that both forces increase with the inclusion size.

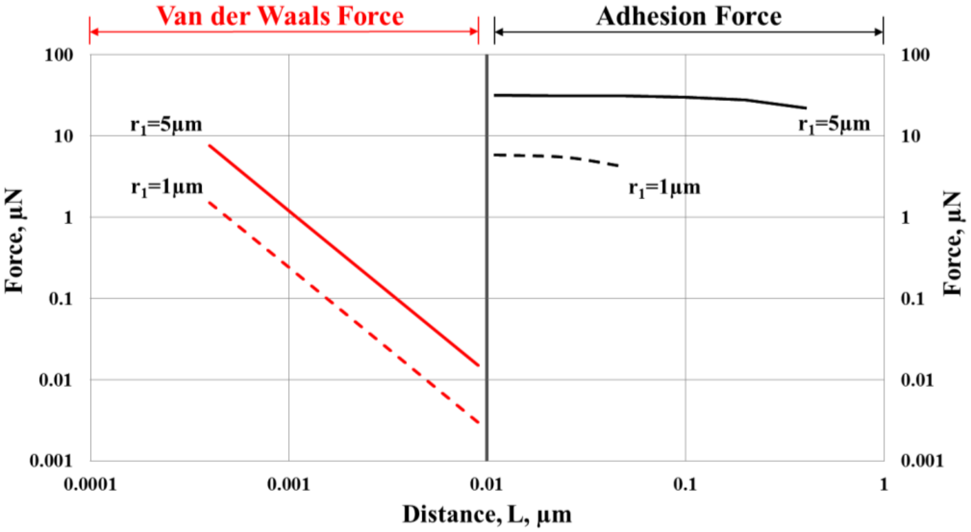

Figure 10. Van der Waals and adhesion as attractive force contribution and their specific range in terms of interparticle distance.

Since the relevant particle wall distances due to the cavity bridges clearly exceed molecular ranges, van der Waals forces will not be considered in the remainder of this analysis.

1.1.3 Detachment of NMIs at a steel/refractory interface

A NMI adhered by a fluid cavity to a refractory may be detached by several force contributions as shown in **Figure 7**. Buoyancy, drag, and lift forces are considered in the following analysis as possible sources for detachment of the inclusion. **Figure 11** represents the forces considered in the system.

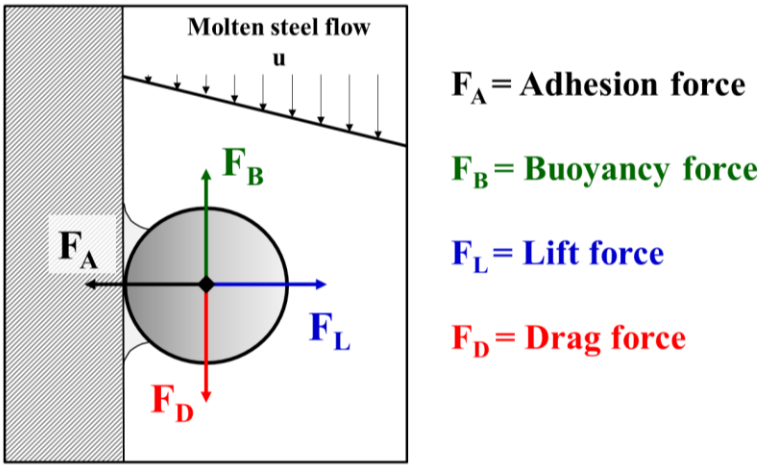

Figure 11. Forces analyzed on a NMI in adhered at a steel/refractory interface in the boundary layer. (F_A = adhesion force, F_B = buoyancy force, F_L= lift force, and F_D = drag force)

To simplify the analysis, it will be assumed that the main motion of a particle in the liquid steel is dominated by translation; rotational or swirling motion of the particle in the near-wall region will, therefore, be neglected.

(1) **Buoyancy force**

Each NMI submerged in molten steel experiences an upward force opposing its weight, known as buoyancy force, F_B. The buoyancy force depends on the density difference between the inclusion and the steel, the gravity acceleration, and the volume of the submerged inclusion, and is given by the following equation:

$$F_B = \frac{\pi}{6} d_1^3 \left(\rho_S - \rho_1\right) g \qquad (9)$$

where d_1 is the inclusion diameter (m), ρ_S and ρ_1 are the density of the molten steel and the inclusion (kg/m^3), respectively, and g is the gravity acceleration (m/s^2).

(2) **Fluid flow forces**

The behavior of adhered NMIs may be influenced as well by the fluid flow in the near-wall region. The flow profile in a circular SEN is characterized by the dimensionless Reynolds number shown in **Equation (10),** and it depends on the ratio of the inertial forces to viscous forces in the fluid.

$$\mathrm{Re} = \frac{\text{Inertial forces}}{\text{Viscous forces}} = \frac{u_{avg}\Phi_{SEN}}{\upsilon} = \begin{cases} \quad\quad\;\; \mathrm{Re} \le 2300 \rightarrow \text{Laminar flow} \\ 2300 < \mathrm{Re} \le 4000 \rightarrow \text{Transitional flow} \\ \quad\quad\;\; \mathrm{Re} > 4000 \rightarrow \text{Turbulent flow} \end{cases} \qquad (10)$$

where u_{avg} is the average flow velocity (m/s), Φ_{SEN} is the SEN diameter (m), and υ is the kinematic viscosity of the steel (m^2/s). The laminar flow can be maintained eventually at much higher Reynolds number (up to 10,000) in very smooth pipes.

In a fully developed laminar flow, the velocity profile remains unchanged in the flow direction. The velocity profile represented in **Figure 12** is parabolic, with a maximum at the centerline and minimum (zero) at the wall. The profile is of the general form:

$$u(x) = 2u_{avg}\left(1 - \frac{x^2}{(2\Phi_{SEN})^2}\right) \quad (11)$$

where x is the radial distance from the centerline of the SEN and u_{avg} is the average velocity in the flow cross section, roughly corresponding to one-half of the maximum velocity.

The turbulent flow along a wall as often encountered in practice is described by four regions that are a function of their distance from the wall: laminar layer, buffer layer, transition layer and turbulent layer. The laminar layer plays a dominant role in flow characteristics due to the large velocity gradient that occurs. The velocity profile for turbulent flow is quite flat compared to the laminar profile (**Figure 12**), with a sharp drop near the nozzle wall.

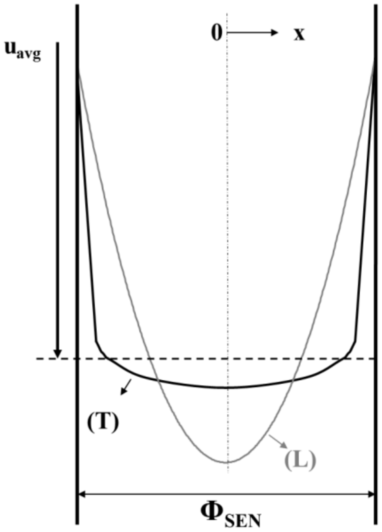

Figure 12. Velocity profile for a laminar flow (L) and a turbulent flow (T) in a nozzle.

The velocity profile in the laminar layer in dimensionless form is known as “the law of the wall for smooth surfaces” and is shown in **Equation (12)**

$$\frac{u}{u^*} = \frac{yu^*}{\upsilon} \ \forall \ 0 \le \frac{yu^*}{\upsilon} \le 5 \quad (12)$$

$$u^* = \sqrt{\frac{\tau_w}{\rho}} \quad (13)$$

$$\tau_w = \mu \cdot \dot{u} = (\rho_S \upsilon) \cdot \dot{u} \ \ \forall \ \dot{u} = \frac{du}{dy} \quad (14)$$

where u* is the friction velocity (m/s), τ_w is the shear stress (kg/ms^2), μ the dynamic viscosity of steel (kg/ms) and υ is the kinematic viscosity of steel (m^2/s), $\dot{u}$ represents the velocity gradient in the laminar layer (s^{-1}) and y is the distance from the wall (m).

From **Equation (15)**, the thickness of the laminar sublayer, δ, is calculated and is proportional to the kinematic viscosity and inversely proportional to the friction velocity, as defined above.

$$\delta = \frac{5\upsilon}{u^*} \tag{15}$$

Force contributions exerted on an adhered particle in the near region of a nozzle wall are analyzed as follows.

Table 5. SEN characteristics.

Φ_{SEN} mm	u_{max} m/s	Re	δ µm	u_δ m/s
30	1	21,000	~370	0.05
	2	42,000	~260	0.07

In **Table 5**, the flow characteristics of a 30 mm in diameter SEN nozzle are presented. The Reynolds number indicates the presence of a turbulent regime inside the pipe for both velocities. The increase of the steel flow velocity in the pipe from 1 to 2 m/s causes a decrease of nearly 100 µm in the thickness of the laminar layer. Thus, the laminar layer gets thinner when the velocity is increased. In addition, the velocity in the laminar layer, u_δ, is in the range of 0.05-0.07 m/s at the limit of the boundary layer and zero next to the wall.

a) Drag force

A spherical inclusion adhered to the nozzle experiences a drag force due to the relative movement of molten steel. The drag force, F_D, depends on the inclusion surface and on the molten steel properties, such as velocity and density according to **Equation (16)**[7,43,47]

$$F_D = C_D \frac{\rho u_r^2}{2} A_1 \tag{16}$$

where C_D is the drag coefficient, A_1 is the projected area of the inclusion toward the flow direction, defined as $\pi d_1^2/4$ (m^2) and u_r is the relative velocity between the inclusion and the molten steel at the inclusion's mass center (m/s). The drag coefficient on a sphere in steady motion can be estimated by using the empirical correlation proposed by Lapple, given in **Equation (17)**[43,47,66]. This equation is an interpolation between the Stokes and the Newton regimes in order to cover the range of cases that will be presented later in this work.

$$\mathrm{C_D} = \frac{24 \cdot \left(1 + 0{,}15 \cdot \mathrm{Re}_\mathrm{p}^{2/3}\right)}{\mathrm{Re}_\mathrm{p}} \quad \forall \quad \mathrm{Re}_\mathrm{p} = \frac{\mathrm{u_r\ d_1}}{\upsilon} \leq 1000 \tag{17}$$

Due to the small particle sizes involved, the particle Reynolds number, Re_p, will be quite small. Thus, the non-stationary drag force terms, such as virtual mass force and Basset force, are not important and therefore will not be considered.

b) Lift force

In addition to the drag force, the flow passing around the adhered inclusion may create a difference in pressure resulting in a lifting force normal to the wall[67,68]. Leighton and Acrivos[69,70] defined an expression for the lift force acting on a sphere resting on a wall, $\mathrm{F_L}$, according to **Equation (18)**,

$$\mathrm{F_L} = 9{,}22\mathrm{Re_G}(\dot{\mathrm{u}}\mu \mathrm{r}_1^2) \ \forall \ \mathrm{Re_G} = \frac{\dot{\mathrm{u}}\mathrm{r}_1^2}{\upsilon} \tag{18}$$

where $\mathrm{Re_G}$ is the shear Reynolds number.

In this section, the deposition mechanism of NMIs coming from steel deoxidation at the nozzle wall was presented. Separation, adhesion and detachment step were the focus. The separation tendency was proved to be higher for solid NMIs than for liquid inclusions due to its different wettability with molten steel. NMIs adhered at the interface by adhesion forces due to the formation of a fluid bridge. Furthermore, the may be detached since they are subjected to other forces such as buoyancy, drag and lift. The mentioned forces were explained here.

1.2 Clogging countermeasures

Over decades a number of clogging-countermeasures were developed to reduce clogging problems in continuous casting. Some of these methods are summarized as follows:

(1) **Change of the nozzle material**: selection of materials with lower wettability with molten steel or use of alternative nozzle materials[13,71,72].

(2) **Modification of deoxidation products** by complete or partial conversion to low melting phases by calcium treatment of the steel[11,13,73–86].

(3) Application of **degassing or vacuum operations** among other treatments for **better cleanness**, meaning to decrease the number of non-metallic inclusions in the steel, in order to decrease the attachment frequency of deoxidation products[11,13,73–86].

(4) **Argon injection** to reduce contacts between inclusions and the nozzle wall, and promote the removal of inclusions by flotation[9,11,13,23,24,87–89].

(5) Development of **new nozzle designs** for a better control of the steel flow and improvement of the insulation and control of the nozzle roughness. Some examples are annular step nozzles[90], electrochemical cell nozzles[91], nozzles with heat insulation[92], bubble curtain nozzles[93], and several others[94,95].

However, even making use of some these precautions, they can not always prevent clogging[96]. Each of these methods has met with partial success, but none has been yet accepted as a single solution by the majority of casters[96]. The reason is that clogging is the result of a complex mechanism which depends on the steel grade produced, process route, and equipment characteristics. And thus, the presented countermeasures may be addapted to each production site.

Table 6. Clogging influential factors and countermeasures.

Influential factor	Improvement mechanism	Property modified	Countermeasure	References
(1) ***Nozzle material***	Decrease in adhesion force between inclusion and nozzle	Refractory wettability	Standard- nozzle material	[13,36,71,72,97–109]
			Selective reactivity	
(2) ***Modification of deoxidation products***		NMIs wettability	Ca-treatment of steel	[11,13,60,73–86]
(3) ***Argon injection***	Elimination of adhesion force	No-contact NMI and Refractory	Argon injection through the nozzle-NMIs collector	[9,11,13,23,24,87–89]

From the previous clogging-countermeasures presented, only the ones related with changes on the interfacial properties of the system "NMIs-Molten Steel-Refractory" will be developed here. In **Table 6**, these countermeasures are summarized. The first two measures refer to the reduction of the adhesion forces by improvement of the wettability of the three-phase system; Whereas, the third measure intends the suppression of the adhesion force by eliminating the direct contact between the NMIs and the refractory wall.

In the following sections, the three most common countermeasures against clogging will be discussed more in detail: Change of the nozzle material, the modification of harmful inclusions and the use of purging gases to float particles in the tundish and to reduce the contacts between particles and the steel/SEN interface.

1.2.1 Change of nozzle material

The selection of refractory materials for the SEN should fulfil the requirements listed below[110,111]:

(1) Minimize the impact to the final product (proper chemistry);
(2) Protect the liquid steel against reoxidation and nitrogen pick-up;
(3) Ensure optimum flow patterns in the mold;
(4) Thermal shock, corrosion, and abrasion resistance;
(5) Do not cause safety and/or environmental concerns;
(6) Design the refractory to meet the desired number of heats or number of casting minutes;
(7) Minimize cost per ton.

One of the most important parameters to select the correct SEN-refractory and eliminate effects such as corrosion, reactivity, and/or clogging, is the wettability. In **Section 1.1** was introduced the importance of the wettability between “NMI & Molten Steel” and “Refractory & Molten Steel” regarding the NMI separation at the steel/refractory interface. If the refractory wettability is improved the separation tendency is reduced as presented in **Figure 5**. Thus, refractories with better wettability with steel will be selected.

However, refractories with good wettability with liquid steel generally exhibit a higher reactivity with steel. Eustatopoulos et al.[10] conclude that it appears to be impossible to find a refractory nozzle material with a low contact angle (below 60-40 deg.) without a high reactivity[10,112]. Thus, a SEN with a contact angle lower than 40 deg. should not be selected.

In many cases, the reactivity is not desired; Nevertheless, there are a few refractories which may present a selective reaction with the alumina inclusions to form low-melting eutectic phases, such as lime-bearing[36,71,97,98,100,101,104], calcium zirconate nozzle materials[97,99,100,105], calcium titanate materials[36,103], O'-SiAlON-ZrO_2 materials[102], BN-enriched materials[72]. These materials are selected for their ability to form low melting compounds as a result of the reaction between the refractory and the solid alumina particles from the steel. The mechanism is described as follows:

(1) The NMIs transported from the bulk region to the boundary layer eventually may come in contact with the nozzle refractory.

(2) At this point, CaO diffuses from the nozzle into each Al_2O_3 inclusion attached. This changes the inclusion composition, causing them to be liquid at steel temperatures[71,104]. This step is illustrated in **Figure 13-a)**.

(3) The alumina accumulates at the nozzle causing gradual liquefying of the surface layer of the nozzle wall forming a liquid/inclusion matrix layer in the wall. If the inclusions build up on the nozzle surface faster than CaO is supplied, the nozzle wall will not be able to liquefy all the inclusions present at the interface and thus clogging can proceed. The force of the flowing steel may wash away large pieces of the liquefied layer, leading to erosion of the nozzle wall[104].

The change in morphology of the NMIs (from solid to liquid) facilitates the detachment of the inclusion from the wall. The advantage of this method is that prevents alumina clogs and increases the nozzle life. However, this methodology causes erosion of the nozzle wall.

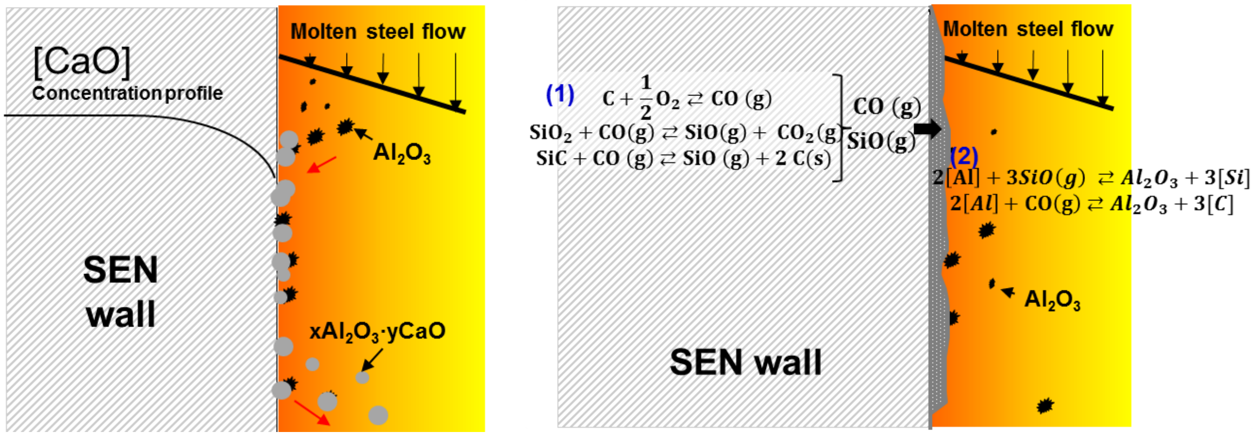

a) **b)**

Figure 13. a) Formation of alumina oxides in low melting-type compounds as a result of the reaction between the solid NMIs and the refractory, and **b)** Refractories containing silicon and carbon clogging mechanism.

Commonly applied SENs were made of alumina, silica and graphite. However, this type of refractory is proved to be prone to clog the SEN. The mechanism behind the clogging of this SENs is described as follows and is illustrated in **Figure 13-b)**[108]:

1. Carbon is expected to react with SiO_2 forming gaseous products like SiO and CO. The reaction gas products diffuse into the molten steel.
2. CO and SiO gas react with aluminum dissolved in the steel forming a solid layer of alumina at the steel/refractory interface.

The more usual development are the carbon free refractories[106–109]. The carbon is removed by oxidation of the inner surface of the SEN and thus, there is not supply SiO (g) and CO (g) to the molten steel avoiding the reaction with the dissolved Al. In addition, their stable surface condition due to the lack of carbon is advantageous in retaining surface flatness and wettability[106].

1.2.2 Modification of deoxidation products

Another possibility to reduce the deposition of NMIs at a steel/refractory interface is to modify the deoxidation products by calcium treatment of the steel[11,13,73–86]. The calcium reacts with aluminum in the steel forming liquid calcium aluminates which are less likely to separate and adhere at the steel/ceramic interface as stated in **Figure 6** of in **Section (1.1.1)**.

Calcium treatment is a widely employed method to modify Al_2O_3 inclusions. Its addition in the molten steel could modify oxide inclusions, performed the desulphurization of steel and control shape of sulphide inclusions. The CaO-Al_2O_3 binary phase diagram[81], shown in **Figure 14-a),** indicates that liquidus temperature is pronouncedly lowered when the two oxides are dissolved in each other. The principle behind the modification of solid alumina inclusions is the reaction of dissolved Ca with Al_2O_3 to produce liquid CaO-Al_2O_3 inclusions avoiding the formation of the solid intermediate phases. However, insufficient or superfluous addition of Ca leads to incomplete or excessive modification of alumina inclusions and the formation of solid calcium aluminates or CaS, which are detrimental to the castability of steels containing more than 200 ppm of sulphur[83].

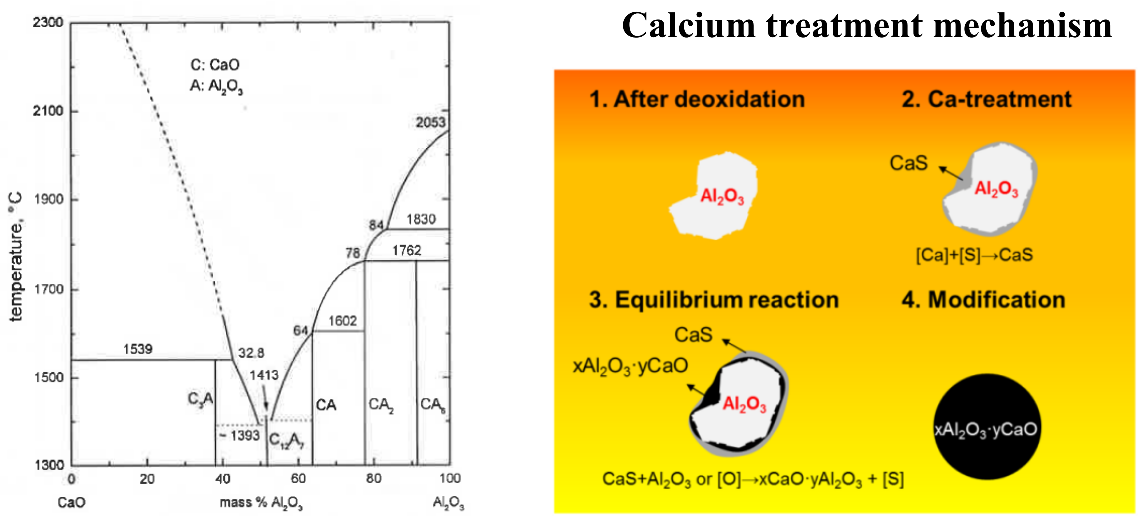

a) **b)**

Figure 14. a) Binary phase diagram CaO-Al_2O_3[81] **b)** Modification mechanism of inclusions during calcium treatment in the molten line-pipe steels. Modified from reference[83].

Ren et al.[83] described the mechanism inclusions during calcium treatment in molten line pipe steel in **Figure 14-b)**:

(1) Irregular Al_2O_3 inclusions generate during deoxidation.
(2) After addition of Ca-Si alloy, the Ca immediately reacts with S. A CaS outer is formed on the Al_2O_3 inclusion.
(3) CaS and Al_2O_3 or O reaction is produced and a layer of $xCaO{\cdot}yAl_2O_3$ is generated between the Al_2O_3 core and the CaS layer. The produced sulphur enters back to the molten steel from the inclusion. Gradually, more and more $xCaO{\cdot}yAl_2O_3$ is generated. The core of the Al_2O_3 inclusion is diminishing and the CaS phase reduce to disappearing. The CaS immediately generated after Ca treatment as a transitional product and disappears as the reaction progress.
(4) Eventually, the Al_2O_3 inclusion modifies to a spherical liquid calcium aluminate.

1.2.3 Argon injection

Argon injection is commonly practiced in the tundish and in the flow control system of the mould, among other locations. It consists in the injection of argon bubbles through holes in the refractory, purging plug or purging beams to mix into the flowing liquid steel[96]. This methodology intends to[9,11,13,23,24,87–89,96,113]:

(1) Promote the removal of inclusions by installation of a purging beam in the bottom of the tundish,

(2) Reduce possible contacts of the inclusions with the nozzle wall by injecting argon at the stopper tip or

(3) Formation of a gas layer at the nozzle wall by injection of argon at the SEN.

These effects are illustrated in **Figure 15**.

Sahai et al.[96] demonstrated by plan trials and water modelling experiments, the beneficial effects of Ar gas injection in a tundish. When argon purging was applied, the number of large inclusions (between 20-100 µm) was reduced significantly. The alumina particles, which are not wetted by the liquid steel, are captured by gas bubbles and floated up to be removed[93,114]. Plant scale experiments[115,116] showed a significant reduction of the number of NMIs in cast slabs. Kumar et al.[115] observed a reduction from 33-70 % in inclusions from 25-50 µm, respectively. In addition, they observed a significant reduction in alumina deposition in the SEN. After an eight-heat sequence, the percentage of area clogged in the SEN was reduced from 35% in a normal tundish to 22% in the tundish with bottom bubbling[115,116].

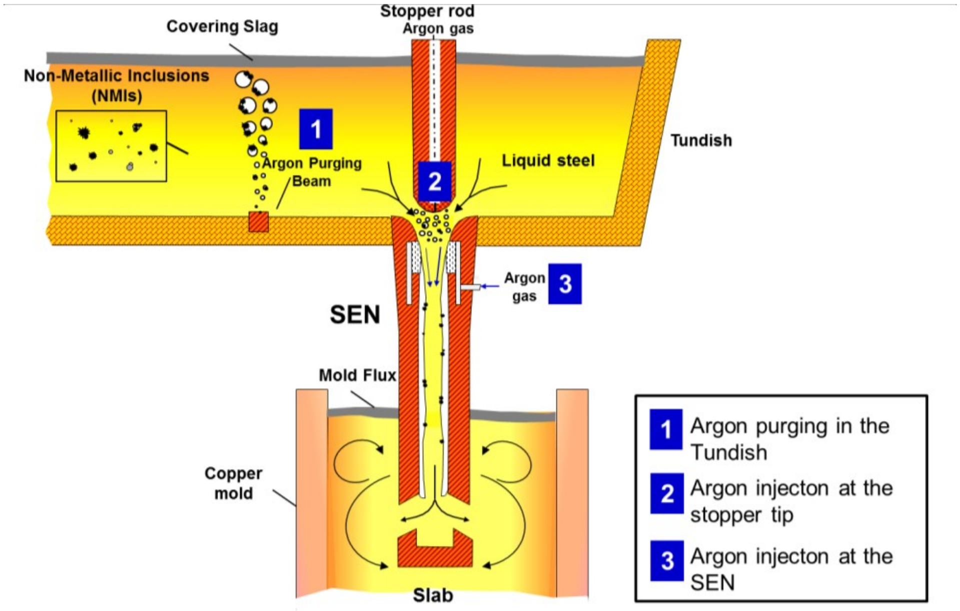

Figure 15. Schematic representation of the tundish, SEN and mould: (1) **A**rgon purging bean in the tundish for the removal of inclusions by flotation, (2) Argon injection at the stopper tip, and (3) Argon injection at the SEN.

In other to reduce clogging the injection of inert gas can be as well performed at the stopper rod tip. The addition of argon at this position increases the pressure below the throttling point and reduces the alumina build up in the casting nozzle[113]. Several methods of Ar injection into the SEN are designed for achieving the defined objective as seen in **Figure 16**[96]. The injection of argon in the SEN is not very common in an industrial scale, being more typically injected at the stopper tip.

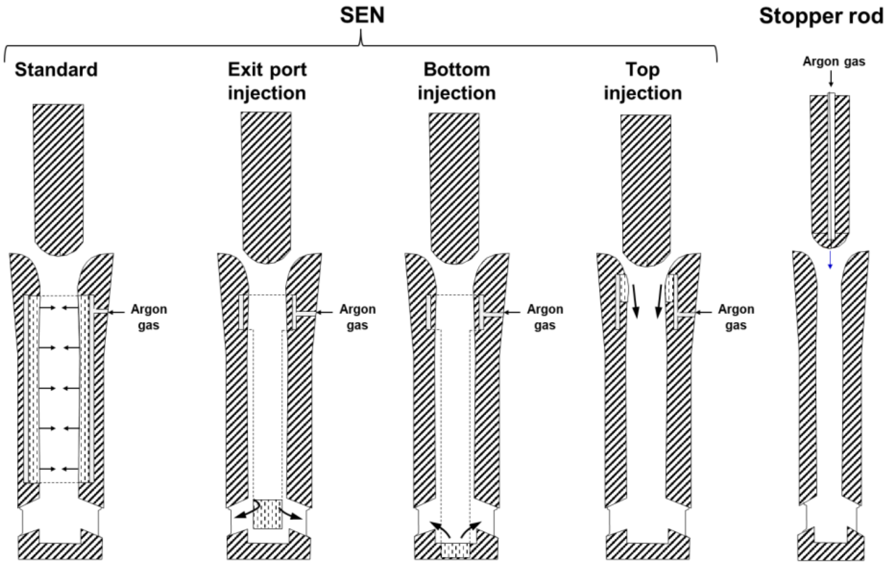

Figure 16. Different configurations of gas injection through SEN[96] and stopper rod.

Table 7 summarizes the advantages of argon as a countermeasure, as well as several side effects or disadvantages. The argon acts as a protection of the refractory to react with the steel and to avoid NMIs interactions, and thus reduce clogging; in addition, increases turbulence and promotes NMIs flotation. The argon injection depends on the steel flow and gas rate flow, needs an optimized SEN design and depends on the bubble size[115,116]. These parameters, among others, need adjustment for a proper application of the argon purging in the flow control system. Otherwise, the argon injection could affect the flow patterns and could disrupt the operation leading to clogging and to defects in the final product surface.

Table 7. Advantages and disadvantages of argon injection[9,88,89].

Ar injection	
Advantages	**Disadvantages**
Prevention of the NMIs to contact the wall	Modification of the flow pattern
Flush off NMIs due to increase of the turbulence	Defects in final product surface; such as “Pencil pipe” and blister defects
Promote NMIs flotation	Operational problems
Reduction of air aspiration through the nozzle	Steel reoxidation
Prevention of chemical reactions between steel and refractory	Entrapment of the mold powder

Different clogging countermeasures during steelmaking have been summarized. Three of them have been further explained:

1. The material selection of the SEN refractory. The wettability of the material has been pointed out to be an important parameter for the material selection.
2. The calcium treatment of the steel. The morphology change of the NMI induces the wettability of the NMIs by the steel, hence reducing the tendency of the inclusions to adhere at the steel/refractory interface.
3. The argon injection is used to reduce clogging by protection of the SEN refractory and thus avoid the adhesion between the NMIs and the refractory wall.

These three countermeasures are based on the reduction or supression of the adhesion forces by modifying the interfacial properties of the system “NMI-Molten Steel-Refractory”.

In the following chapters, these clogging countermeasures are proved to reduce clogging in the SEN region during steelmaking production. The development of a set-up for NMIs obsevation by means of High-Temperature Laser Scanning Confocal Microscopy (HT-LSCM) is presented in **Chapter 2**. A detachment criteria is developed in **Chaper 3** and **4** and is used to defined the critical conditions for a NMIs detachment from a steel/refractory and steel/gas interface. Different cases are proposed and solved in order to study the effect of certain properties such as contact angle, the NMIs size or the role of the gas phase in the clogging phenomena.

2 Clogging evaluation

In this chapter, the clogging evaluation methods are presented and classified into direct and indirect methods. Finally, the High-Temperature Laser Scanning Confocal Microscopy (HT-LSCM) methodology is selected to get a further understanding on how the wettability properties of the system NMI-Molten Steel-Refractory may affect the clogging problem from a qualitative point of view. The experimental set up, limitations, evaluation and test results are detailed here.

Table 8. Clogging evaluation by direct and indirect methods.

Clogging evaluation					
Direct methods		**Ref.**	**Indirect method**		**Ref.**
Investigation of Clogged samples	From plant trials	[13,17,32,72,73,76,81,82,86,87,117–132]	NMIs formation, modification and characterization	2D	[50,51,61,64,83–86,130,131,133–138]
				3D	[50,51,64,83]
	From casting operation at small scale	[8,11,12,18,22,40–42,78,139–143]	*Wettability properties- DSA*	*Steel/Refractory & Steel/NMI*	[128,144]
			NMIs behavior at different interfaces- HT-LSCM	*Liquid steel*	[6,145–162]
				Slag	[6,14,163–171]
				Refractory	[6,147,148]
			Refractory characterization	*Stability with steel*	[28,172]
				Erosion and corrosion	[19,27,29,30,34,97–99,102,109,119,173–175]
				Permeability	[21,103]
				Thermochemical reactions	[38,175]

Over the last decades, much research has been done from side of steelmakers and researchers in order to clarify the clogging sources. Two preferable methodologies are shown in **Table 8**: direct methods that investigate the clogging deposits in a used SEN and, indirect methods, which investigate how isolated parameters such as the interfacial properties of the system "NMI-Molten Steel-Refractory" may affect to the clogging problem. The last ones should be seen as qualitative sources in order to understand the physical phenomena behind the problem.

The direct investigation of the clogged-SEN deposits has been the focus of many researchers:

(1) **Investigation of clogged samples produced during plant trials**[13,17,32,72,73,76,81,82,86,87,117–132]. Clogged SENs from continuous casting are studied in order to identify the root cause of clogging. The informative value of this post mortem analysis is limited as it is mostly impossible to separate the initial causes of clogging from subsequent modifications of the clog by e. g. penetration of the clog by liquid steel.

(2) **Investigation of clogged samples from the simulation of the casting operation at small scale**[8,11,12,18,22,40–42,78,139–143]. Here the steel is melted and poured through a nozzle. The clog interface is usually analyzed to determine the effect of the experimental conditions on clogging. However, these small-scale experiments are difficult to control with respect to the experimental conditions such as temperature, steel composition, number, size and composition of NMIs, pouring time, atmosphere control, among others. In addition, the quantification of these experiments is a challenge since the conditions of the experiment are not stable due to reoxidation or NMIs separation.

The previously described experimental techniques allow a near process simulation of clogging. As already extensively described in **Chapter 1**, clogging is the result of a complex interaction of the formation and conditioning of inclusions in ladle treatment, interfacial phenomena at the steel/refractory interface, the fluid flow in the SEN, temperature losses in the flow control system as well as the access of air (oxygen) into the pouring system. Depending on the case only one of the listed influencing parameters or all of them might be of importance. The consideration of all possible influencing parameters in the laboratory simulation is impossible and the value of the experimental results is therefore limited.

The indirect techniques study isolated effects of related clogging parameters such as nucleation, growth, and modification of NMIs and wettability of the system inclusion/steel or refractory/steel, among others. These techniques have been gaining importance to make significant statements, as well as to verify the simulation model predictions. Some of the clogging related parameters and its experimental techniques are summarized here:

(1) **NMIs formation, modification and characterization:** Investigation of the influence of the treatment of steel by i. e. the addition of alloying elements on NMIs chemical composition, distribution, morphology, number and size. As an example, different deoxidation experiments are carried out where a certain amount of liquid steel is kept at a defined temperature and after addition of the deoxidizing elements, samples are taken at different times. Again, the experimental conditions to produce the desired inclusion population are difficult to control, and thus the experimental conclusions are difficult to establish since the conditions from one experimental set-up to the next set-up might not be the same. Reasons may here be attributed to different crucible materials, differences in the raw material composition or the surrounding atmosphere. Further difficulties are induced due to the change with time of the steel composition, the number, size and composition of inclusions. After the experimental procedure chemical analysis and inclusions characterization are performed. In some cases, only single inclusions are investigated by light microscopy and then serve for the qualitative interpretation of the metallurgical phenomena. Other are based on extensive SEM/EDS analysis[50,51,61,64,83–86,130,131,133–138] were conclusions are drawn on a statistical basis. But even in case of SEM/EDS the individual handling of the raw data makes comparisons difficult and so an inconsistency of results remains. Electrolytic extraction of NMIs[50,51,64,83] is another method, here the size and shape of the NMIs analyzed by SEM/EDS is more accurate, however the number of NMIs analyzed depends on the observer. The analytical methods differ widely.

(2) **Wettability properties:** Investigation of interfacial phenomena between molten steel and solid oxides such as wettability, surface tension and reactivity by means of high-temperature drop shape analyzer (HT-DSA) or Sessile Drop technique[128,144]. This technique is used to characterize the refractory and the NMIs interfacial properties with the steel. The main disadvantage of HT-DSA is related to the long experimental time required and the control of the furnace atmosphere to avoid reoxidation of the steel sample. In addition, the experiments require a further microscopic investigation to assure if the phases are stable or not.

(3) **NMIs behavior at different interfaces:** Investigation of the NMIs' behavior at different interfaces at steelmaking temperature by means of high-temperature laser scanning confocal microscopy (HT-LSCM). It permits the investigation of the NMIs clustering tendency in the liquid steel[6,145–162], the inclusion dissolution in a slag phase[6,14,163–171], as well as the separation behavior of inclusions at a steel/refractory interface[6,147,148]. This methodology shows a high

potential to predict how an interfacial property such as wettability influences the clogging tendency of certain steel grades. The data obtained are used as a qualitative source, since the experimental observation and the clogging phenomena occur at different interfaces. The experimental observation is performed at the steel surface in an argon atmosphere and the clogging phenomena occur at the steel/refractory interface in the bulk.

a) **In the bulk:** The separation of NMIs at a steel/refractory interface in the bulk melt cannot yet be in situ observed. However, the tendency for separation of NMIs at different interfaces can be predicted in terms of interfacial energy.

b) **In the HT-LSCM:** NMIs are observed at the steel surface, whenever they are at certain distance they tend to separate and agglomerate forming clusters. An attractive force is observed and may come from a capillary effect due to the formation of a meniscus around the NMIs. These forces are found in a range of 10^{-19}-10^{-14} N, depending on the NMIs size and interparticle distance. The HT-LSCM observations supplies valuable qualitative data regarding the separation tendency of NMIs at different interfaces

(4) **Refractory stability with steel** by static accretion or crucible experiment[28,172]. Small refractory pieces are cut from SENs. Holes are machined into the refractory pieces and each one is used as a separate crucible to contain a given steel chemistry. Melting and holding steel in small crucibles allows researchers to conduct multiple experiments quickly but shows the same disadvantages as the dip tests. The purpose of this type of experiment is to determine the stability of the refractory material with the alumina inclusions coming from the steel and characterize metal/ceramic interactions.

(5) **Erosion and corrosion by refractory immersion or dip test**[19,27,29,30,34,97–99,102,109,119,173–175]: An induction furnace melts the steel in an argon atmosphere. After killing the steel, samples of the refractory being tested are immersed and usually rotated in the molten steel for various lengths of time. The tests results in accretion formation on the refractory samples. However, the experimental conditions are difficult to control, especially the steel composition and the number and size of inclusions due to its change with the time, the steel flow does not correspond with the one inside the SEN. In addition, the quantification of these experiments becomes delicate since the experimental conditions are not stable and controllable. This method is preferable to provide qualitative information on the erosion and corrosion of nozzle refractory materials.

(6) **Others:** Determination of the properties of the refractory; such as permeability[21,103], and thermo-chemical reactivity[38,175].

Summing up, one cannot stablish any direct conclusions from the indirect methods since they only investigate isolated related clogging parameters. But these investigations are needed as a imput for computational simulation of metallurgical processes[15,94,126,176–185]. In the following sections, the HT-LSCM is presented as a tool to investigate how the wettability of the system "NMI-Molten Steel-Refractory" may influence the clogging tendency of certain steel grades.

2.1 High-temperature laser scanning confocal microscopy (HT-LSCM)

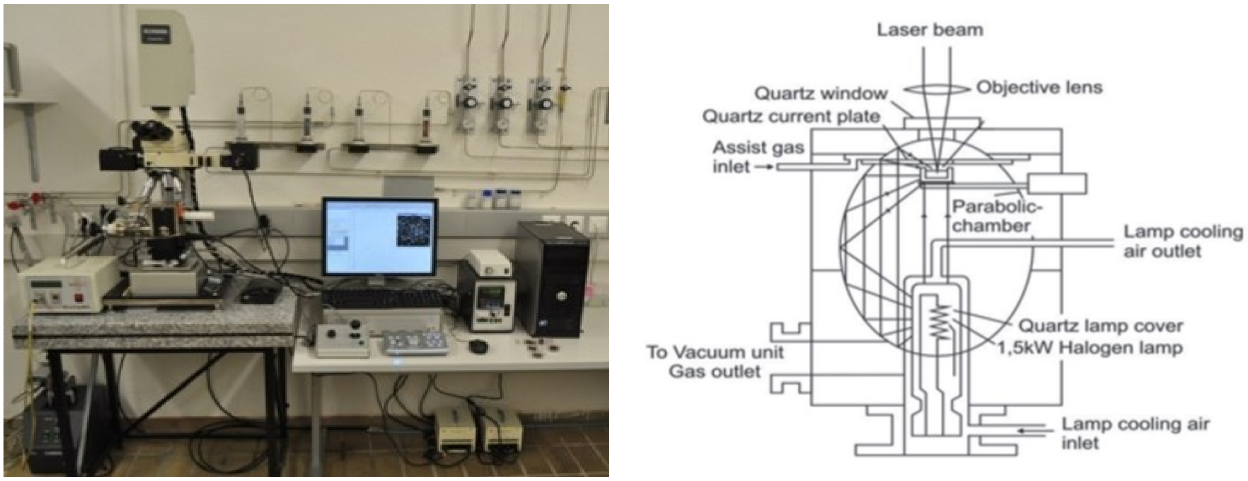

a) **b)**

Figure 17. (a) HT-LSCM in the laboratory[186] and **(b)** transverse section through the infrared heating furnace [187]

The high-temperature laser scanning confocal microscope (HT-LSCM) in **Figure 17-a)** implies the possibility of in-situ steel observations at temperatures up to 1700 °C with a very good image quality; due to the fact, that a violet laser with a wavelength of 405 µm is used as a light source. A Confocal Scanning Laser Microscope (VL2000DX from Lasertec) and a high temperature furnace (SVF17-SP from Yonekura) are used in this investigation. A schematic view of the high temperature furnace which shows an elliptic, gold coated inner contour is shown in **Figure 17-b)**. The halogen lamp is situated in the bottom focal point of the furnace and the sample holder with the crucible and sample inside is located in the top focal point of the ellipse. The temperature is measured with a thermocouple fixed at the bottom side of the sample holder. High-purity argon with a flow rate of 125 cm^3/min ensures a neutral atmosphere in the furnace. Additionally, the oxygen content in the furnace is measured for every experiment. The detailed configuration data can be found elsewhere[147,186].

The HT-LSCM is a strong tool which enables in situ observation of different high temperature metallurgical phenomena; by combining the advances of a laser, confocal optics and an infrared image furnace. Some of the metallurgical phenomena investigated by HT-LSCM are summarized in **Table 9**. Phase transformation of certain steel grades, steel cleanness by the study of the inclusions' dissolution in slags and the NMIs behavior in molten steel have occupated much of the HT-LSCM research investigation over the past 20 years. The current work deals with the in situ observation of NMIs at different interfaces.

Table 9. Different metallurgical phenomena observed by means of HT-LSCM.

Metallurgical phenomena			**References**
Phase transformations in steel	Peritectic phase transition		[188–199]
	Nucleation of acicular ferrite		[200–211]
	Austenite grain growth		[187,212–220]
	Other Phase Transformations		[221–239]
Steel cleanness	Inclusions dissolution in a slag phase		[6,14,163–171,240]
	In situ alloying and deoxidation		[241,242]
Non-metallic inclusions behavior	Agglomeration	at liquid steel surface	[6,145–162,243]
		at steel/refractory interface	[6,147,148]

Table 10 summarizes the state-of-the-art in research regarding the NMIs behavior at steel/Ar interface by HT-LSCM. A strong long-range attraction, over 10^{-16} N and extending as far as 50 µm, between alumina particles is firstly observed on the molten steel surface. Both the magnitude and the acting length of the attraction increase with the increase of particle size. The long-range attraction is found to be almost independent on the composition of steel melt, but greatly influenced by the physical properties (contact angle and density) and morphology (solid or liquid) of the NMIs[146]. The strength of the capillary attraction force for NMIs pairs in molten steel regarding its morphology, was listed by Yin et al. [145] as follows in ascending order: liquid/liquid pair < liquid/semi-liquid pair < semi-liquid/semi-liquid pair < liquid/solid pair < semi-liquid/solid pair, and finally solid/solid pair as the strongest.

Furthermore, the HT-LSCM confers the possibility of the observation of NMIs at steel/refractory interfaces. **Table 11** gives an overview on the research done on this topic. Aneziris et al.[148] investigate the collision between inclusions when an endogenous inclusion is placed on the top of the steel sample to study the filtration efficiency of different steel filters. In the following section, the observation of the behavior of NMIs at a steel/ceramic interface will be investigated in relation with the clogging problem.

Table 10. HT-LSCM-Investigation of inclusions behavior at steel surfaces in the last 20 years.

Year	Literature	Inclusions			Steel	Atmosphere
		Solid	**Complex**	**Liquid**		
1997	[149,244,245]	Al_2O_3			Low Carbon steel	Ar
		A80S			Fe-3%Si	
		CA		CA60S	HSLA steel	
		CA80S CAS95		CA50S	Si-killed steel	
		CA80	CA60	CA50	HC-Ca steel	
2001	[150]	MgO	$Al_2O_3 \cdot MgO$		Mg-added Al killed steel	Ar
2001	[152]	Al_2O_3 $Al_2O_3 \cdot CaO$	$Al_2O_3 \cdot CaO \cdot MgO$		Stainless steel	Ar
2001	[153]	$Al_2O_3 \cdot CaO$	$MgO \cdot Al_2O_3$	$Al_2O_3 \cdot CaO \cdot MgO(\cdot SiO_2)$	16Cr Al-Si killed steel 16Cr Si killed steels	Ar
2003	[154]			$Al_2O_3 \cdot CaO$	Ca-Treated, Al-killed steel	Ar
2004	[155]	Al_2O_3 $Al_2O_3 \cdot MnO$		$Al_2O_3 \cdot MnO-SiO_2$	Mn-Si killed steel	Ar
2008	[243]	Al_2O_3 Ce-O	Al-Ce-O		Misch-metal	Ar
2007 - 2010	[161,162,246]	Al_2O_3			Tool steel	Ar
		$MgO \cdot Al_2O_3$				Ar+1vol%H_2
		$CaO \cdot 2Al_2O_3$				Ar+2vol%H_2
				$CaO \cdot Al_2O_3$		Ar+3vol%H_2
2008	[56]			$Al_2O_3 \cdot CaO$	steel	Ar
2015	[156]		$CaO-MgO-Al_2O_3-SiO_2$		Low oxygen special steel	Ar
2015	[6,147]	Al_2O_3		$CaO \cdot Al_2O_3$	ULC steel Ca treated steel	Ar
2017	[157]	Al_2O_3, $MgO \cdot Al_2O_3$			H13 Steel + Mg Addition	Ar
2017	[160]	TiN, Ti_2O_3			Low Carbon steel	Ar
2017	[158,159]	Al_2O_3			Low Carbon steel	Ar

A = Al_2O_3, C = CaO, S = SiO_2

Table 11. Investigation of different NMI behavior at molten steel/ceramic interface.

Year	Literature	Inclusions		Steel	Refractory/Filter/ Ceramic
		Solid	Liquid		
2013	[148]	Al_2O_3	$TiO_2 \cdot Al_2O_3$	Stainless steel	Al_2O_3
2015	[147]	Al_2O_3 Al_2O_3 with Mn, Ca, S traces	$Al_2O_3 \cdot CaO$	ULC steel Ca treated steel	Al_2O_3

2.1.1 Observation of NMIs at steel/ceramic interface

The observation of the behavior of NMIs in the steel and at a steel/ceramic interface will be investigated in relation with the clogging problem. A two-step set-up has been developed and the HT-LSCM experimental limitations are commented. The experimental work has the following objectives:

(1) First, the investigation of the behavior between NMIs at the steel surface. The behavior of inclusions from a Ca-treated steel will be compared with the behavior of solid alumina inclusions coming from an ULC steel. In addition, this step is needed to characterize the observed NMIs, thus the sample is investigated under SEM-EDS.

(2) Investigation of the behavior of NMIs with different morphologies towards a steel/ceramic interface and their behavior with the change of the ceramic. The same Ca-treated steel used in the previous step is used here and the ceramic used are Al_2O_3, MgO and ZrO_2.

As result, the attractive forces between NMIs at steel and different steel/ceramic interfaces will be calculated from observations and will be compared with a theoretical capillary attractive force. For the solution of the theoretical model, contact angles between NMIs and steel and ceramic and steel are needed, and thus HT-DSA experiments were carried out, to implement the results in the model.

2.1.1.1 Experimental set up

A two-step experimental set up is performed:

(1) **Characterization of NMIs observed at the molten steel surface.** A steel disc (600 µm thickness and 7 mm diameter) is placed in an Al_2O_3 crucible and subsequently set up on the sample holder in the ellipsoidal furnace (see **Figure 18**). An alumina disc is placed under the steel disc in order to avoid the attachment of the steel disc onto the crucible. The crucible was introduced into the

furnace and the chamber was purged with high purity argon to ensure an inert atmosphere. When the liquidus temperature of the steel is reached, inclusions are starting to emerge from the bulk to the steel surface and their agglomeration behavior can be studied. The objective of the present study is to characterize the NMIs behavior at the molten steel, including the NMIs type and size.

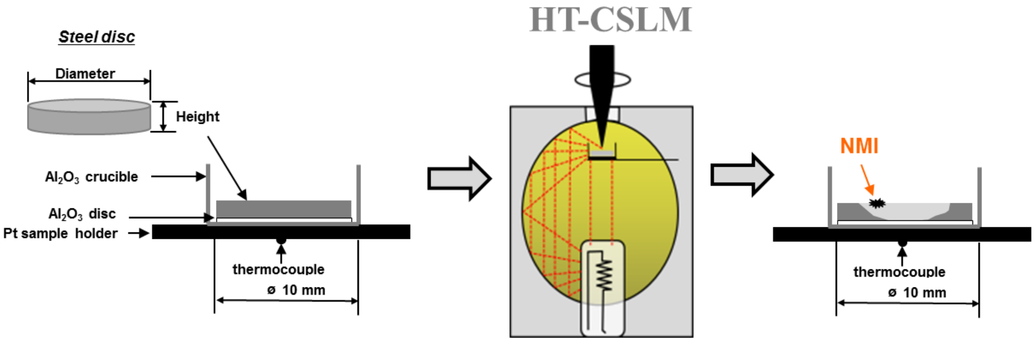

Figure 18. Experimental set up 1: Characterization of NMIs observed at the molten steel surface.

(2) **NMIs inclusions behavior at different molten steel/ceramic interfaces:** Each experiment was conducted by placing a single ceramic-particle (Equivalent circle diameter (ECD) = 400 μm), on the surface of a steel disc (600 μm thickness and 7 mm diameter); all inside an alumina crucible, as shown in **Figure 19**. An Al_2O_3 disc was place between the steel and the crucible to avoid the sticking of the sample. The crucible was introduced into the furnace and the chamber was purged with high purity argon to ensure an inert atmosphere. When the specimen reaches liquidus temperature, inclusions start to emerge from the bulk to the steel surface and a meniscus forms around the exogenous ceramic-particle. The current experiments investigate the influence of the “NMI-steel-Refractory” wettability into the separation tendency of NMIs at different interfaces. For that purpose, the attractive forces in reference to a steel/ceramic interface are investigated and estimated.

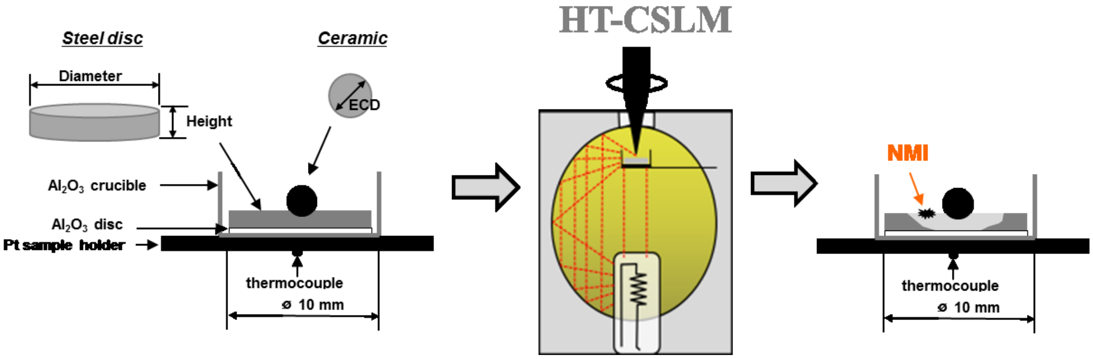

Figure 19. Experimental set up 2: NMIs inclusions behavior at different molten steel/ceramic interfaces.

2.1.1.2 Experimental limitations

There are certain limitations that restrict the experimental set up and the observations. They are summarized in **Table 12**,.

Table 12. HT-LSCM limitations for the observation of NMIs at steel and steel/ceramic interfaces.

Limitation	**Cause**	
Melting of the sample	Inner furnace conditions	
	Sample dimensions	
	Steel grade	
	Contact between the pool and the bottom of the furnace	
Furnace atmosphere	Re-oxidation	
	NMIs-modification	
	Evaporation	
Experiments evaluation	NMIs	Complex (Semi-liquid)
		Size limit
		Irregular shape
		Composition
Ceramic-particle	Change of position during the experiment	

(1) **Controlled melting of the steel sample:** The crucible with the sample is placed on the upper focal point of the furnace that received the heat from the lamp, which is placed on the lower focal point. During heating, the sample suffers a temperature gradient, leading to the partial melting of the sample from the center. There are different inconveniences that lead to an uncontrollable melting of the sample:

a) **Inner furnace conditions:** The design of the glass-cover of the lamp modifies the trajectory of the heat rays making the temperature gradient non-uniform in the sample. The furnace cleanliness and the coating conditions may influence the gradient rising the melting temperature. In these situations, it is observed that the melting starts from the edge of the sample.

b) **Sample dimensions:** The shape of the sample from cylindrical to prismatic seems not to affect the melting conditions but the sample thickness does affect it. Too thin samples, below 400 µm, show a starting stable melting area; however, it rapidly breaks leading to the observation of the crucible's bottom. Too thick samples, above 1 mm, form quickly a steel droplet. The optimal thickness of the sample for a stable melting was found to be around 500-800 µm.

  c) **Steel grade:** It was observed that the higher the alloy elements the harder to control the melting. For example, ULC steel was easier to control than a Ca-treated steel. More information regarding the steel composition is given in **Table 13**.

  d) **Contact between liquid steel and the bottom of the crucible:** This may cause some steel/crucible interference such as, steel reoxidation.

(2) **Furnace atmosphere:** The system is put under vacuum to clean the atmosphere of the furnace before the experiments. Right after argon starts to flow. The argon 6.0 (containing < 2 ppm O) goes through two filters for O_2 and H_2O vapor. In order to further reduce the oxygen content in the flow, the argon goes through a tube furnace which contains Ti-turnings at around 700 °C. The oxygen concentration in the furnace to start the experiment should be below 1 ppm. The oxygen concentration in the argon flow is measured by the Cambridge Sensotec Rapidox 2100 Oxygen Sensor Analyzer.

  a) **Reoxidation:** If the furnace is not correctly purged before the experiment, or the argon brings some oxygen or there is a leakage in the pipe system, the sample may be reoxidized during the experiment. A formation of a layer on the top of the sample or the formation of too many inclusions during melting of the sample covering a wide range of the pool could be observed.

  b) **NMIs modification:** Due to possible oxygen sources, the NMIs have the tendency to react with the oxygen.

  c) **Evaporation:** Elements like manganese show a certain tendency towards evaporation during high temperature experiments. For relatively low Mn-concentrations of < 1 wt.-% the influence on the experiments is marginal whereas for higher Mn-concentrations the loss of Mn will have to be considered.

(3) **NMIs evaluation**:

  a) **Complex inclusions (semi-liquid):** it is not possible to recognize them directly. They may be mixed up with liquid inclusions if their shape is fully globular or with solid inclusions if their shape is irregular.

  b) **NMIs size limit:** No inclusions below 3 µm are accurately observed.

c) **Irregular inclusions size:** The size of irregular inclusion is approximated to its equivalent circle diameter (ECD).

d) **NMIs composition:** The sample needs to be investigated after the experiment to characterize the inclusions observed.

(4) **Ceramic-particle position:** the ceramic-particle introduced can be moved due to fluid flow or spin inducing other forces in the observations.

The limitations summarized here, determine the set-up chosen in the previous section but as well the experimental evaluation and results, which are presented in the following sections of this work.

2.1.1.3 Experimental evaluation

Each HT-LSCM experiment is recorded, and the video evaluation is performed by analyzing it frame by frame. In each image the temperature and the time are plotted. During the analysis, the position of a 'guest particle' (NMI) towards a static 'host particle' (NMI or ceramic-particle) is analyzed, as represented in **Figure 20-a).** In **Figure 20-b),** the trajectory of a guest particle, called 'D', towards the 'host particle', called 'A' is traced during an experiment.

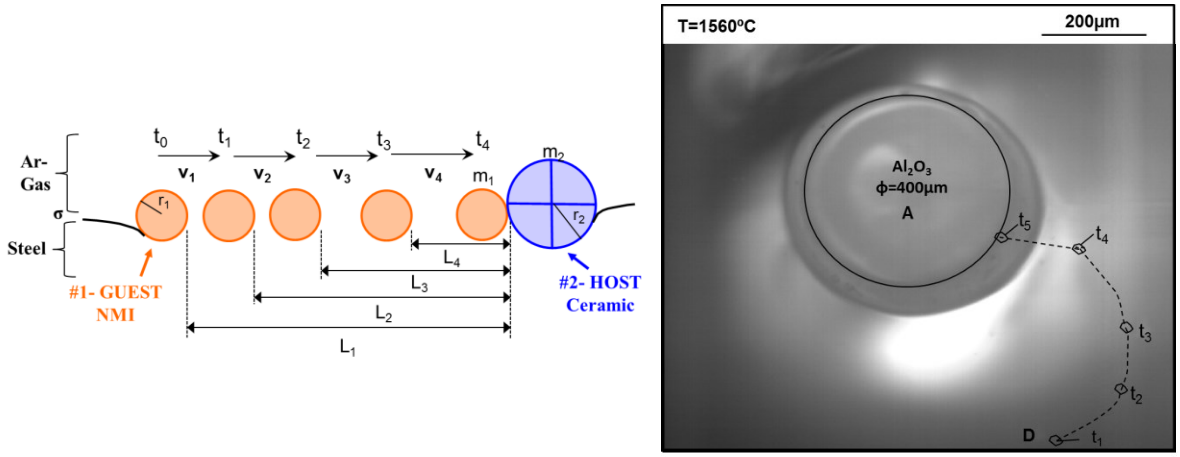

a) **b)**

Figure 20. a) Schematic diagram of the HT-LSCM experiments evaluation, and **b)** Trajectory of particle D towards 'A' surface during an experiment.

When the particle D is at certain distance from particle A, 'D' experiences a long-range attractive force and separates at 'A'. The attraction force, $F_{HT\text{-}LSCM}$, was given by Yin et al.[146,244] and it is calculated as follows:

$$F_{HT-LSCM} = m_1 \cdot a_1 \qquad (19)$$

where m_1 is the mass of the 'guest particle' and a_1 is the acceleration of the 'guest particle'. If two particles moved simultaneously, a revision was made by a factor of $m_2/(m_1 + m_2)$ in **Equation (19)** with m_2 the mass of the 'host particle'. In this analysis, the friction force which arises from viscous drag of the particle by liquid steel surface was ignored[244]. Yin et al. [146,244] describe an approximate evaluation of the magnitude of the attraction force from measured acceleration and estimated mass of particles:

(1) **Measured acceleration, a_1:** The movement of particle D, in **Figure 21-a),** is traqued every 0.2 seconds and its distance from the center of the ceramic-particle A is measured in each position. Particle A is considered to be always in the same position. Thus, the acceleration, a_1, of the 'guest particle' when the 'host particle' in the pair stayed quiescent can be determined from the change of the position of the guest particle at 0.2 seconds intervals as shown in **Figure 21-b)**[244].

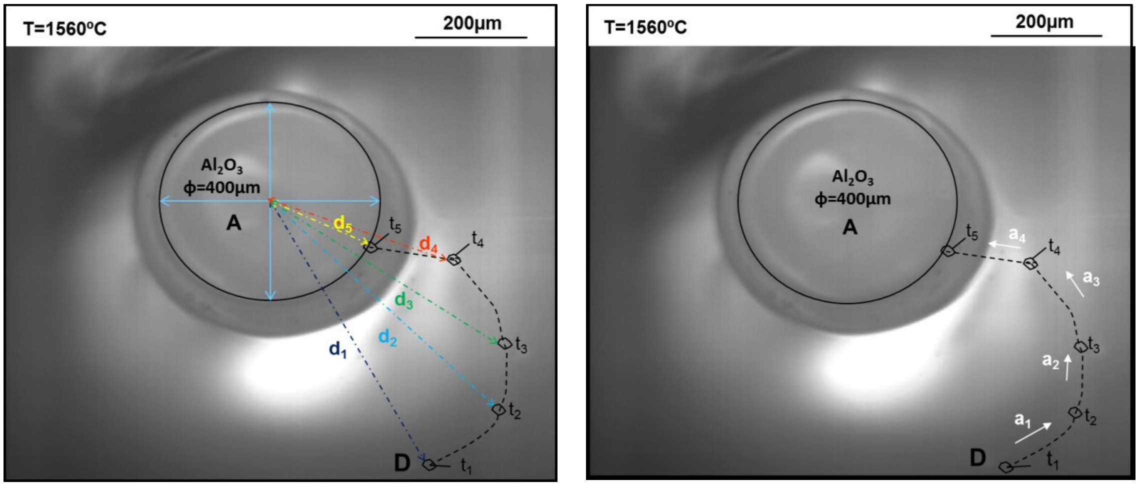

a) **b)**

Figure 21. Detailed sequence of agglomeration caused by the long-range strong attraction between two alumina particles on a moving surface of Ca-treated liquid steel at 1560ºC.

(2) **Estimated mass of the particle, m_1:** The particle shape was approximated to be spherical (ECD). If the particle was irregular the length of long axis (d_1) and short axis (d_2) of a particle were observed. Further, the ellipse was approximated to be a sphere of radius, r_1, which was taken to be the geometric average in **Equation (20).**

$$r_1 = \frac{\sqrt{d_1 \cdot d_2}}{2} \tag{20}$$

Therefore, the mass of the particle, m_1, can be approximated by **Equation (21)**[56,148,154,155].

$$m_1 = \rho_1 \cdot \frac{4\pi}{3} r_1^3 \tag{21}$$

With ρ_1 the density of the 'guest particle'.

2.1.1.4 Theoretical evaluation

It is observed that some inclusions in the steel bath approaching a ceramic-particle surface experience a long-range attractive force, which makes them separate and agglomerate at the surface. However, it is necessary to confirm whether the observed attraction in the HT-LSCM is caused due to capillary effects or due to other forces such as fluid flow in the surface of the melt. For that purpose, the theoretical capillary force between two particles at a steel/argon interface is investigated here.

When two particles float at a molten steel/argon interface, the meniscus of the interface around the particle is deformed by a capillary effect creating an interaction between the two particles when they are a certain distance of each other[247]. Floater-to-floater interaction, represented in **Figure 22**, was first modeled by Nicolson & Chan et al.[248] for spherical bubbles. They assumed that the attractive force on a bubble is only due to the surface profile created by the other bubble, neglecting the interaction of the moving bubble with its own meniscus. Later Kralchevsky & Paunov et al.[249,250] studied the capillary forces between spherical particles floating attached to a liquid-fluid interface, when the meniscus deformations are due to particle weight.

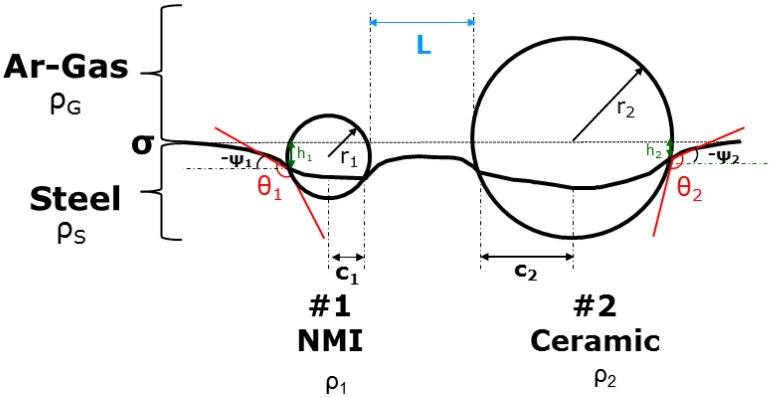

Figure 22. Schematic diagram of capillary meniscus around two spherical particles.

The capillary meniscus around two spherical particle of radii r_1 and r_2 floating at an interface between molten steel and argon of mass densities ρ_S and ρ_G, respectively. Each of these particles protrudes from the steel, and three-phase contact lines of radii, c_1 and c_2, are formed. Where the steel meets the particle surface, the respective contact angles, θ_1 and θ_2 are formed, and the surface tension of this phase boundary will be denoted by σ. Far from the particles, the interface is flat and horizontal[251].

Kralchevsky et al.[251,252] represented the free energy of the system, W, as a superposition of gravitational, wetting, and liquid meniscus contributions:

$$W = W_g + W_w + W_m \tag{22}$$

W_g represents the gravitational energy of the particles and steel and gas phase, W_w is the surface free energy of the particles and W_m denotes the free surface energy of the liquid meniscus. The reference zero state to be the free energy of the same particles, taken at the infinite interparticle separation. Then the interaction energy, ΔW, between particles 1 and 2 can be defined by

$$\Delta W = W - W_\infty = \Delta W_g + \Delta W_w + \Delta W_m \tag{23}$$

Where W_∞ is the free energy when the two particles are far apart.

The capillary interation force, defined as ΔW, defined as $F_{cap}=-\frac{d(\Delta W)}{dL}$, will be calculated as follows:

$$\frac{d\Delta W_w}{dL} = -\pi\,\sigma\sum_{k=1}^{2}(qc_k)^2 r_k\cos\theta_k\frac{dh_k}{dL}\,x\left[1+O\left(q^2c_k^2\right)\right] \tag{24}$$

$$\frac{d\Delta W_m}{dL} = \pi\,\sigma\sum_{k=1}^{2}\left[Q_k+(qc_k)^2 r_k\cos\theta_k\right]\frac{dh_k}{dL}\,x\left[1+O\left(q^2c_k^2\right)\right] \tag{25}$$

$$\frac{d\Delta W_g}{dL} = -\pi\sigma\sum_{k=1}^{2}2Q_k\frac{dh_k}{dL}\,x\left[1+O\left(q^2c_k^2\right)\right] \tag{26}$$

where h_k is the elevation of the contact line for particle 1 and 2, Q_k is the capillary charge for particle 1 and 2, L is the interparticle distance, and $q^{-1} = \left[\frac{\sigma}{(\rho_S-\rho_G)g}\right]^{\frac{1}{2}}$ is the capillary length. Combining the last three **Equations (24)**, **(25)** and **(26)** in accordance with **Equation (23)** yields an asymptotic expression for the lateral capillary force:

$$F_{cap} = -\frac{d(\Delta W)}{dL} = -\pi\sigma \sum_{k=1}^{2} Q_k \frac{dh_k}{dL} \text{ x } \left[1 + O\left(q^2 c_k^2\right)\right] \qquad (27)$$

Paunov et al.[250,251,253] concluded from the previous calculation that the capillary force, turns out to be approximaterly equal to the half of the gravity contribution d(ΔW_g)/dL. Paunov introduced the following simplification for the height of the contact line, h_k:

$$h_k = h_{k\infty} + Q_j \ln\frac{2}{\gamma_e qL} \quad \forall \;\; k = 1,2; \;\; j \neq k; \quad c_k \ll L \ll q^{-1} \qquad (28)$$

$$h_{k\infty} = c_{k\infty} \sin\psi_{k\infty} \ln\frac{4}{\gamma_e q c_{k\infty}(1 + \cos\psi_{k\infty})} \quad \forall \;\; k = 1,2; \; (qc_{k\infty})^2 \ll 1 \qquad (29)$$

Here and subsequently the subscript "∞" denotes the value of the respective parameter for $L \to \infty$, ψ_k slope at the contact line for particle 1 and 2, $\gamma_e = 1.781072418$ is the constant of Euler-Masceroni and $K_0(x)$ is the modified Bessel function of zero order.

Now substituting **Equation (28)** and **(29)** into **Equation (27).** The next **Equation (30)** is obtained:

$$F_{cap} = 2\pi\sigma Q_1 Q_2 q K_1(qL)\left[1 + O\left(q^2 c_k^2\right)\right] \quad \forall \;\; c_k \ll L; \;\; k = 1,2 \qquad (30)$$

where $K_1(x)$ is the modified Bessel function of first order, for L > q^{-1} the function $K_1(qL)$ decay exponentially as seen in the procedure developed in **Equation (31)**.

$$K_1(qL) = \frac{1}{qL} + O[(qL)\ln(qL)] \;\; \forall \;\; qL \to 0$$

$$O[(qL)\ln(qL)] = \lim_{qL\to 0}(qL)\ln(qL) = \lim_{qL\to 0}\frac{\frac{1}{qL}}{\frac{1}{(qL)^2}} = \lim_{qL\to 0}(-qL) = 0 \qquad (31)$$

$$K_1(qL) = \frac{1}{qL}$$

The capillary interactions become important, **Equation (30)** reduce to

$$F_{cap} = 2\pi\sigma\frac{Q_1 Q_2}{L} \quad \forall \;\; R_k \ll L \ll q^{-1}; \quad k = 1,2 \qquad (32)$$

Equation (32) resembles Newton's law of gravity or Coulomb's law of electricity, with respect to the distance, L. The effective capillary charge is a quantity, which can be both positive and negative. Correspondingly, the capillary force (in **Equation (32)**) is attractive when $Q_1 \cdot Q_2 > 0$ and repulsive when $Q_1 \cdot Q_2 < 0$. The solution of **Equation (32)** needs an iterative procedure, more detail about it can be found in **Appendix E**[45,247].

In order to solve the theoretical capillary forces, by the iterative procedure presented in **Appendix E**, it is necessary to have as input data the following:

(1) The particles size and interparticle distance. These data may come from the HT-LSCM experiments,
(2) Data from bibliography such as surface tension[54] and particle and ceramic density[254]
(3) Contact angles between the particles and the steel and the particles and the ceramic-particle. The contact angles are obtained by HT-DSA experiments.

The attractive forces measured from HT-LSCM experiments will be compared with the theoretical capillary attractive forces in order to assure that the agglomeration behavior observed during the experiments come from capillary effects due to the meniscus deformation.

2.1.1.4.1 High-temperature drop shape analyzer (HT-DSA)

Wetting experiments, to find the contact angle between molten steel and a solid substrate, were conducted in a laboratory horizontal tube furnace, called high-temperature drop shape analyzer (HT-DSA). A high-temperature sessile drop system Krüss DSA HT10 (HT-DSA) is used to measure the wetting angles between liquid steel and solid substrates at temperatures of 1600 °C. The apparatus consists of a tube furnace and a CCD camera with a light source. The experiments are conducted in a horizontal tube furnace with a linear heating process (rate: 15°C/min). A holding time of 30 min at 1600°C is followed by cooling down at a rate of 10°C/min. Once the sample is melted, the measurements of the contact angle, as a function of temperature and time, start. They consist in a continuous monitoring of the shape of the sessile drop by a digital video camera connected to a computer, enabling automatic digital image analysis. The experiments are performed under a high purity argon atmosphere. More details regarding the device characteristics and the experiment set up can be found in literature[128,255]. The contact angle represents the average of six measurements taken during 30 minutes holding time at 1600 °C. Each of those six measurements represents the medium value between the right and the left contact angle.

The contact angles measured will be implemented as an input data into the theoretical capillary force. the HT-LSCM attractive forces measured from the experimental evaluation will be compared with the theoretical capillary forces. The comparison is needed to determine whether the NMI separate at the steel/ceramic interface due to capillary forces or not. Furthermore, HT-DSA results will help to explain the role of the wettability in the system 'NMI-Molten Steel-Refractory'.

2.1.2 Results

In the previous sections of this chapter, the two-step experimental set-up, the HT-LSCM experimental limitations and the experimental and theoretical evaluations have been presented. In the following sections, the experimental results are presented. First, the behavior of inclusions from Ca-treated steel are compared with the behavior of solid alumina inclusions coming from an ULC-steel. The inclusions from the steel are characterized by means of SEM-EDS. In the second part, the behavior of NMIs from a Ca-treated steel are investigated at three different interfaces: steel/Al_2O_3, steel/ZrO_2 and steel/MgO.

2.1.2.1 Set-up 1: NMIs characterization at the molten steel surface

The objective of the present study is to characterize the NMIs behavior at the molten steel, such as NMIs type, size, and behavior respect other inclusions. Here the NMIs of Ca-treated steel will be investigated and they will be compared with the behavior of NMIs at an ULC steel. The steel compositions are given in **Table 13.** The "set-up 1" given in **Section 2.1.1.1** is used here. It is previously known that the ULC presents a worse behavior respecting clogging than the Ca-treated steel.

Table 13. Investigated materials.

Steel	C %	Si %	Mn %	Al %	S %	Ca %
Ca-treated	0.15	0.02	1.07	0.04	0.004	0.0012
ULC	0.002	0.001	0.074	0.020	0.008	-

wt.-% = weight percentage

When the steel sample (Ca-treated or ULC) is heated up in the furnace and the liquidus temperature is reached, the steel melts partially (**Figure 23-a)** and **b)**) and inclusions start to emerge from the bulk to the steel surface as seen in **Figure 23-c)**. When two inclusions find each other at certain distance, a long-range attractive force may act between them inducing their agglomeration in order to reduce their surface energy. **Figure 23 a-c)** represent an example from the Ca-treated steel, but same behavior was observed for the ULC-steel.

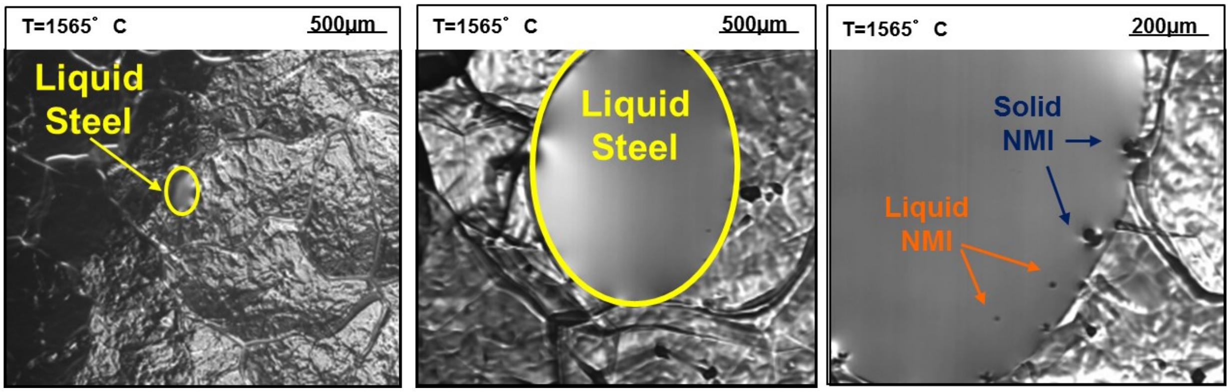

a) **b)** **c)**

Figure 23. Description of the NMIs from Ca-treated steel observation by means of HT-LSCM. **a)** The liquidus temperature of the steel is reached and the steel start melting, **b)** the liquid phase grows, and **c)** NMIs (solid and liquid) start to emerge from the bulk to the steel surface.

During the experiment with ULC steel samples, a big number of solid inclusions were observed swimming in the liquid steel. The experiments showed that alumina inclusions strongly attract to each other; the inclusions grow quickly by agglomeration in good agreement Yin et al.[6,145,146]. A cluster is shown in **Figure 24-a)**. SEM analyses were performed to the cooled samples and Al_2O_3 inclusions were found to be the predominant type as seen in **Figure 24-b)**. See more detail of the composition in **Table 14**.

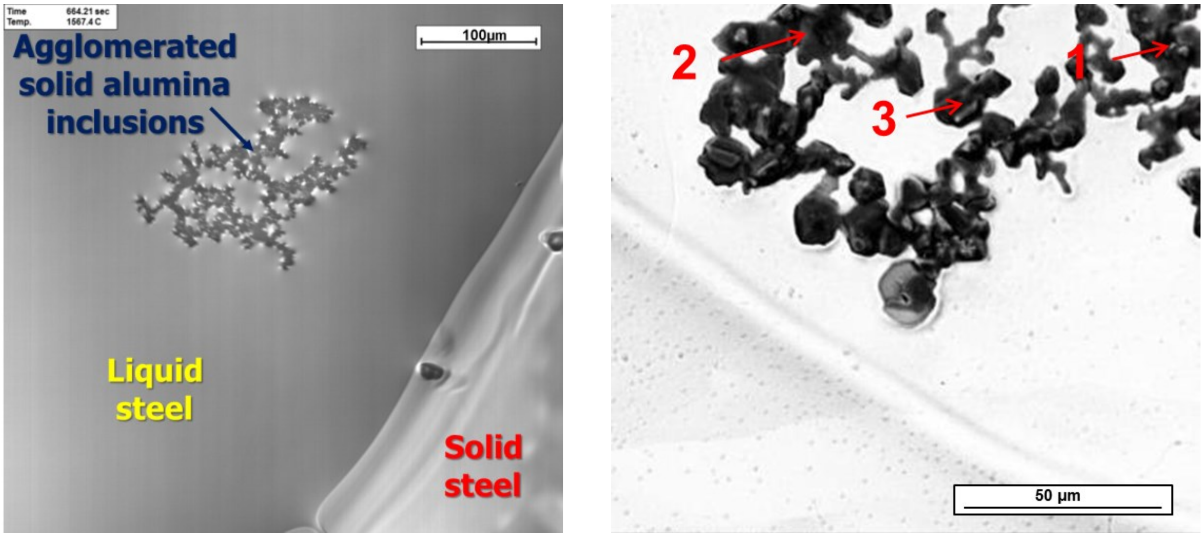

a) **b)**

Figure 24. NMIs at a ULC steel at **a)** HT-LSCM image and **b)** SEM-EDS analyses. The detailed NMIs composition is given in **Table 14**.

Table 14. SEM-EDS analyses of ULC-steel NMIs of **Figure 24-b)**.

N°	**O**	**Al**	**Mn**	**Fe**
	%	**%**	**%**	**%**
1	41.6	25.9	6.7	25.8
2	36.6	27.0	8.2	28.2
3	37.1	25.8	7.9	29.2
mass-%				

In contrast, the Ca-treated steel samples present a low number of NMIs. As it is observed in **Figure 23-c),** they have different shapes indicating a different NMIs morphology. Two different behaviors were observed:

(1) Attractive behavior between irregular inclusions as shown in **Figure 25-a),** and

(2) Globular inclusions swimming on the steel with no interaction between them as indicating in **Figure 25-b)**.

Interaction between irregular and globular inclusions was not observed.

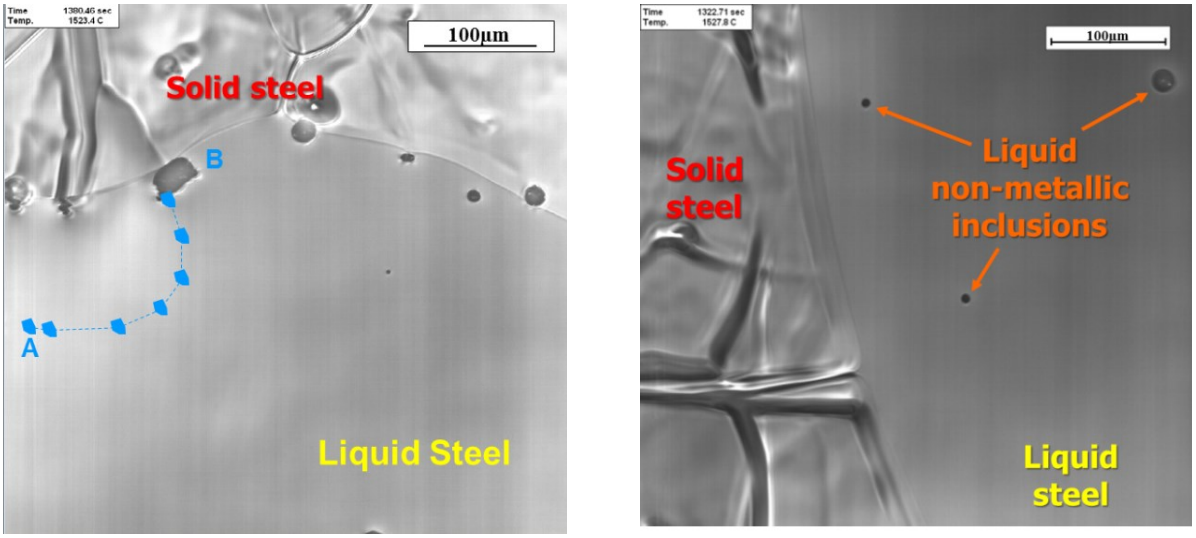

a) **b)**

Figure 25. Identification of NMIs during HT-LSCM experiment **a)** irregular inclusions and **b)** globular inclusions in a Ca-treated steel.

As previously mentioned, a different NMIs morphology was observed during the Ca-treated experiments. Thus, a SEM-EDS investigation of the samples after HT-LSCM was carried out to find out the type of inclusions observed. Representative examples of detected inclusions and the corresponding chemical compositions are given in **Figure 26** and **Table 15**, respectively.

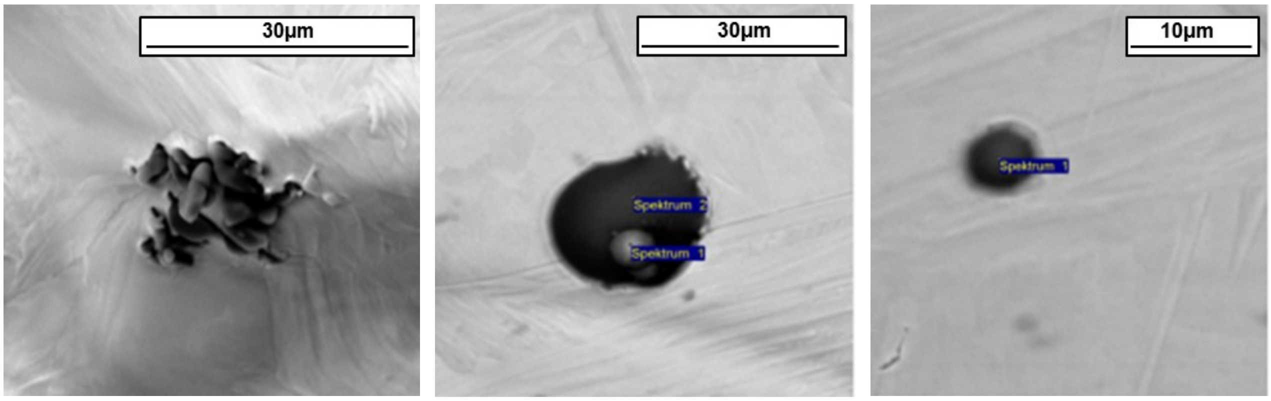

a) **b)** **c)**

Figure 26. SEM-EDS investigation of the steel samples after HT-LSCM. Three types of inclusions are observed: **a)** Solid alumina inclusion, **b)** Complex inclusion: Liquid Ca-Al-O with solid areas of Ca-S, and **c)** Liquid Ca-Al-O inclusions. The detailed composition is given in **Table 15**.

Table 15. SEM-EDS inclusions composition of **Figure 26** (in mass-%).

NMIs		**O** **%**	**Al** **%**	**S** **%**	**Ca** **%**	**Mn** **%**	**Fe** **%**	**Phase**
a)	**1**	61.4	30.5		0.4	0.4	7.3	Al-O with traces of Ca, Mn, Fe
b)	**1**	11.9	0.5	39.9	45.1	0.7	2.1	Light: Ca-S-O
	2	46.9	28.8	0.3	20.3	2.7	1.0	Dark: Al-Ca-Oxide
c)	**1**	43.8	30.6	1.4	16.7	1.2	6.3	Dark: Al-Ca-Oxide
mass-%								

Three types of inclusions were observed:

(1) Solid alumina inclusions,
(2) complex inclusions composed by two phases: liquid calcium aluminate with solid CaS precipitates, and
(3) liquid calcium aluminates.

The NMIs are identified by their shape: Irregular inclusions will be considered to be solid and the globular ones as liquid. Complex, called as well semi-liquid inclusions, cannot be easily identified during the HT-LSCM investigations (as already mentioned in **Section 2.1.1.2**); therefore, they will be considered as liquid-type if their shape looks globular or solid-type if they look irregular during the pictures evaluation. Due to possible oxygen sources, the NMIs have the tendency to react with the oxygen and formed more solid alumina with traces of S, Mn, Ca. In any case, it is clearly observable that the liquid inclusions do not show high tendency to agglomerate in comparison with the solid ones.

There is a great difference between these two steels. In the ULC steel a high number of solid alumina inclusions presenting a high tendency to agglomerate are observed. However, in the Ca-treated steel, a lower number of inclusions are noticed. In addition, different NMI morphologies are recognized. Due to the lower number of inclusions observed and their different types, lower numbers of interactions between inclusions are seen.

Each experiment was evaluated following the procedure given in **Section 2.1.1.3**. In this case the 'guest' and the 'host' particles will be NMIs of the same size. The 'host particle' always remains in the same position during the attraction. The HT-LSCM attractive force, given by **Equation (27)**[6,46,145,146] is calculated. The results of the attractive force between a pair of equal solid NMIs with the same size from the two different steel grades are plotted in **Figure 27**. From these results, it can be seen that the attractive force increases with the NMIs size for both steel grades and that the attractive force is stronger for NMIs in the ULC-steel than in the Ca-treated steel. A possible explanation for this observed difference is the NMIs' wettability.

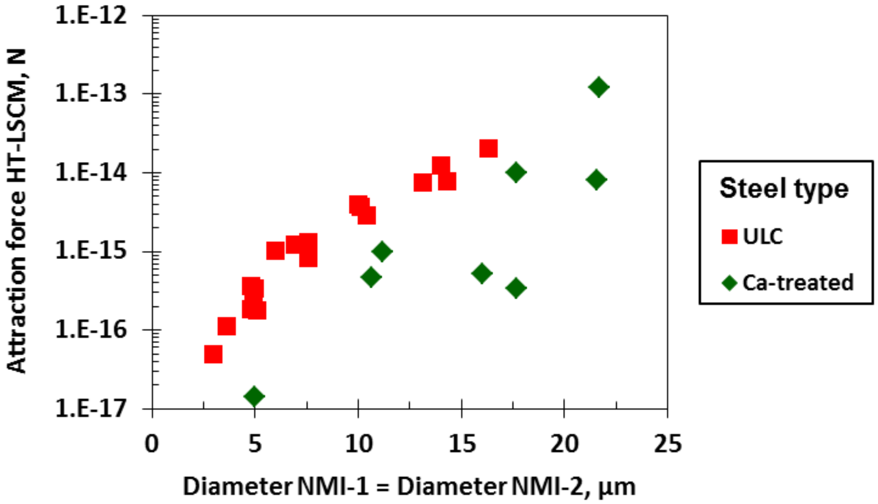

Figure 27. HT-LSCM measured attractive force between two equal solid NMIs from ULC-steel and Ca-treated steel.

For that reason, HT-DSA experiments have been carried out between these two steel grades and an alumina substrate. As a result, the contact angle between the NMIs and the steel is obtained. More details regarding HT-DSA are found in **Section 2.1.1.4.1**. In both cases, the contact angle measured corresponds with partial non-wetting; however, the contact angles measured differ from 98 ± 5.7 deg. between Ca-treated molten steel and Al_2O_3, 137 ± 10 deg. between ULC steel and Al_2O_3. The contact angle difference can be observed in **Figure 28-a)** and **b)**.

From the results presented in **Figure 27** and **Figure 28**, it is observed that there is a relation between the attractive force and the contact angle. Thus, the capillary force is weaker in a Ca-treated steel due to the lower contact angle between the NMIs and the steel than in a ULC-steel. The NMIs, which are better wetted by the molten steel, present a smaller meniscus, leading to weaker attractive forces than inclusions with higher contact angle. In addition, bigger inclusions-pairs will be attracted to each other stronger.

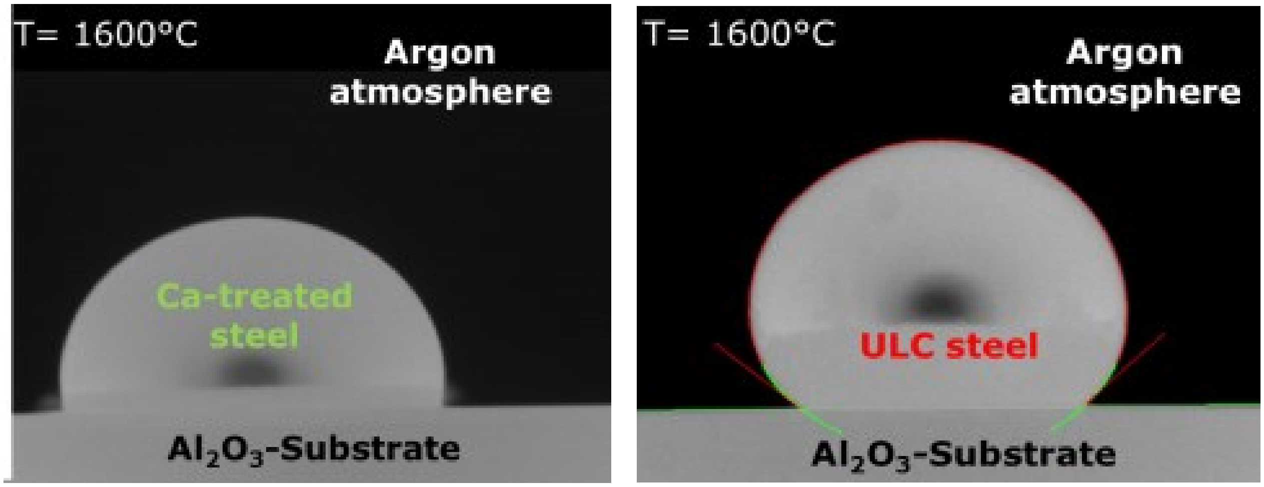

a) **b)**

Figure 28. HT-DSA measurements of contact angle between Al_2O_3-substrate and **a)** Ca-treated steel and **b)** ULC-steel.

The comparison of two steels presenting a different clogging behavior during continuous casting have been investigated for the first time by means of HT-LSCM. A clear difference between the NMIs contained in the steel and their behavior was observed during the experiments. Furthermore, an extraordinary accordance of HT-LSCM observations and the wettability behavior of both steels measured in the HT-DSA is found. From these experiments, three important facts can be outlined here:

(1) **Characterization of NMIs** by SEM-EDS analyses: In ULC-steel only alumina inclusions were found, whereas in Ca-treated steel solid, semi-liquid and liquid inclusions were observed. The various types of NMIs in a steel grade make the interpretation of the experiments more difficult.

(2) **NMIs size:** Bigger inclusions will be attracted with higher force.

(3) **NMIs wettability:** The attraction force between two solid alumina inclusions, in two different types of steel grades is probed to be different. This is due to the different wettability of the NMIs with the steel.

In good agreement with the previous knowledge, the clogging tendency of the ULC steel will be worse than the Ca-treated steel. Thus, the inclusions type, size and contact angle influence the clogging tendency of the NMIs at the steel/refractory interface.

2.1.2.2 Set-up 2: NMIs behavior at different molten steel/ceramic interfaces

In the previous section, the NMIs from steel were characterized and their attractive behavior was investigated. In this section, an exogenous ceramic is introduced in order to simulate the separation of NMIs at a nozzle. Here, the behavior of NMIs from a calcium treated steel at the interface between liquid steel and Al_2O_3, ZrO_2 and MgO is investigated by application of "Set-up 2" (see **Section 2.1.1.1** for more detail). **Table 16** gives more information about the materials chosen. The steel used is the same as in the previous section.

Table 16. Investigated materials.

Ca-treated Steel composition						**Ceramic-particle ECD**		
C %	**Si %**	**Mn %**	**Al %**	**S %**	**Ca %**	**Al_2O_3 µm**	**ZrO_2 µm**	**MgO µm**
0.15	0.02	1.07	0.04	0.004	0.0012	400	350	500-400
[wt.-%] = weight percentage						ECD= Equivalent Circle Diameter		

Figure 29 shows a typical heating cycle for the NMIs observation in the molten steel. At liquidus temperature, the steel starts to melt forming a meniscus around the exogenous ceramic and inclusions emerge from the bulk to the steel surface. Various screenshots during the experiments with Al_2O_3, ZrO_2 and MgO ceramics are shown.

Three representative examples of the experimental evaluation of every kind of ceramic-particle used are presented on **Figure 30-a), b)** and **c)**. During the experiment is observed that solid NMIs ('guest particle') tend to agglomerate at the surface of the exogenous ceramic-particle ('host particle'), when they are found to be at certain distance from each other. The position of the 'guest particle' with respect to the ceramic is measured, assuming that the 'host particle' is always quiescent when the attraction takes place. The HT-LSCM attractive force is given by **Equation (27)**[6,46,145,146]. More details on the quantitative evaluation of the experiments are given in **Section 2.1.1.3**.

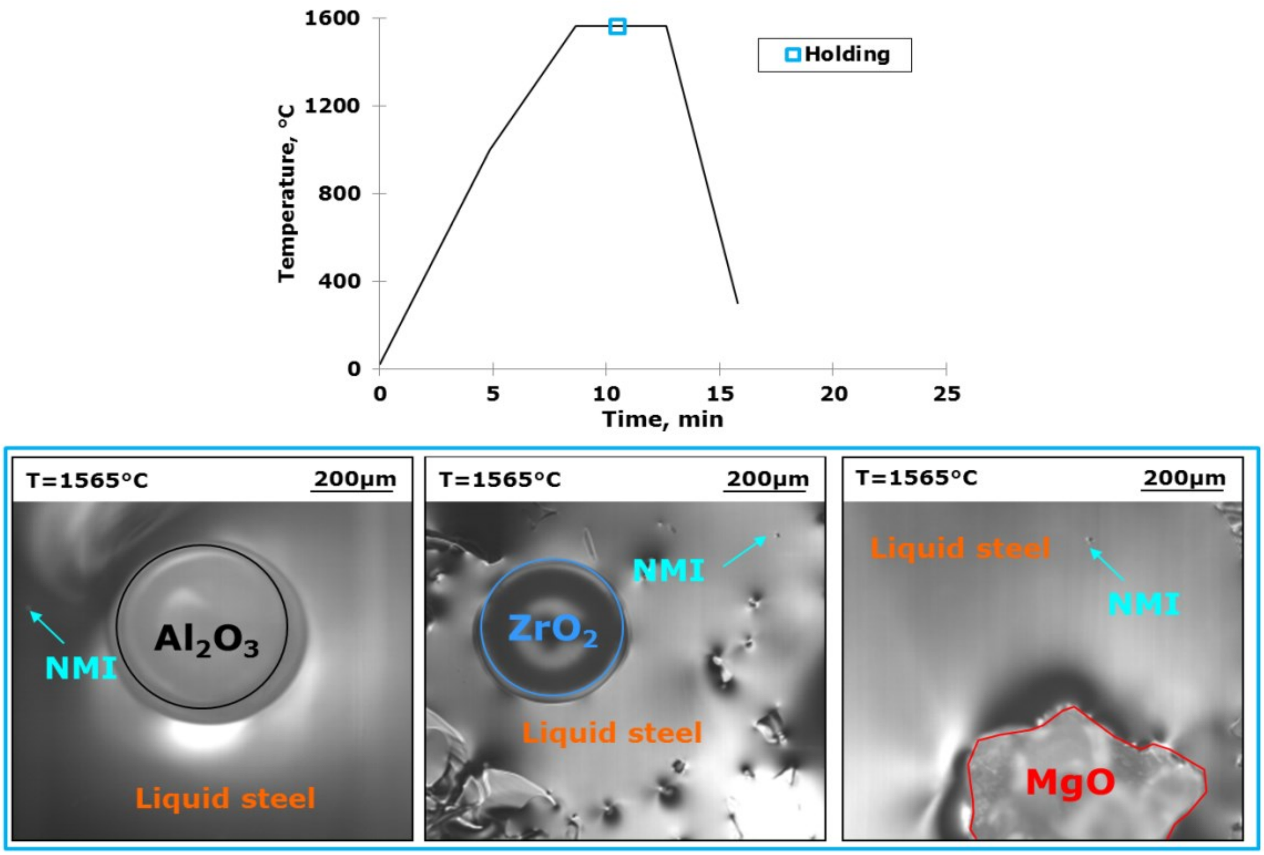

Figure 29. Experimental heating cycle, with screenshots during holding for the three types of experiments carried out (Al_2O_3, ZrO_2 and MgO).

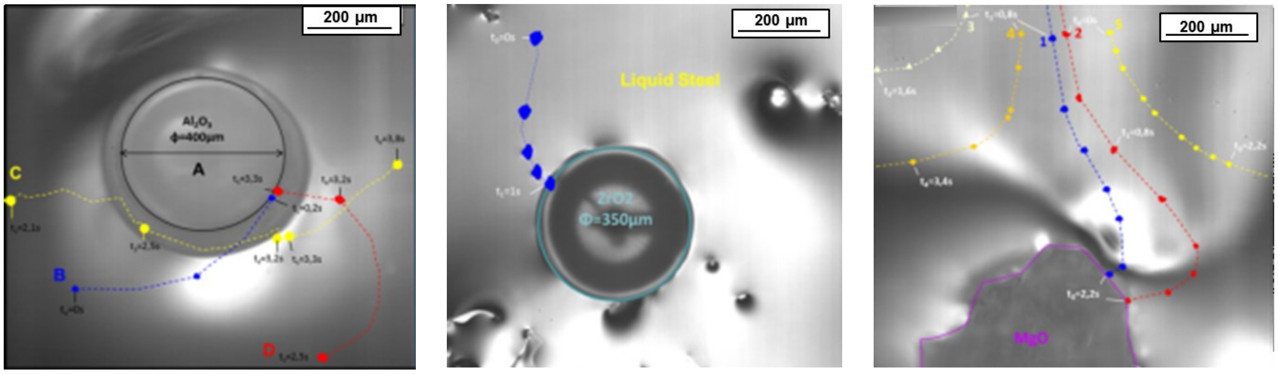

a) **b)** **c)**

Figure 30. Videos analyzed frame by frame ready to be evaluated for a) Al_2O_3 (A), b) ZrO_2 (Z) and c) MgO (M).

Two parameters are analyzed and discussed here:

(1) **NMI wettability**: solid and liquid inclusions from Ca-treated steel are investigated at a molten steel/ Al_2O_3 interface, and

(2) **Refractory wettability**: solid inclusions from Ca-treated steel are investigated at different steel/ceramic interfaces, i.e., Al_2O_3, ZrO_2 and MgO.

2.1.2.2.1 NMI wettability

As already mentioned in **Section 1.1** the behavior of solid and liquid inclusions in molten steel regarding their adhesion at a steel/refractory interface is different. **Figure 31 a-e)** resembles this different behavior[147]. In **Figure 31-a)** a solid particle B rapidly attaches to the particle A, after 2 seconds a liquid particle C appears. The trajectory of particle C is observed (see **Figure 31b)-e)**), it moves towards particle A, but instead of attaching, particle C keeps moving close to A and after some time, it moves away. In **Figure 31-b)** a solid particle D is observed; after 0.8 seconds particle D attaches to A (see **Figure 31-c)** and **-d)**). Particle B and D present an irregular shape and they are assumed to be solid at the experimental temperature, whereas particle C present a globular shape and is taken as liquid. A clear difference on the different behavior of the inclusions in function of its morphology (solid or liquid) is observed.

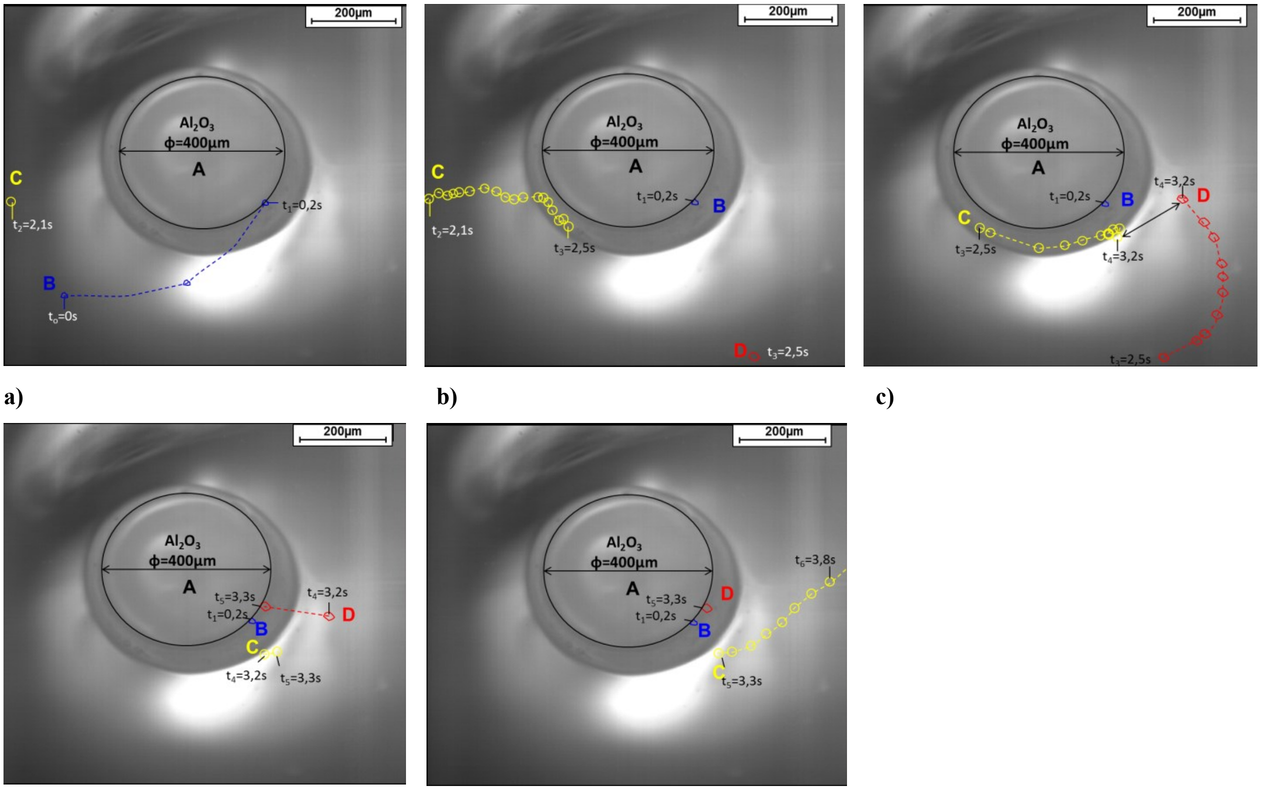

a) b) c)

d) e)

Figure 31. a)-e) Show the trajectory of three non-metallic inclusions B, C and D in relation to particle A

In **Figure 32-a)** the trajectory of different liquid inclusions at the steel/ceramic interface is plotted. The liquid NMIs approach the ceramic but at certain distance which is found to be between 20-100 µm. They approach the spherical ceramic-particle but they do not separate at the steel/ceramic interface.

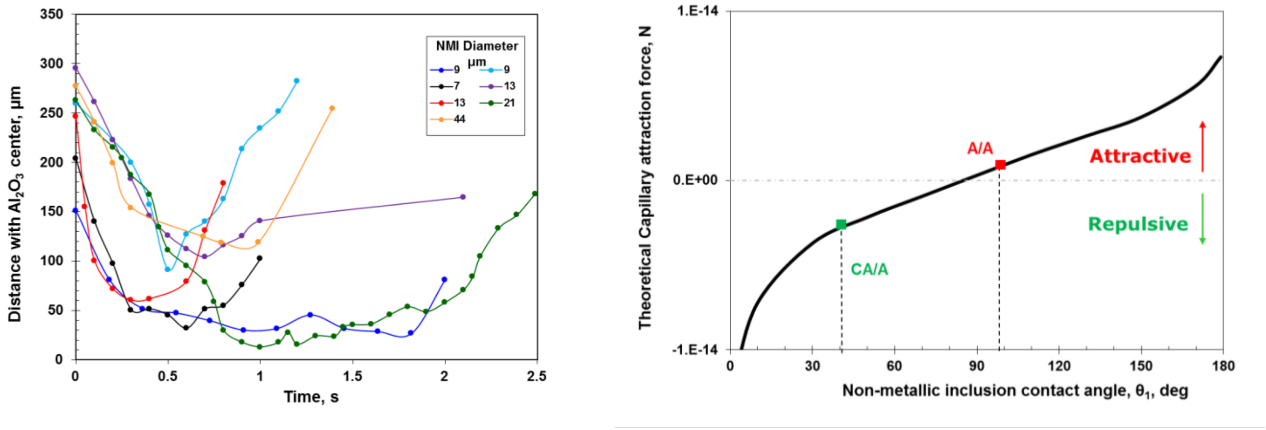

a) **b)**

Figure 32. a) Liquid NMIs trajectory from the Al_2O_3 center.and **b)** Theoretical capillary attraction force

The theoretical capillary force between a NMI and an Al_2O_3 ceramic with 98 deg. contact angle (see **Figure 28-a)**) has been calculated in **Figure 32-b)**, by solving **Equation (40)** under the iterative procedure given in **Appendix E**. Point CA/A indicates the capillary force between a liquid calcium aluminate with approximately 40 deg. contact angle (see **Table 3**). This point indicates that there is repulsive capillary force acting between these two bodies due to their different wettability behaviors. This justify, that no separation at the molten steel/ceramic interface is observed during the experiments.

Whereas Point A/A in **Figure 32-b)** indicates that the capillary force between a solid alumina inclusion with 98 deg. contact angle (see **Figure 28-a)**) is attractive. Thus, alumina inclusions tend to separate at the steel/ceramic-particle interface, but not the liquid calcium aluminates. These tendencies were observed during the HT-LSCM experiments and these effects were resembled in **Figure 31**.

The cooled samples were investigated under SEM-EDS analyses. The objective was to observe which kind of inclusions were adhered at the molten steel/ceramic interface. At the surface of the ceramic only solid Al_2O_3 inclusions (with traces of Ca, S, Mn and/or Fe) were found to be agglomerated but no liquid inclusions, as expected from **Figure 31** and **32**. Two examples of solid inclusions agglomerated at the ceramic surface are given in **Figure 33-a)** and **b)** by means of SEM-EDS.

Liquid and solid NMIs in this Ca-treated steel have a wetting and a non-wetting behavior with the steel, respectively. Their wettability behavior is the reason for their different behavior at the molten steel/ceramic interface. The HT-LSCM observations are in accordance with the theoretical capillary force calculations and give a good support to the thermodynamic calculations given in **Section 1.2**.

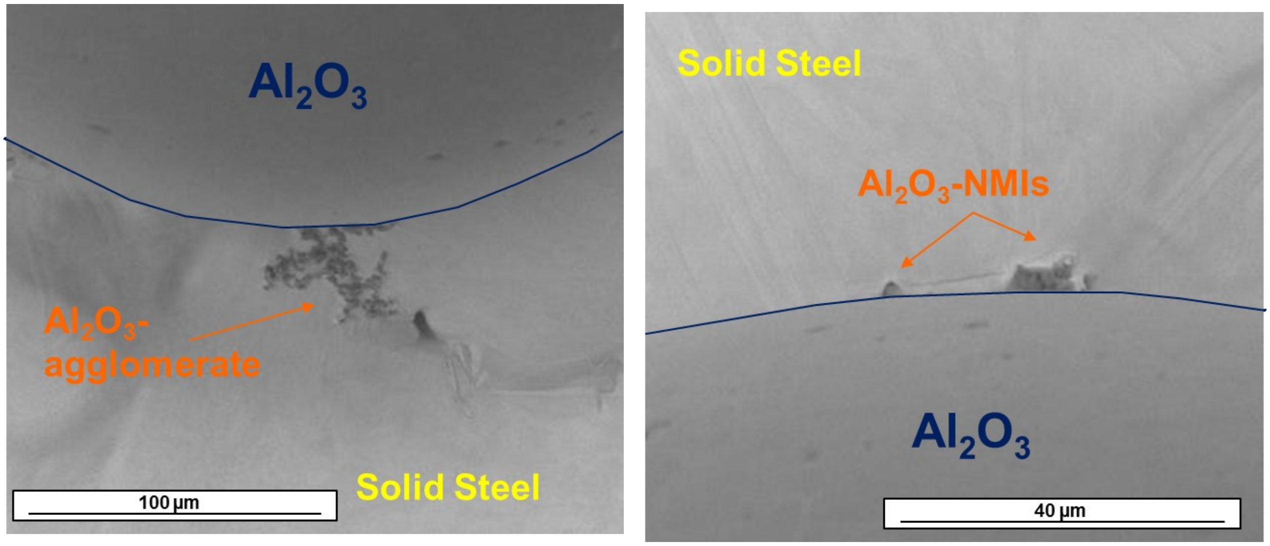

a) b)

Figure 33. Alumina inclusions agglomerated at the Al_2O_3 interface by means of SEM-EDS analysis.

Furthermore, these observations state the importance of the Ca-treatment of steel as a clogging countermeasure. More details regarding the Ca-treatment to modify deoxidation products is given in **Section 1.3.2**. The calcium reacts with alumina in the steel forming liquid calcium aluminates, which are less likely to form agglomerates at the steel/refractory interface, since they may feel a repulsive capillary force due to their wetting behavior with molten steel.

2.1.2.2.2 Ceramic wettability

Now the ceramic-particle is changed. The objective is to observe the behavior of the NMIs from Ca-treated steel towards three exogenous ceramic-particles:

1. Al_2O_3,
2. ZrO_2, and
3. MgO.

The materials details are given in **Table 16** and the "Set-up 2" is (see **Section 2.1.1.1** for more detail).

When the steel disc is melted, solid alumina particles, between 4-30 µm ECD-diameter, start to emerge and swim at the molten steel surface. These solid inclusions tend to approach the exogenous ceramic (Al_2O_3, ZrO_2 or MgO) and rapidly adhere at its surface as already introduced in the previous section. The experimental results are evaluated following the procedure explained in **Section 2.1.1.3**. The HT-LSCM attractive force experienced between the inclusions and the spherical ceramic-particle is calculated.

In **Figure 34**, the attractive force experienced when a 14 µm ECD-diameter inclusion approaches to Al_2O_3, ZrO_2 or MgO is represented. In the three cases, it is observed that when the 'guest particle' starts approaching the exogenous body, its force rises before separation. This means that the inclusions experience an attractive force at certain distance from the ceramic-particle. Furthermore, the attraction distance, which is observed right before separation happens, depends on the ceramic-particle chosen; being the highest attractive distance for MgO and the smallest for Al_2O_3.

The attractive force experienced by solid alumina inclusions of certain size before separation is plotted in **Figure 35.** Bigger inclusions suffer a stronger attractive force than smaller ones, i.e., a 5 µm inclusion experiences an attraction force within 10^{-16}-10^{-15} N, whereas if a 16 µm inclusion 10^{-14}-10^{-13} N. In addition, the attraction force is found to be affected by the used ceramic-particle, and it can be listed as follows in ascending order: NMI/Al_2O_3 < NMI/ZrO_2 < NMI/MgO. The different shape of the MgO ceramic-particle used might induce a non-stable meniscus around it, but this was not taken into account during the investigation. **Figures 34** and **35** show that the attractive force and the attractive distance depend on the particle size as well as on the ceramic-particle type.

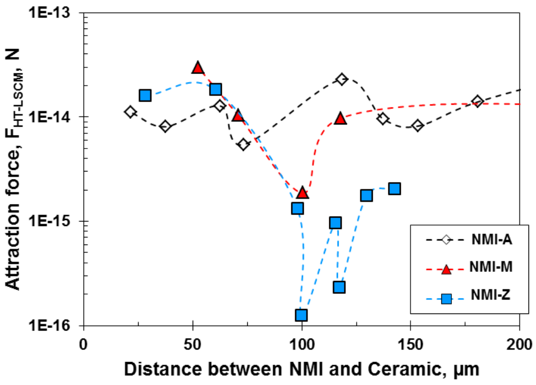

Figure 34. Selected example of the variation of the force with the distance between a ~14µm inclusion and Al_2O_3, ZrO_2, and MgO.

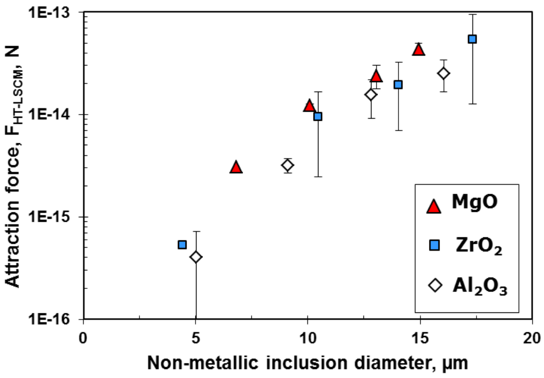

Figure 35. Observed attraction force in dependence of inclusions size and the exogeneous ceramic-particle (Al_2O_3, ZrO_2, and MgO).

It is observed that these solid inclusions experience a long-range attractive force. However, it is necessary to confirm whether the separation is caused due to capillary effects or due to other forces such as fluid flow in the surface of the melt. For that purpose, a comparison between the HT-LSCM observed data and the theoretical capillary force calculations is done. For the calculation of the theoretical capillary force (Explained in **Section 3.1.1.4** and **Appendix E**) different input data are needed:

(1) Data collected during HT-LSCM experiments (particle size and interparticle distance),

(2) data from bibliography, such as surface tension[54] and material densities[254], and

(3) contact angles between NMI or refractory and molten steel by HT-DSA.

Three different HT-DSA experiments were performed under a well-controlled atmosphere between:

(1) Ca-treated steel droplet and an alumina substrate,
(2) Ca-treated steel droplet and a zirconia substrate and
(3) Ca-treated steel droplet and a MgO substrate prepared from a MgO brick produced in a refractory plant.

More details regarding the HT-DSA are given in **Section 2.1.1.4.1**. The summary of the HT-DSA results is presented in **Figure 36.** In all cases, the contact angle measured corresponds with partial non-wetting; however, the contact angles measured differ from 98 ± 5.7 deg. between molten steel and Al_2O_3, 106 ± 10 deg. between molten steel and ZrO_2 to 137± 9 deg. between molten steel and MgO. The contact angle represents the average of six measurements taken during 30 minutes holding time at 1600 °C. Each of those six measurements represents the medium value between the right and the left contact angle.

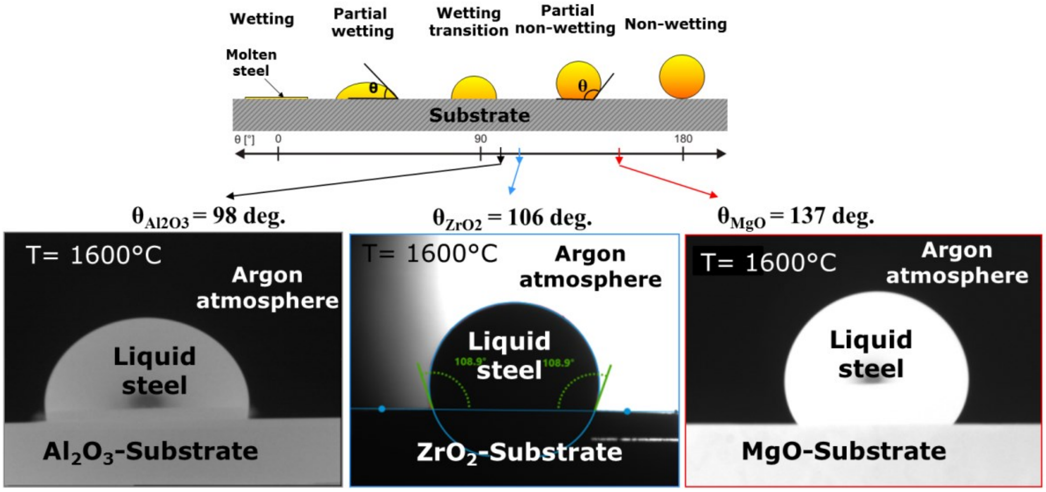

Figure 36. Screenshot during HT-DSA experiment for Ca-treated steel and Al_2O_3(left image), Ca-treated steel and ZrO_2 (central image), and Ca-treated steel and MgO substrate (right image).

With all the input data available in **Table 17,** the theoretical capillary force is calculated and compared with the HT-LSCM attractive force calculated for different inclusions sizes in **Figure 37**. The solid line indicates the theoretical capillary force and the dots represent the HT-LSCM experimental calculations for each of the three studied cases: Al_2O_3 (A), ZrO_2 (Z), and MgO (M). The theoretical capillary force is approximately one order of magnitude higher than the HT-LSCM calculated force, being for Al_2O_3-Al_2O_3 the most accurate. These results indicate that the HT-LSCM attractive forces observed may come from capillary effects due to the formation of a meniscus around the exogenous ceramic-particle. As already mentioned in the HT-LSCM limitations (see **Section 2.1.1.2**), the experimental evaluation introduces some error regarding the video evaluation which could explain the difference between the HT-LSCM data and the theoretical calculations. From the theoretical data, increasing attraction forces are observed with increasing inclusion size as well as by changing the ceramic, in ascending order listed as follows: solid inclusion/ Al_2O_3 < Solid inclusion/ZrO_2 < Solid inclusion/ MgO. This confirms that the HT-LSCM observations are in good agreement with the theoretical understanding of the capillary phenomena.

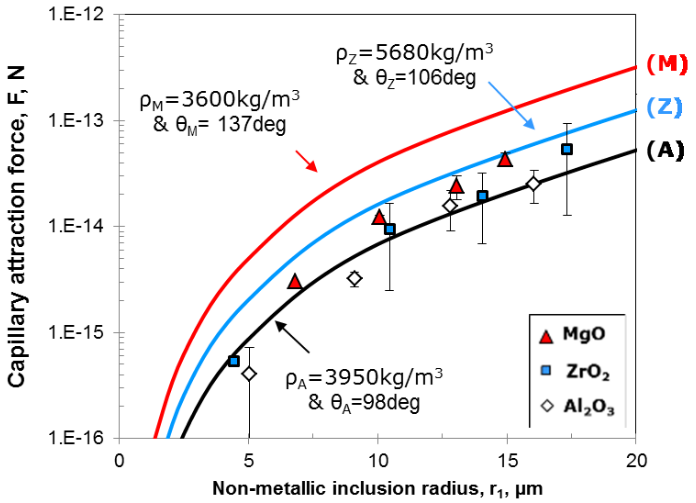

Figure 37. Theoretical capillary force (solid line) vs. HT-LSCM calculated force (points) for different inclusions sizes at different ceramic/steel interfaces. (Al_2O_3 (A), ZrO_2 (Z), and MgO (M)).

Table 17. Data for the calculation of the theoretical capillary attraction force solid line.

Calculation Figure 37.	Steel	Ceramic-particle #2				Separation	Non-metallic inclusion #1		
	σ N/m	Type	d_2 µm	θ_2 deg.	ρ_2 kg/m^3	L µm	d_1 µm	θ_1 deg	ρ_1 kg/m^3
	1,6	(A)	400	98	3950	50	{2-40}	98	3950
		(M)	500	137	3600				
		(Z)	175	106	5680				

(A) = Al_2O_3 and (M)= MgO

For the selected steel in the HT-LSCM investigation (see **Table 16**), the separation of inclusions would be weaker at an Al_2O_3-based refractory with a contact angle of 98 deg. than at a MgO-based refractory with a contact angle of 137 deg. since the attractive forces are smaller. This investigation resembles the importance of the material wettability in relation with clogging phenomena. These results agree qualitatively with the thermodynamic calculations presented in **Section 1.2**, where a better wetted refractory was suggested in order to reduce the separation tendency of the alumina inclusions at the SEN wall.

For the first time, the influence of the separation tendency of NMIs at a steel/refractory interface has been investigated in detail by means of HT-LSCM. The influence on the attraction force of the ceramic-particle type as well as the NMI morphology has been measured. The results show an extraordinary correspondence with the wettability behavior of the materials involved, that was measured by HT-DSA. The following facts can be seen:

(1) **NMIs morphology:** Solid and liquid inclusions behave differently regarding its separation at steel/ceramic interfaces.
(2) **NMI size:** The attractive forces increase with the NMI size.
(3) **Ceramic-particle wettability:** The wettability of the ceramic-particle influences the attraction force magnitude. Ceramic-particles good wetted by molten steel show lower attractive forces.

2.1.3 Discussion

The HT-LSCM has been used as an indirect technique to observe the behaviour of particles at steel/refractory interfaces. The results have been cross-checked with measured wetting angles at the interface between steel/refractory and steel/inclusion. The results stand in an astonishing accordance:

(1) **NMIs population:**

  a) **Morphology:** The morphology of the NMIs (liquid or solid) influences its behavior towards the separation at a steel/ceramic interface. The liquid inclusions and the ceramic-particles present a wetting and a non-wetting behavior with the molten steel, respectively. Their opposite wettability behavior, induces an opposite meniscus shape around the bodies being the reason for the existance of a repulsion force. Whereas solid inclusions present an attractive capillary force that induces its separation at the steel/ceramic interface. These observations agree with the thermodynamic calculations shown in **Figure 5** and **6**.

   b) **NMI size:** the attractive forces are observed to increase with the NMI size for all studied cases.

(2) **Refractory:** The change of the wettability of the system, induced by the exchange of the ceramic-particle from MgO to ZrO_2 and Al_2O_3, showed a reduction of the attractive forces for the same inclusions' type. Indicating a weaker separation towards the SEN-wall for the same inclusion type. This behavior was observed for the investigated Ca-treated steel; however, for ULC steels the tendency might be the opposite since the contact angle of the steel with Al_2O_3 is already 137 deg. and with ZrO_2 110 deg.

(3) **Steel grade:** The calcium treated steel was found to have a 98 deg. contact angle with alumina, whereas ultra low carbon (ULC) steel presents a contact angle of 137 deg. with alumina. The steel deoxidation and possible modification of inclusions by Ca-treatement may lead to different clogging tendencies for the steel since this treatments condition the wettability and NMIs' population.

Thus, the three elements of the system “NMI-Molten Steel-Refractory” need to be considered in order to apply the best clogging countermeasures. The NMIs' population and distribution, the NMIs and refractory wettability and the steel grade are key parameters for the study of the clogging tendency due to the attachment at the SEN wall of deoxidation produts.

The combination of the HT-LSCM and HT-DSA permits the connection between contact angle and the observation of different behavior of the NMIs in the molten steel. And therefore, an added value to the wettability studies is given regarding clogging tendency of different steel grades.

3 NMIs detachment from a steel/refractory interface

In this chapter, a detailed model is derived to predict the critical conditions needed for detachment of NMIs from the nozzle wall. This model is based on the local hydrodynamic conditions combined with the specific interfacial properties in the system NMI-steel-refractory. Three detachment criterions are developed in function of the force balances in normal and parallel directions and the torque moment of the NMI at the steel/refractory interface. The detachment model is implemented to investigate how the interfacial properties of the system NMI-steel-refractory may influence the adhesion or detachment of a NMI at the steel/ceramic interface. Three systems are studied here:

(1) Steel-refractory
(2) Steel-NMI
(3) NMI-steel-refractory

3.1 Detachment criteria

Based on the force contributions already introduced in **Section 1.2** (see **Figure 11**), three criteria in terms of force and torque balances determine whether an inclusion in contact with the wall will be able to be detached from the wall or not. The model comprises the following assumptions and simplifications:

(1) The source of the clogging deposit comes from the agglomeration of small oxidic inclusions at the nozzle wall.
(2) The small inclusions with a spherical shape are attached to the wall by a fluid cavity. The source of the cavity is already present in the system, meaning that no argon injection is considered for the analysis.
(3) The nozzle wall is assumed to be flat and smooth.

3.1.1 Normal movement

For a detachment of the inclusion particle from the wall in the normal direction, according to the force balance

$$F_A = F_L \tag{33}$$

the lift force must overcome the adhesion force. In other words, the inclusion will be lifted off if the normal ratio (R_N) is greater than unity, as shown in the equation

$$R_N = \frac{F_L}{F_A} \tag{34}$$

Since the lift force is directly dependent on the fluid flow conditions next to the wall, any increase in velocity at the near-wall region will increase the normal ratio.

3.1.2 Parallel movement

In **Equation (35)** the parallel movement of the inclusion is analyzed. For that to happen, the resultant tangential force should overcome the friction between the surfaces. The frictional force, F_F, is proportional to the normal force exerted by each surface on the other, directed perpendicular to the surface.

$$(F_D - F_B) = F_F = \kappa_S \cdot F_n = \kappa_S \cdot (F_A - F_L) \tag{35}$$

$$R_P = \frac{(F_D - F_B)}{\kappa_S (F_A - F_L)} \tag{36}$$

Where F_n is the normal force (N), κ_s is the coefficient of friction, and R_p is the parallel ratio. The criterion indicates that the particle will be detached when the parallel ratio is greater than unity. The possibility of a liquid phase acting as a bridge might reduce the dry frictional force, increasing the parallel ratio.

3.1.3 Torque moment

The torque moment defines the tendency of a force to rotate an object about an axis[256]. Drag and lift forces exerted on the inclusion might induce a torque on the particle.

$$aF_A = 1{,}4 r_1 F_D + aF_L - r_1 F_B \tag{37}$$

$$a = \left(\frac{6\pi\sigma r_1^2}{K}\right)^{\frac{1}{3}} \tag{38}$$

$$K = \frac{4}{3}\left(\frac{1-\upsilon_1^2}{E_1} + \frac{1-\upsilon_2^2}{E_2}\right)^{-1} \tag{39}$$

where r_1 is the particle radius (m), a is the contact radius, K is the elastic constant (Pa) and ν_i, E_i (i=1,2) are the Poisson's ratio and Young's modulus (Pa) of a particle and a surface, respectively[256]. Value 1.4 was chosen for Shi et al.[256] to calculate the drag force at the maximum.

An inclusion will be detached when the torque ratio, R_T, becomes larger than unity, meaning that the detachment forces acting on the inclusion are stronger than the adhesion force. The fluid flow conditions next to the wall strongly influence the torque ratio given by **Equation (40)**.

$$R_T = \frac{1{,}4 r_1 F_D + a F_L - r_1 F_B}{a F_A} \tag{40}$$

The model predicts the critical conditions needed for detachment of NMIs from the nozzle wall. The model will be implemented into three systems: Steel-refractory, Steel-NMI and NMI-steel/refractory.

3.2 Steel-refractory

Steel grades that possess an increased tendency to clog are ones containing elements with high affinities for oxygen, sulfur, or nitrogen. Examples of such elements are aluminum, rare earth metals, calcium, or titanium and these are able to form solid non-metallic inclusions, such as Al_2O_3 or CaS, in the liquid steel[257]. Special importance over the years is given to clogging caused during the production of Al-killed steels[12,19,20,27,28,32,38,40–42,73,98,123,139,258–261]. In these steels, the solid aluminum oxides formed due to deoxidation already in the liquid steel during tapping and subsequent ladle treatment. These alumina particles within a size of 1-10 μm, are transported from the bulk region to the boundary layer eventually may come in contact with the nozzle refractory. They adhere to the wall by interfacial forces, caused by a fluid cavity formation around the contact point. Their high contact angle of 137° with molten steel is believed to be the reason that these steels have a high risk of clogging the SEN.

In order to observe how the ceramic phase may affects the clogging problem of steel containing solid alumina inclusions, the detachment model presented in **Section 3.1.1** will be solved for a 5 μm alumina inclusion with 137 deg. with molten steel at different steel/ceramic interfaces.

In **Figure 38**, the adhesion force calculated between a 5 µm diameter aluminum oxide at different steel/refractory interfaces according to **Equations (2-7)** is presented. At Case (A-A) the alumina particle is adhered at an alumina-based refractory of 137 deg. of contact angle with molten steel. A reduction of the adhesion force presented in Case (A-A) is possible under the assumption that the new nozzle material chosen has a better wettability for liquid steel than the alumina-based refractory used before. As a compromise, a zirconia-based refractory was chosen for this analysis because it has a contact angle of 100°. In Case (Z-A) of **Figure 38**, the reduction of the adhesion force due to the selection of a refractory better wetted with steel is represented. The selection of refractory materials better wetted by molten steel was mentioned in **Section 1.3** as one of the possible clogging countermeasures.

Sasai et al. [43] and Mizoguchi et al.[48] suggested a mechanism by which liquid FeO could act as a binder for the alumina particles. Kang et al.[37] emphasized the importance of the interfacial conditions in contraposition with the bulk conditions. In the interface between steel and the refractory, a local increase of the oxygen concentration may lead to steel re-oxidation. In literature[43,47–49], great importance is given to the formation of FeO as a binder for the reduction of the adhesion of alumina particles in the tundish. Since the FeO formation is rather unusual on an industrial scale if there is no reoxidation, this mechanism of a liquid phase present might be compared with the usage of refractories which may react with the alumina inclusions to form low-melting eutectic phases explained in **Section 1.3**.

The formation of a liquid phase as an adhesion bridge is related to the reduction of the surface tension between steel and the fluid phase inside the cavity. The surface tension between molten steel and a gas or vapor contained in the cavity is considered to be approximately 1.8 N/m. However, the surface tension between molten steel and liquid slag phase is approximately 0.6 N/m[54,262]. Therefore, if a liquid bridge is formed, the adhesion force between an aluminum oxide inclusion and the new nozzle wall is reduced, as shown in the Case (L-A) of **Figure 38**, from 22.5 µN from Case (A-A) to 4 µN with the liquid binder. The presence of a liquid bridge reduces the adhesion force in comparison to the gaseous case, and a further reduction in adhesion force would be expected if the solid inclusion becomes liquid or semi-liquid.

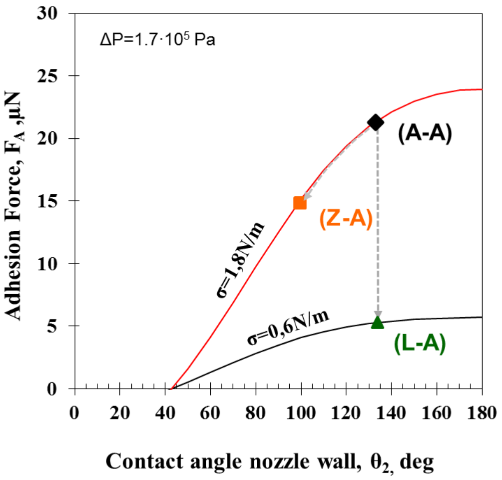

Figure 38. Model calculation for the relation between the adhesion force, the surface tension of molten steel and the contact angle at the nozzle wall.

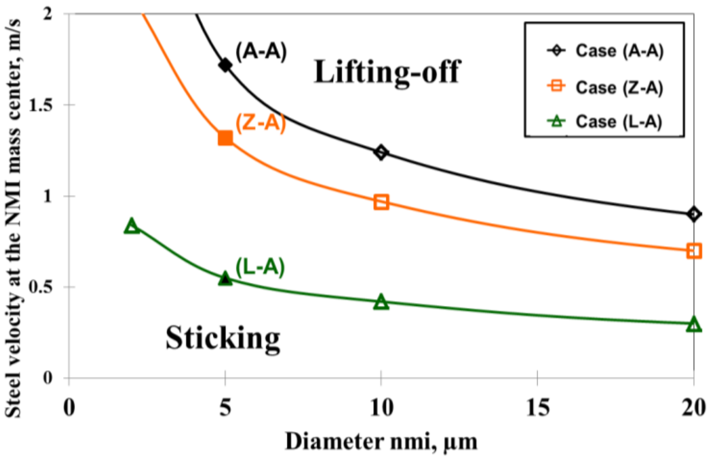

Figure 39. Regime discrimination between sticking/detachment conditions for NMIs in the relative velocity/diameter space for three case studies according to detachment criteria, **Equations. (34), (36)** and **(40)**.

The force balances proposed in the detachment criteria (see **Section 3.1**) have been solved for the three cases presented in **Figure 38.** The properties necessary for the calculations are found in **Table 18**. Since the lift force is small in comparison to the adhesion force the normal ratio given by **Equation (34)** could be neglected. The parallel ratio, given by **Equation (36),** increases with the change of the friction coefficient from 0.3 (in Case (A-A) and (Z-A)) to 0.1 (in Case (L-A)). However, in all calculations, the torque ratio (**Equation (40)**) is the limiting one. As a result, the minimum velocity needed for detaching an inclusion at the inclusion's center of mass is presented in **Figure 39**. The reduction of the adhesion force, from Case (A-A) to Case (L-A), leads to a decrease in the minimal steel velocity at the wall near the particle location for detaching the particle. To remove a 20 μm alumina inclusion in Case (A-A), the minimum steel flow velocity next to the wall would be at least 1 m/s, 0.8 m/s for Case (Z-A) and 0.4 m/s for Case (L-A). As the inclusion size increases, it becomes easier for the force of the steel flow to detach the particle.

In industrial practice, the inclusions found in the clogging deposits are in a range of 1-10 μm. From **Figure 39**, the NMIs in this range may need even higher steel velocities in the near-wall region to be removed, which further underscores the importance of understanding fluid flow in the near-wall region. From the previous calculations, the inclusions within the mentioned range would be completely immersed inside the laminar layer (in accordance with the calculations in **Table 5**), and due to the low velocities in the laminar layer, they will not be detached.

Table 18. Material properties.

Calculated Case	**Cavity fluid**	**Liquid steel**			**Nozzle material**				**Non-metallic inclusion**				
		σ N/m	ρ_S kg/m^3	ν m^2/s	2	θ_2 deg.	E_2 GPa	ν_2	1	θ_1 deg.	E_1 GPa	ν_1	ρ_1 kg/m^3
(1)	Gas	1.8	7000	$7.14 \cdot 10^{-7}$	**Al_2O_3-based**	137	314	0.27	**Al_2O_3**	137	314	0.27	3950
(2)					**ZrO_2-based**	100	175	0.27					
(3)	Liquid FeO	0.6			**Al_2O_3-based**	137	314	0.27					

Another factor to take into account is the roughness of the wall. The roughness may help to introduce some disturbances in the laminar layer and produce a local fluctuating component of the velocity. In turbulent flow, the instantaneous values of velocity fluctuate about a mean value. This fluctuating component in the turbulent near-wall region may be responsible for a temporary increase or decrease of the steel velocity at the particle's position. As this fluctuation could be of the same magnitude as the average mean velocity, it eventually can lead to a possible detachment depending on the inclusion size and the material-related properties such as contact angle and surface tension. The inclusion detachment may be linked to the formation of unsteady turbulent eddies in the near-wall region.

Over the years, it was stated that hydrodynamic conditions strongly influence the deposition of the inclusions[11,22]. The current work gives an insight on how the hydrodynamic conditions may influence the detachment of NMIs from the wall. **Figure 39** illustrates that in areas of low velocity in the near-wall (dead or stagnant zones) the NMIs would not be detached and thus, the clogging tendency would increase. Whereas, turbulent eddies in the near-wall zone may enhance the detachment of NMIs. From the results obtained in **Figure 38** and **Figure 39,** it is apparent that the modification of the refractory wettability proposed above (from Case (A-A) to Case (Z-A)) is not enough to cause a radical decrease of the adhesion forces and therefore to permit the detachment of inclusions from the nozzle wall. The controlled formation of a liquid phase between the inclusion and the nozzle (Case (L-A)) improves detachment in comparison to the initial case, suggesting that modifying the solid inclusions so that they become low melting phases at the refractory/steel interface might reduce clogging.

The high contact angle of 137 deg. between alumina and molten iron is one of the reasons that these inclusions have a high risk of adhesion at the wall and thus, to clog the SEN. Once the inclusions adhere at the nozzle wall by interfacial forces they will not be detached. The solution of the detachment criteria indicates that high velocities at the NMI mass center are needed to detach these inclusions fully immersed in the laminar layer. Furthermore, the small size of the inclusions found in the clogging deposits difficult the NMIs lifting-off.

3.3 Steel-NMI

In **Section 2.1.2.1**, HT-LSCM experiments have been performed with two different steel grades: ULC and Ca-treated steel. In **Table 13**, more details regarding their composition are given. From that investigation is extracted that solid alumina inclusions present a different wettability behavior in each of these steels and thus, a difference in the magnitude of the attractive forces.

In **Figure 28**, the contact angles between alumina and ULC and Ca-treated steel are shown, being 137 deg. and 98 deg., respectively. There is a difference of almost 40 deg. between both contact angles. The adhesion force between an alumina NMI from each steel adhered at a Al_2O_3 based refractory (**Equations (2-7)**) is illustrated in **Figure 40** for different NMIs sizes. In this case, both the contact angle NMI/steel and refractory/steel are equal. The adhesion force increases with the contact angle and with the particle size.

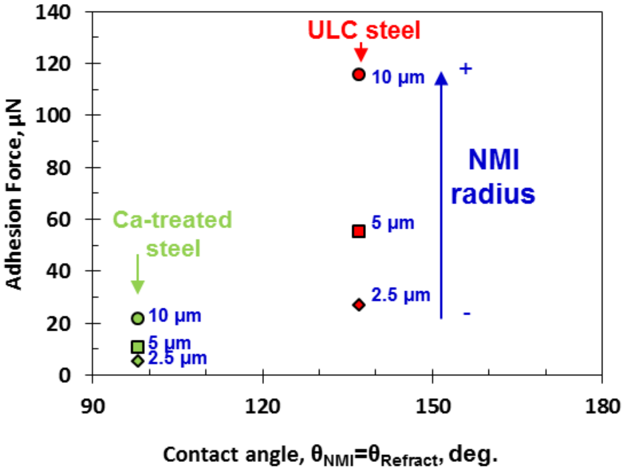

Figure 40. Calculation for the relation between the adhesion force, and the contact angle.

The force balances proposed in the detachment criteria (see **Section 3.1** for more detail) have been solved for the cases presented in **Figure 40.** As previously mentioned the normal ratio given by **Equation (34)** could be neglected. The parallel ratio, R_P, given by **Equation (36),** uses a value of the friction coefficient of 0.3. However, in this case, the torque ratio, R_T, **Equation (40)**, is the limiting one.

The minimum steel velocity at the NMI mass center to detach it from the refractory wall is given in **Figure 41**. The properties necessary for the calculations are found in **Table 19**. The 5 µm alumina inclusions from Ca-treated steel are attached to the Al_2O_3 based refractory w wall with 10 µN**.** This inclusion would need a minimum steel velocity at its mass center of 0.35 m/s to be detached, as shown in **Figure 41.** The velocity rises with the particle size. Now, a 5 µm alumina inclusion from ULC is attached to the wall with 60 µN (see **Figure 40).** It would need approximately a minimum steel velocity at its mass center of 1.2 m/s to be detached. In good agreement with **Figure 39**, the lift off possibility increases with the NMI size.

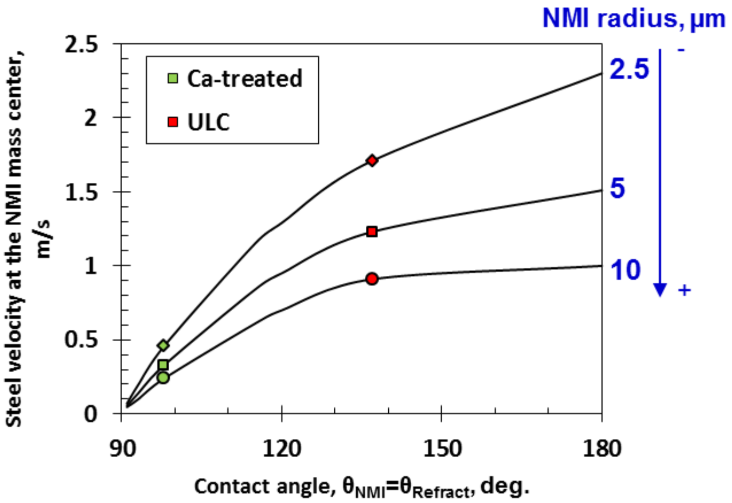

Figure 41. Critical conditions for the detachment of NMIs from different steel grades.

Table 19. Material properties.

Case	**Cavity fluid**	**Liquid steel**			**Nozzle material**						**Non-metallic inclusion**					
		σ N/m	ρ_S kg/m^3	ν m^2/s	2	r_2 µm	θ_2 deg.	E_2 GPa	ν_2	ρ_2 kg/m^3	1	r_1 µm	θ_1 deg.	E_1 GPa	ν_1	ρ_1 kg/m^3
Ca-treated	Gas	1.8	7000	$7.14 \cdot 10^{-7}$	**Al_2O_3**	200	98	314	0.27	3950	**Al_2O_3**	2.5 5 10	98	314	0.27	3950
ULC					**Al_2O_3**	200	137	314	0.27	3950	**Al_2O_3**	2.5 5 10	137	314	0.27	3950

A=Steel A; B= Steel B

When comparing both kinds of steels, it is seen that the alumina inclusion in the Ca-treated steel are easier to lift-off from the steel/refractory interface than the alumina inclusions from the ULC. The reason for this difference is the different wetting behavior of these inclusions with each kind of steel. And thus, the steel grade influences the clogging tendency.

3.4 NMI-steel-refractory

In real practice, two steels with similar composition may behave differently with respect to castability. This may depend on the SEN chosen, as well as on the steel characteristics, such as NMIs type, size and number. The detachment model will be used here as a tool to provide information on the clogging tendency of the steel with certain SEN material, in order to study the mentioned effects.

The investigated system is formed by the following:

(1) Two steels with similar composition that behave differently with respect to clogging, and
(2) Four different SEN materials.

The composition of the steels investigated is summarized in **Table 20**. It is reported from the production site that '**Steel B**' showed higher tendency to clog the SEN during continuous casting than 'Steel A'.

Table 20. Steel A and B compositions (mass-%).

Steel	**C** **%**	**Si** **%**	**Mn** **%**	**Al** **%**	**N** **%**
Steel A	0.07	0.008	0.32	0.01-0.02	0.01-0.02
Steel B	0.07	0.012	0.22	0.01-0.02	<0.01

By means of Scanning Electron Microscopy (SEM), samples of 'Steel A' and 'Steel B' have been investigated. The main inclusion found in these steels after the analysis were solid Al_2O_3 inclusions. The size distribution of the NMIs present in the sample has been obtained and the mean size of the inclusions was calculated and is presented in **Table 21**. 'Steel A' has a typical inclusion size of 1.53 µm ECD and 'Steel B' of 1.37 µm ECD. The alumina inclusions have a similar mean size in both steels. However, the number of NMIs per area is bigger in 'Steel B' than in 'Steel A'. Here, it is assumed that the samples investigated represent the melt conditions.

Table 19. SEM-EDS NMIs statistics.

Steel	**ECD** **µm**	**Number NMIs per Area** **N°/mm^2**
Steel A	1.53	14.42
Steel B	1.37	20.5

As already stated in the previous sections of this work, the interfacial properties of the system NMI-sSteel-refractory are needed to solve the detachment model and to interpret the results. Thus, the materials used were investigated by means of HT-DSA (see **Section 2.1.1.4.1** for more detail) in order to obtain the contact angle between the NMI (θ_1) and the steel and between the refractory and the steel (θ_2). Reactivity between the steel and substrate was not taken into account here.

The contact angle of the Al_2O_3 inclusions and the molten steel are presented in **Table 22**. Al_2O_3-NMIs in 'Steel A' have 104.5 deg. contact angle with steel and in 'Steel B' 102.55 deg.. This is almost 30-40 degrees less that the same inclusion type in a ULC-steel.

Four different SEN materials have been suggested for the SEN: (1) ZrO_2 (called 'Z'), (2) MgO (called 'M'), (3) Alumina (called 'A1'), and (4) Alumina (called 'A2'). The contact angle between 'Steel A' or 'Steel B' and the refractory material are summarized in **Table 22**. Both steels present a non-wettability behavior with the refractories, since the contact angles are higher than 90 deg.. The smaller contact angle is presented for the system 'Steel A/Z' with 111 deg. and the higher contact angle corresponds to 'Steel A/A1' and 'Steel B/A1' with 148 deg..

Table 20. Contact angles between refractory and molten steel.

Steel	$\theta_{Al2O3\text{-}NMI/\ Steel}$ deg.	$\theta_{Z\ /\ Steel}$ deg.	$\theta_{M\ /\ Steel}$ deg.	$\theta_{A1/\ Steel}$ deg.	$\theta_{A2\ /\ Steel}$ deg.
Steel A	104.5	111	132	148	145
Steel B	102.5	131	143	148	145

In **Figure 42**, the adhesion force between a NMI from 'Steel A' and 'Steel B' adhered to different refractories at a melt depth of 1 m and 1.8 N/m of molten steel surface tension is plotted by solving **Equations (2-7)**. The data needed for the calculation are found in **Table 23.** The adhesion force between Al_2O_3-NMI from 'Steel A' and the refractories is listed as follows: A-Z < A-M < A-A2 < A-A1 (from lowest to highest). Regarding 'Steel B', the adhesion force is listed as follows: B-Z < B-M < B-A1 ~ B-A2 (from lowest to highest). It is important to take into account the bigger size of the NMIs from 'Steel A' and the higher contact angle of the NMIs of 'Steel A' in comparison with 'Steel B'. Thus, alumina at M, A1 and A2 interface shows higher adhesion force for 'Steel A' than for 'Steel B'. The exception is found for A-Z, where alumina attraction is weaker than for B-Z. The reason is the different of the contact angles, being 111 deg. for 'Steel A' and 131 deg. for 'Steel B'.

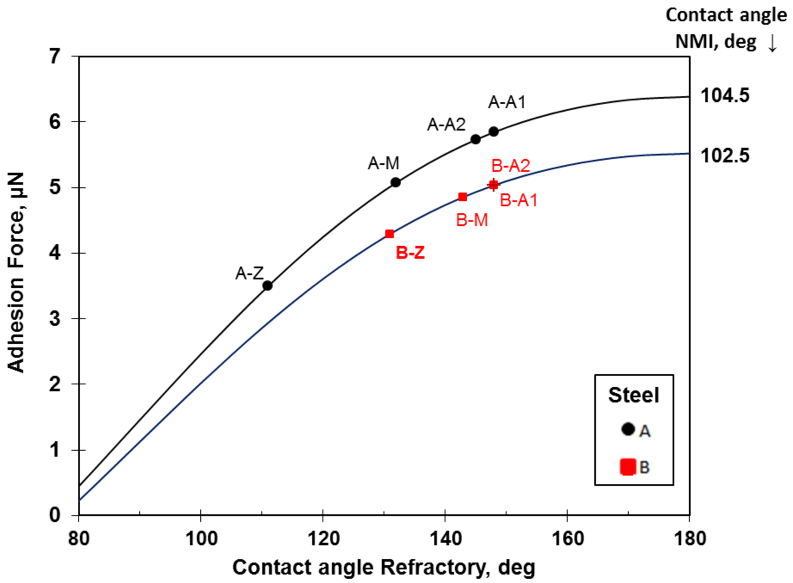

Figure 42. Adhesion force for Al_2O_3 from 'Steel A' and 'Steel B' and different refractory materials.

The force balances proposed in the detachment criteria (see **Section 3.1** for more detail) have been solved for the cases presented in **Figure 42.** As previously mentioned the normal ratio given by **Equation (34)** could be neglected. The parallel ratio, R_P, given by **Equation (36),** uses a value of the friction coefficient of 0.3. However, in this case, the torque ratio, R_T, **Equation (40)**, is the limiting one.

The minimum steel velocity at the NMI mass center to detach it from the SEN wall is given in **Figure 43**. The properties necessary for the calculations are found in **Table 23**. The 1.53 µm alumina inclusions from 'Steel A' are attached to the wall within 3.5-6 µN depending on the refractory**.** The inclusions would need a minimum steel velocity at its mass center of 1.6-2.25 m/s to be detached, as shown in **Figure 41.** As the contact angle of the refractory increased, the harder is to detach the NMIs from the wall and is listed as follows: A-Z < A-M< A-A1 < A-A2. This means that the alumina inclusions from 'Steel A', will be removed easier from Z than from A2 (worse case). The 1.37 µm alumina inclusions from 'Steel B' are attached to the wall within 4-5 µN depending on the refractory (see **Figure 42).** They would need approximately a minimum steel velocity at its mass center of 2.25 m/s to be detached. The detachment velocities behave indifferently since the contact angles are all higher than 130 deg.

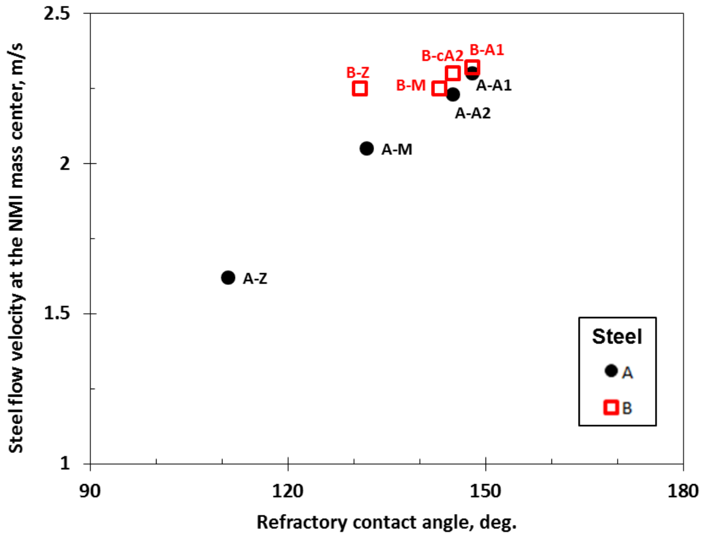

Figure 43. Minimum steel flow velocity at the inclusion mass center needed to detach an inclusion from 'Steel A' and 'Steel B' adhered at different steel/refractory interfaces according to detachment criteria, **Equations. (34), (36)** and **(40)**.

Table 21. Material properties.

Case	**Cavity fluid**	**Liquid steel**			**Nozzle material**						**Non-metallic inclusion**					
		σ N/m	ρ_S kg/m^3	ν m^2/s	2	r_2 µm	θ_2 deg.	E_2 GPa	ν_2	ρ_2 kg/m^3	1	r_1 µm	θ_1 deg.	E_1 GPa	ν_1	ρ_1 kg/m^3
A-Z	Gas	1.8	7000	$7.14 \cdot 10^{-7}$	**Z**	200	111	175	0.27	5680	**Al_2O_3**	1.5	104.5	314	0.27	3950
A-M					**M**		132	300	0.36	3600						
A-A1					**A1**		148	314	0.27	3950						
A-A2					**A2**		145	314	0.27	3950						
B-Z					**Z**	200	131	175	0.27	5680	**Al_2O_3**	1.4	102.6	314	0.27	3950
B-M					**M**		143	300	0.36	3600						
B-A1a					**A1**		148	314	0.27	3950						
B-A2					**A2**		145	314	0.27	3950						

A=Steel A; B= Steel B

When comparing the steel grades, it is appreciated that the inclusions in both steels need a steel velocity at the NMI mass center to be detached higher than 1.4 m/s. As already mention in the previous section, the studied NMIs would be completely immersed inside the laminar layer (in accordance with the calculations in **Table 5**), and due to the low velocities in the laminar layer, they will not be detached. From the previous section was suggested that turbulent eddies in the near-wall zone may enhance the detachment of NMIs.

Furthermore, all the combinations with 'Steel B' and the refractories proposed and 'Steel A' with A1 and A2 refractory exceed the maximum steel velocity of the SEN proposed in **Table 5**. This indicates the low probability of these NMIs to be detached once they adhered to the steel/refractory interface.

The reason for the high steel velocity needed for the detachment is the small size of the NMIs. From **Figure 39** was observed that the smaller inclusions are harder to be lifted off. Thus, the inclusions from 'Steel A' with 1.5 μm mean diameter will need a slightly smaller velocity to be removed from than the inclusions from 'Steel B' with 1.4 μm mean diameter.

These results suggest that 'Steel B' may have a higher tendency to clog the proposed SENs. This agrees with the previous knowledge that 'Steel B' presented a worse castability. Another reason supporting this fact is the higher number of small inclusions present per area in 'Steel B' than in 'Steel A' (see **Table 20**).

In general, it is seen that the alumina inclusions from 'Steel B' are harder to be detached than the ones from 'Steel A'. For three reasons:

(1) The mean NMIs size is smaller for 'Steel B' than 'Steel A'. Small inclusions are harder to be detached than big ones.
(2) The worse wettability of 'Steel B' with the refractory materials. All the contact angles between the refractory and 'Steel B' present a contact angle above 130 deg.
(3) Higher number of NMIs per area in 'Steel B'. A higher number of small inclusions will most presumably also result in a higher number of collisions between the particles and the SEN-wall.

Figure 43 could be used to select the refractory with the lowest clogging risk for each steel. For 'Steel A', the refractory 'Z' may be selected since the velocity needed to detach a NMI adhered from the wall is the smallest one. However, the selection of investigated refractories does not contain a promising option for 'Steel B' as all of them show a high wettability A theoretical measure could be to reduce the number of small inclusions which is in fact difficult to realize in ladle treatment.

3.5 Discussion

The detachment criteria of NMIs at a steel/refractory interface have been developed in this chapter based on the material properties and assuming certain –simplified- fluid flow conditions in the SEN. The interfacial properties of the system NMI-steel-refractory have been investigated in order to investigate how they may affect the clogging tendency. The following is concluded:

(1) **Steel-refractory**: The detachment model has been solved for alumina inclusions at different steel/refractory interface. As a conclusion, it is seen that the improvement of the refractory wettability increases the lift-off tendency of the NMIs from the steel/refractory wall.

(2) **Steel-NMI**: the detachment model has been solved for alumina inclusions coming from two different steel grades (ULC and Ca-treated steels). The alumina is better wetted at the Ca-treated steel and thus they show higher tendency to be lifted-off from the steel/refractory wall than at the ULC.

(3) **NMI-steel-refractory**: Two steels with similar characteristics show different contact angle with the same refractory material.

Other parameters observed to affect the clogging tendency are:

(1) **NMIs Size:** The inclusions within a size of 1-10 µm which are normally present in the clogging deposit need extremely high velocities at its mass center to be detach from the wall once they adhered (see **Figure 39**); Whereas bigger inclusions will be more exposed to the detachment forces.

(2) **NMIs per area:** If the number of NMIs per area is high, more collisions between particles and the SEN-wall will result and the probability for the adhesion of NMIs at the steel/refractory interface will consequently be higher.

(3) **Hydrodynamic conditions:** influence the adhesion and the detachment. Thus, dead-zones with small steel velocity will be areas where no detachment will be possible, whereas turbulent zones may increase the detachment possibility.

4 Argon injection

Argon is injected in the SEN or more commonly at the tip of the stopper rod in order to reduce the adhesion force at the steel/ceramic interface. Some information regarding the argon injection is given in **Section 1.3**. In the next two sections, the following phenomena are examined in detail:

(1) The behavior of bubbles at a steel/refractory interface.
(2) The deposition mechanism of NMI at a steel/gas interface.

In both sections, the forces acting on the bubbles or the NMI are analyzed. Two detachment criteria are developed to investigate the size of bubbles that may be stable at the steel/refractory interface and to investigate if the NMIs may be detached from the bubbles once they adhere at the steel/gas interface.

4.1 Bubbles at steel/refractory interface

In this section, the conditions for the investigation of bubbles at a steel/refractory interface are established. Parameters, such as contact angle or equivalent radius are analyzed with respect to their influence on their behavior at the steel/refractory interface. The forces acting to adhere or detach the bubble at the wall are explained.

In water model experiments, Bai and Thomas et al.[88,89] observed that at large Ar injection rates and high water flow, the argon bubbles elongate along the wall forming a gas layer, preventing the physical contact between the steel stream and the refractory wall and thus, the build-up of inclusions on the SEN wall. In these experiments, argon gas was injected horizontally through the tiny holes on the inner wall of the nozzle into highly turbulent downward-flowing liquid. Bubble formation fell into one of the four different modes represented in **Figure 44**. They concluded that the mode depends primarily on the velocity of the flowing liquid and secondarily on the gas flow rate.

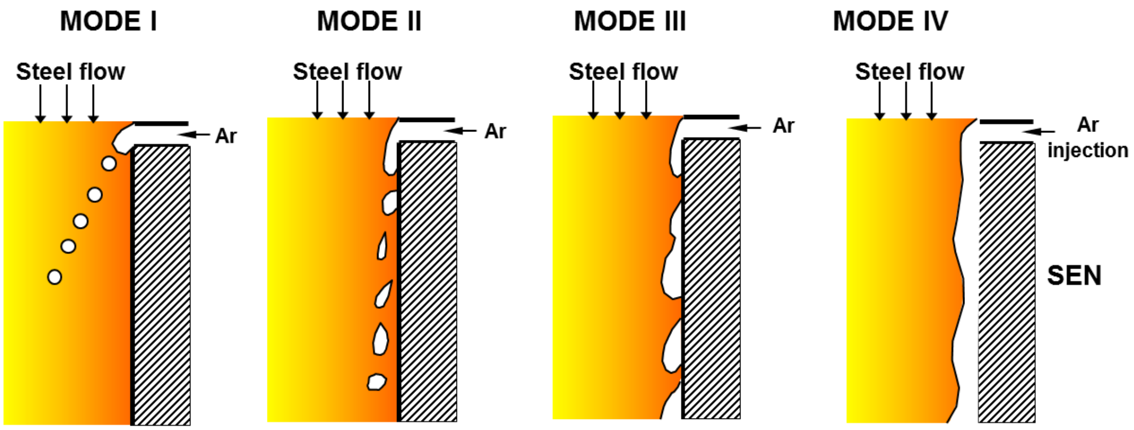

Figure 44. The four modes of injected gas behavior through Water-modelling experiments[88,89]

(1) **Mode I** (low liquid speed and small gas flow rate), uniform-sized bubbles form and detach from the wall.
(2) **Mode II** is intermediate between Mode I and Mode III.
(3) **Mode III** (high liquid speed), the injected gas elongates down-along the wall and breaks into uneven sized bubbles.
(4) **Mode IV** (high liquid speed and high gas flow rate), the gas elongates a long distance down the nozzle walls, forming a sheet before breaking up.

Bai et al.[89] claimed that in a real-life nozzles with hundreds of pierced holes or thousands of tiny pores on porous refractory, a continuous gas curtain might be expected on the gas injection section of the inner wall of the nozzle for **Mode III**. In fact, the argon gas injected into the liquid steel has much bigger tendency to fall into **Mode III** and to form a gas curtain/layer on the refractory wall due to the much larger surface tension of the liquid steel and the non-wetting behavior of the liquid steel on the refractory material. Their experiments also showed that no matter what bubble formation mode, the injected gas will partially and from time to time also detach from the wall, break up into discrete bubbles and join the liquid stream. Therefore, no stable and permanent gas curtain in the tundish nozzle might form but a partial occupancy of the interface with continuously adhering and after a while detaching bubbles, at least after a certain distance from the gas injection section.

If the argon injected follows **Mode III** as explained by Bai et al. [89], the bubbles attached to the wall will experience the effect of the drag force due to the shearing liquid flow. The transverse flowing liquid makes the contact angles no longer uniform along the bubble-solid contact circumference[89]. At the upstream of the bubble, the contact angle increases to θ_a, defined as the advancing contact angle, and at the downstream of the bubble, the contact angle decreases to θ_r, defined as the receding contact angle shown in the following **Figure 45-a)**.

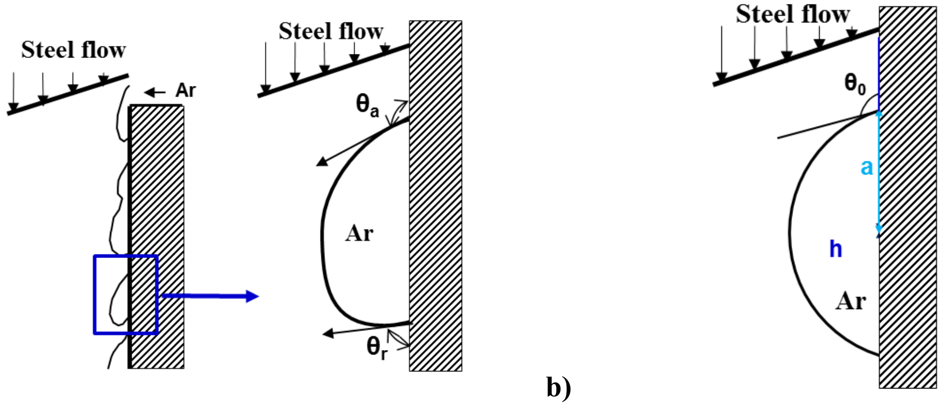

a) b)

Figure 45. a) Bubbles attached to the wall following **Mode III**. The advance and receding contact angles due to the drag force acting over the bubble and **b)** static bubble attached at the nozzle wall defined by a static contact angle and the height of the cup, h, and the contact radius, a.

Estimations on advancing and receding contact angles for elongated argon bubbles in flowing steel can be made based on the observation in the air-water system. The static contact angle is much larger for steel-argon system (θ_O =150 deg.) than for water-air system (θ_O =50 deg.). The advancing contact angle, θ_a, should be larger than the static contact angle θ_O and increases with increasing liquid velocity, but it cannot be larger than 180 deg.. The receding contact angle θ_r should be smaller than the static contact angle and decreases with increasing liquid velocity. Bai et al.[89] defined a contact angle function based on the liquid steel velocity from their estimations the advancing and receding contact angles for a steel velocity of 0,9 m/s are θ_a =155 deg. (> θ_O =150 deg.) and θ_r =124 deg. (> θ_O =150 deg.) when θ_O = 150 deg., respectively[89].

For the following forces calculations, the bubble will be considered to be static at the nozzle wall with a contact angle of θ_O = 150 deg.. The height of the bubble, defined as h, and the contact radius between the bubble and the wall, defined as a, are calculated with **Equation (42)** and **(43)**. More details about the bubble parameters calculation (h and a) are given in **Figure 45-b)** and **Appendix F**.

$$a = r_b \sin \theta_0 = \frac{h}{\tan\left(\frac{\pi - \theta_0}{2}\right)} \tag{41}$$

$$h = a \cdot \tan\left(\frac{\pi - \theta_0}{2}\right) = \frac{2r_b\left(\tan\left(\frac{\pi - \theta_0}{2}\right)\right)^2}{\left[1 + \left(\tan\left(\frac{\pi - \theta_0}{2}\right)\right)^2\right]} \tag{42}$$

Being r_b the equivalent bubble diameter.

Table 17. SEN characteristics and maximum bubble size inside the boundary layer.

Φ_{SEN} mm	u_{max} m/s	Re	δ=h µm	$r_{b,max}$ mm
30	1	21.000	~370	2.8
	2	42.000	~260	1.9

If the height of the bubble is equal to the thickness of the boundary layer the maximum possible radius of a bubble inside the boundary layer will arise. From **Table 17**, the thickness of the boundary layer, δ, for a 30 mm diameter SEN was given, being of approx. 370 µm for 1 m/s maximum steel velocity and of approx. 260 µm for 2 m/s maximum steel velocity. When substituting the thickness of the boundary layer into **Equation (42)** the maximum possible equivalent bubble radius, $r_{b,max}$, results with 2.8 mm and 1.9 mm for 1 and 2 m/s of molten steel, respectively. Bubbles bigger than this size will no longer be inside the laminar layer.

In this section, the argon injected is assumed to fall into **Model III** of **Figure 42**, where the gas elongates down-along the wall. The bubble is assumed to be static at the steel/refractory interface with a contact angle of 150 deg.. As well the geometrical parameters of the bubble (a and h) have been defined in function of the equivalent bubble radius. The maximum size of a bubble that may be immersed on the boundary layer of the SEN has been calculated.

4.1.1 Adhesion of bubbles at a steel/refractory interface

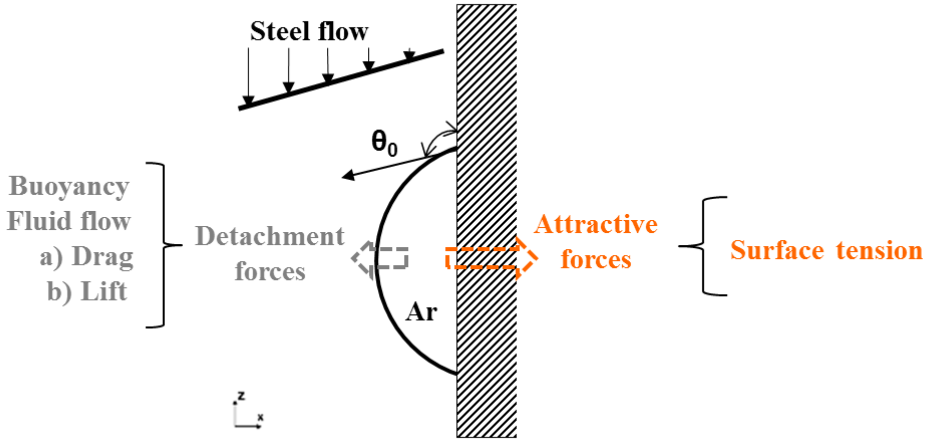

Figure 46. Attractive and detachment forces affecting a bubble adhered at a steel/refractory interface.

The argon bubbles at the steel/refractory interface may be subjected to attractive forces, which keep the bubble at the wall, and to other external forces which force the bubble to be detached, as shown in **Figure 46**. The attractive force, that is investigated here, is the surface tension force. The detachment forces analyzed are related to the bubble material properties and to the steel fluid flow, such as buoyancy, drag and lift forces.

4.1.1.1 Attractive force

(1) **Surface tension force**

The force that keeps a bubble adhered at the surface of a nozzle wall is called surface tension force, F_S, and it is illustrated in **Figure 47-a)**. The derivation of the surface tension force for a static bubble ($\theta_r = \theta_a = \theta_0$) adhered to a SEN-wall is demonstrated in detail in **Appendix G**, and finally results in **Equation (44)** [89,263]

$$F_S = \pi\, a\, \sigma \sin\theta_0 \tag{43}$$

In **Figure 45-b),** the dependence of the bubble size on the adhesion force is plotted. The surface tension force that keeps the bubbles attracted to the wall increased with the bubble size.

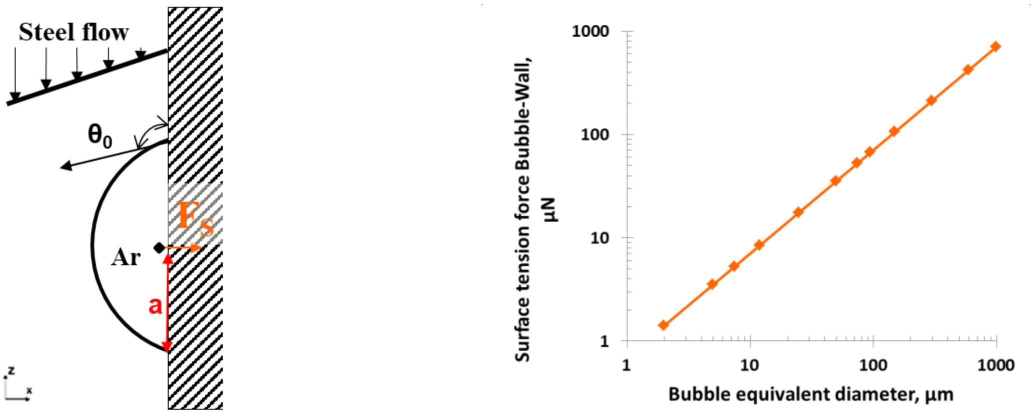

a) **b)**

Figure 47. a) Surface tension force in a static bubble at the nozzle wall, and **b)** Dependence of the surface tension force (Bubble-wall) with the argon bubble size.

4.1.1.2 Detachment forces

Bubbles adhered at a nozzle wall will be subjected to other forces in the near-wall region as illustrated in **Figure 48**. Buoyancy, drag and lift will be analyzed.

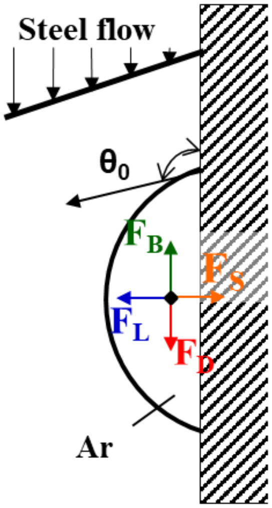

Figure 48. Force contributions in a bubble adhered at a nozzle wall in the boundary layer. (F_S = surface tension force, F_B = buoyancy force, F_L= lift force, and F_D = drag force).

(1) **Buoyancy force**

Each argon bubble submerged in molten steel experiences an upward force opposing its weight, known as buoyancy force, F_B. The buoyancy force depends on the density difference between the bubble and the steel, the gravity acceleration, and the volume of the submerged bubble, and is given by the following equations:

$$F_B = V_b(\rho_s - \rho_b)g \tag{44}$$

$$V_b = \frac{1}{3}\pi r_b^3 \cdot \frac{[2+\cos(\pi-\theta_o)]\sin(\pi-\theta_o)}{[1+\cos(\pi-\theta_o)]^2} \tag{45}$$

where V_b is the volume of the argon droplet[264] (m^3), ρ_s and ρ_b are the density (kg/m^3) of the molten steel and the gas bubble, respectively, and g is the gravity acceleration (m/s^2).

(2) **Fluid flow forces**

The fluid flow conditions have been stablished previously in **Section 1.2.2**.

a) **Drag force**

A bubble adhered to the nozzle experiences a drag force due to the relative movement of molten steel. The drag force, F_D, depends on the bubble surface and on the molten steel properties, such as velocity and density according to **Equation (46)**[89]:

$$F_D = C_{D,NS} \frac{\rho_S u_r^2}{2} A_1 \tag{46}$$

where $C_{D,NS}$ is the drag coefficient for a non-spherical shape, A_1 is the projected area of the bubble toward the flow direction (m^2), ρ_S is the molten steel density (kg/m^3) and u_r is the relative velocity between the inclusion and the molten steel at the inclusion's mass center (m/s).

The shape of the bubble will be approximated to an ellipsoid with an aspect ratio defined in **Equation (47)**:

$$E = \frac{d_\parallel}{d_\perp} = \begin{Bmatrix} < 1 & \rightarrow & \text{Oblate} \\ = 1 & \rightarrow & \text{Sphere} \\ > 1 & \rightarrow & \text{Prolate} \end{Bmatrix} \tag{47}$$

$$d_\parallel = 2 \cdot a \tag{48}$$

$$d_\perp = 2 \cdot h \tag{49}$$

Where $d_\parallel$ and $d_\perp$ are the parallel and normal diameters. In this case, $d_\parallel > d_\perp$ and thus $E > 1$ in **Equation (48)**. The bubble will be approximated to a prolate spheroid.

The drag coefficient for non-spherical particles, $C_{D,NS}$ at intermediate Reynolds numbers is calculated as follows[265]:

$$C_{D,NS} = C_D^* \cdot C_{Shape} \tag{50}$$

$$C_D^* = \frac{24}{Re_p^*}\left[1 + 0.15\left(Re_p^*\right)^{0.687}\right] + \frac{0.42}{1 + \frac{42{,}500}{\left(Re_p^*\right)^{1.16}}} \quad \text{for circular cross section} \tag{51}$$

$$Re_p^* = \frac{C_{Shape} Re_p}{f_{shape}} \tag{52}$$

Where C_D* the dimensionless Clift-Gauvin expression for the drag coefficient for shapes with circular cross section, f_{shape} is the Stokes correction factor for prolate spheroids, Re_p* is the corrected Reynolds number, and C_{shape} is the Newton correction factor.

The Stokes correction factor is defined as the ratio of creeping solid spheroid drag force to creeping solid sphere drag force (where both have the same equivalent diameter). The Stokes correction factor for prolate spheroids, f_{Shape}:

$$f_{shape} = \frac{F_{D,NS}(E, Re_p \to 0)}{F_{D,Sphere}} = \left(\frac{2}{5} + \frac{2E}{5}\right) \cdot E^{-\frac{1}{3}} \quad \forall \quad 1 < E < 6 \tag{53}$$

The Newton correction factor represents the normalization the drag coefficient with the drag coefficient of a sphere with the same volume. The Newton drag correction, C_{shape}:

$$C_{Shape} \approx 1 + 0.7\sqrt{A^*_{surf} - 1} + 2.4(A^*_{surf} - 1) \text{ for } E > 1 \tag{54}$$

$$A^*_{surf} = \frac{1}{2E^{\frac{2}{3}}} + \frac{E^{\frac{1}{3}}}{2\sqrt{1 - E^{-2}}} \sin^{-1}\left(\sqrt{1 - E^{-2}}\right) \text{ for } E \geq 1 \tag{55}$$

Where A^*_{surf} is the surface area ratio for a prolate spheroid given by **Equation (55).**

The projected area towards the fluid flow is equivalent to half of the prolate spheroid:

$$A_1 = (\pi h^2)/2 \tag{56}$$

with h the height of the cup.

Due to the small particle sizes involved, the particle Reynolds number, Re_p, will be quite small. Thus, the non-stationary drag force terms, such as virtual mass force and Basset force may be neglected.

b) **Lift force**

In addition to the drag force, the flow passing around the adhered bubble may create a difference in pressure resulting in a lifting force normal to the wall[67,68]. The approach of Leighton and Acrivos[69,70] will be used according to **Equation (58)**,

$$F_L = 9{,}22 \mathrm{Re}_G (\dot{u} \mu r_b^2) \quad \forall \quad \mathrm{Re}_G = \frac{\dot{u} r_b^2}{\upsilon} \tag{57}$$

where Re_G is the shear Reynolds number, and r_b the equivalente bubble radius.

In this section, the **Mode III** represented in **Figure 44**, has been assumed to be the typical behavior of gas injected in the flow control system of the mould. Parameters, such as bubbles size and contact angle with were studied and the bubble was assumed to be static and stable at the interface for the following analyses. The forces acting on a bubble adhered at the steel/refractory interface have been explained. The surface tension force keeps the bubble adhered to the interface, but buoyancy, drag and lift act against this adhesion. In the following section, the deposition mechanism of NMIs towards a steel/gas interface will be investigated.

4.2 Inclusion at the steel/gas interface

The NMIs deposition mechanism at a steel/gas interface is divided in three steps[266,267] and is schematically illustrated in **Figure 49**.

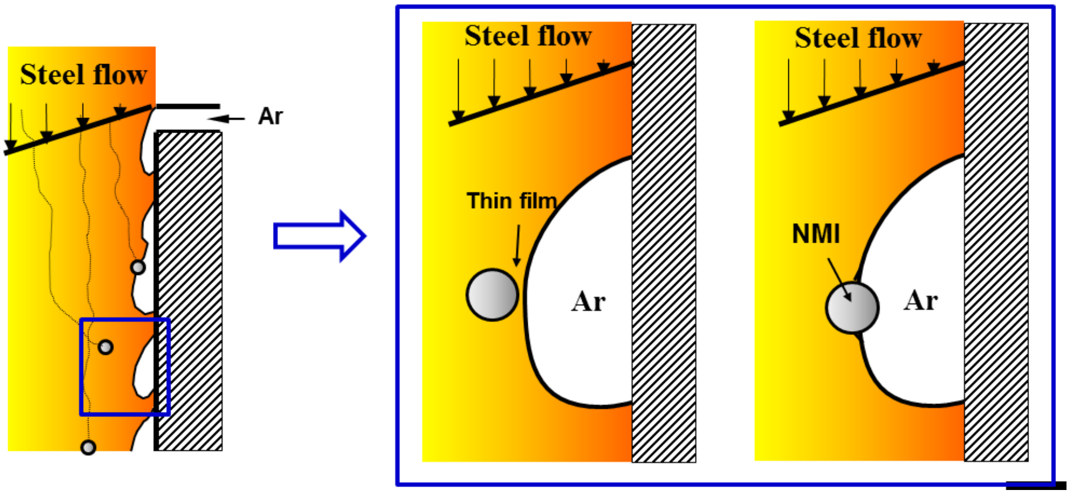

Figure 49. Mechanism of deposition of NMI at an argon bubble: Transport, separation and adhesion.

(1) **Transport:** The NMIs are transported from the bulk region to the gaseous/liquid interface upon formation of a thin film of molten steel between the NMI and the gas phase.

(2) **Separation:** The liquid film between the NMI and the gas phase will drain to a critical thickness at which rupture occurs.

(3) **Adhesion:** Movement of the three-phase contact line until a stable wetting perimeter is established.

The separation and adhesion steps will be developed in the following sections, but no further comment on the transport step will be given here.

4.2.1 Separation of NMIs at a steel/gas interface

When a NMI separates from the metal bath to the steel/gas interface by the rupute of the thin steel film there is a change in the interfacial energy of the NMI. The NMIs passes from a the bulk melt to a steel/gas interface. The free energy change in the system is given by **Equation (62)**[54]. More details on how to obtain this equation are given in **Appendix (A)**.

$$\Delta G = \sigma \cdot (\cos \theta_1 - 1) \qquad (58)$$

Where θ_1 is the NMI contact angle with the molten steel.

Figure 50 indicates that an Al_2O_3 should be attached more readily towards a steel/argon gas interface than towards a steel/refractory interface. This indicates that there is a high tendency for NMIs to separate towards a gas bubble adhered at the nozzle wall.

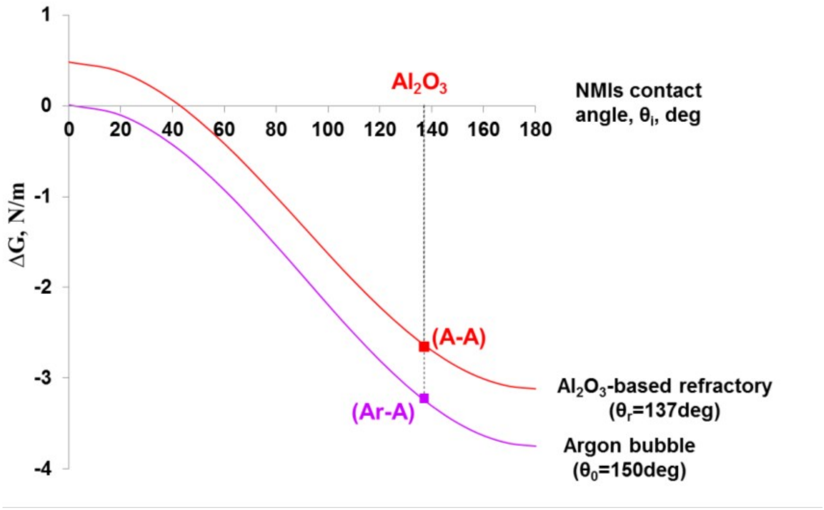

Figure 50. Free energy change, ΔG, when different Al_2O_3 NMIs separate at an Al_2O_3-based refractory (Point (A-A)) and an argon bubble (Point (A-Ar)) given by **Equation (58)**.

4.2.2 Adhesion of NMIs at a steel/gas interface

The NMIs adhered at the steel/gas interface may be subjected to attractive forces, which keep the NMIs at the gas bubble, and to other external forces which force the NMIs to be detached, as shown in **Figure 51**. The attractive force investigated here will be the capillary force and the detachment forces analyzed are buoyancy, drag and lift forces.

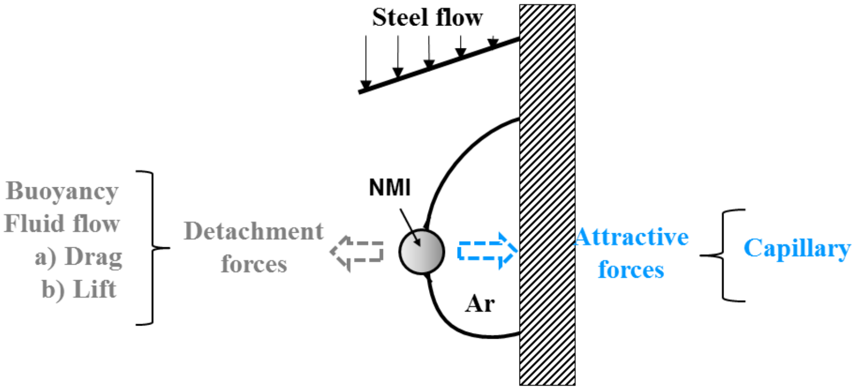

Figure 51. Attractive and detachment forces affecting a bubble adhered at a steel/refractory interface.

4.2.2.1 Attraction force

(1) **Capillary force**

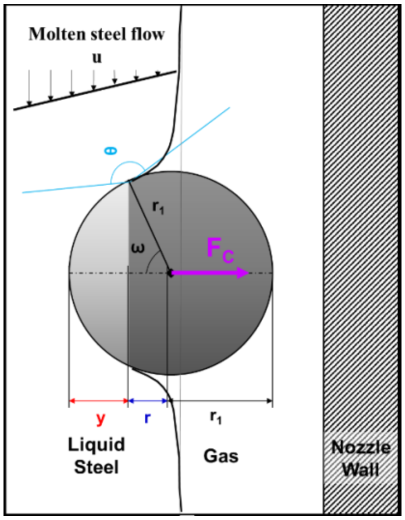

Figure 52. NMI adhered at an argon bubble at the nozzle wall.

The micro-inclusions stay adhered at the molten steel/gas interface due an attractive force called capillary force, F_C[266,267]. This force is defined by **Equation (59)** and illustrated in **Figure 52**.

$$F_C = -2\pi r_1 \sigma \sin\omega \sin(\omega + \theta_1) \tag{59}$$

$$\omega = \operatorname{atan}\left[\frac{-\sigma\sin\theta_1}{\left[\frac{r_1}{r_b}\sigma - r_1 r_b \rho_S g + \sigma\cos\theta_1\right]}\right] \tag{60}$$

where r_1 is the NMI radius, σ is the surface tension, ω is the center-angle when the particle is stable at the fluid interface. This force defined in **Equation (59)** is calculated at the stability position, which is indicated by the angle "ω", given in **Equation (60)**. More details on how to obtain "ω" are found in **Appendix H**.

In **Figure 53**, the capillary force suffered by an Al_2O_3-NMI adhered at a steel/argon interface is calculated from **Equation (59)** and **(60)**. The capillary force decreases with the increase of the bubble size as can be seen in **Figure 53**. For a 10 µm Al_2O_3-NMI the capillary force decreases from 2.9 – 0.6 µN when the equivalent bubble radius is increased from 200 – 750 µm.

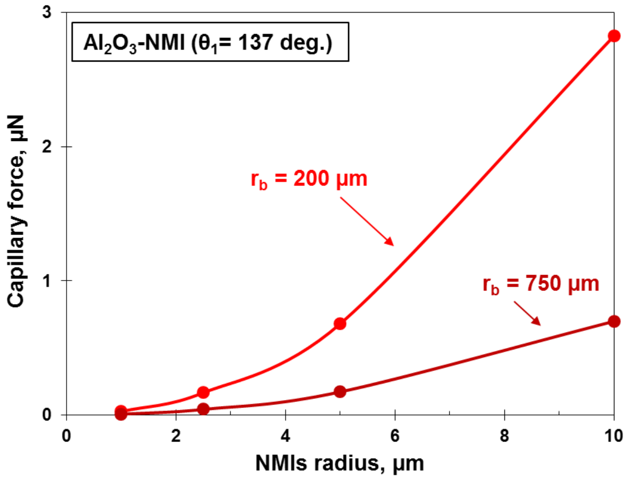

Figure 53. Capillary force between NMI and an argon bubble a) for Al_2O_3 NMIs at different bubbles sizes.

Another parameter affecting the capillary force is the NMI wettability. The change of the capillary force when the wettability of the NMI is improved from 137 deg. (Al_2O_3-NMI) to 100 deg. (ZrO_2-NMI) is shown in **Figure 54-a)**. ZrO_2, which is better wetted by the steel, will adhere strongly to the steel/argon interface than alumina of the same size.

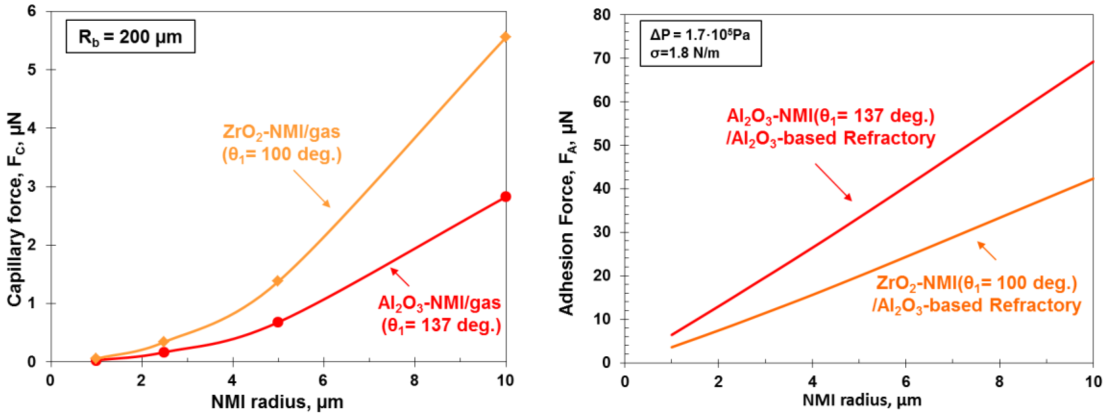

a) **b)**

Figure 54. Capillary force between NMI and an argon bubble **a)** for different NMI types at constant bubble size, and **b)** Adhesion force for Al_2O_3 NMI and ZrO_2 NMI.

This effect is the opposite to that observed in **Figure 54-b)** where the adhesion force of a NMI adhered at a steel/refractory interface is illustrated (**Equations (2)-(7)**). In **Figure 54-b)**, the adhesion force decreases with the decrease of the contact angle. When comparing a ZrO_2 and an Al_2O_3 inclusion, it is seen that the ZrO_2 will be attracted with a weaker force at the steel/refractory interface than Al_2O_3 but it will be attracted stronger than Al_2O_3 at the steel/gas interface.

4.2.2.2 Detachment forces

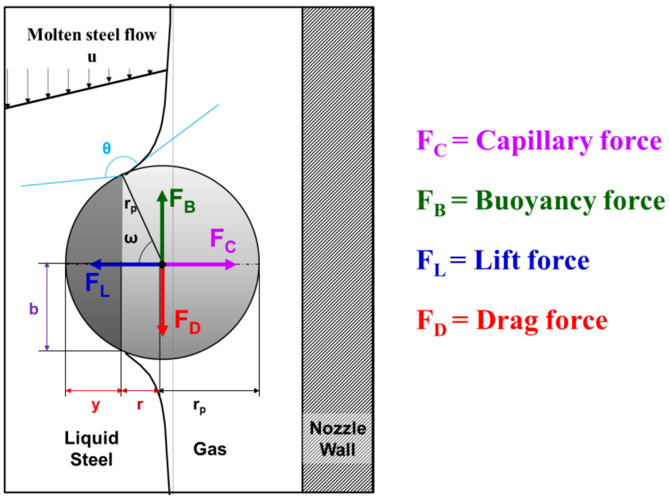

Figure 55. Forces analyzed on a NMI in contact with an argon bubble in the boundary layer. (F_C = Capillary force, F_B = buoyancy force, F_L= lift force, and F_D = drag force)

Capillary forces attach the NMIs towards the steel/argon interface. The particles partially immerse in the steel and in the argon bubble; the immersion depends on the center-angle ω. Different forces act to detach the inclusions from this interface. Drag and lift come from the fluid flow created from the steel movement into the SEN, thus they only act in the dark-shadow area of **Figure 55**; whereas, buoyancy force depends on the material properties.

(1) Buoyancy force

As already mentioned, micro-oxides partly immerse in the steel and in the argon bubble. The buoyancy force of this partially immersed NMI is the sum of the buoyancy of the part immersed in the steel and the part immersed in the argon bubble, this relation is given in **Equation (61)**. However, since the buoyancy of the particle in the gas is too small. The buoyancy can be approximated to that created for the volume of the particle immersed in the steel.

$$F_B = F_{B,immersedinGas} + F_{B,immersedinSteel} = F_{B,immersedinSteel} \tag{61}$$

The buoyancy is given by the product of the density of the liquid, acceleration due to gravity, and the volume of liquid displaced by the submerged section of the particle, that is[266,268,269]:

$$F_B = \frac{\pi}{3} r_p^3 [\cos\omega^3 - 3\cos\omega + 2] \cdot (\rho_S - \rho_1) g \tag{62}$$

Where ρ_1 is the density of the particle.

(2) Fluid flow force

a) Drag force

A spherical inclusion adhered to an argon bubble in the bulk melt experiences a drag force due to the relative movement of molten steel. The drag force, F_D, depends on the inclusion surface and on the molten steel properties, such as velocity and density according to **Equation (63)**[7,43,47]

$$F_D = C_D \frac{\rho u_r^2}{2} A_1 \tag{63}$$

where C_D is the drag coefficient, A_1 is the projected area of the inclusion toward the flow direction (m^2) and u_r is the relative velocity between the inclusion and the molten steel at the inclusion's mass center (m/s).

The drag coefficient on a sphere in steady motion can be estimated by using the empirical correlation proposed by Lapple, given in **Equation (64)**[43,47,66]. This equation is an interpolation between the Stokes and the Newton regimes.

$$C_D = \frac{24 \cdot \left(1 + 0{,}15 \cdot Re_p^{2/3}\right)}{Re_p} \quad \forall \quad Re_p = \frac{u_r\, d_1}{\upsilon} \leq 1000 \tag{64}$$

The projected area of the inclusion toward the flow direction, A_1, is given by **Equation (65).**

$$A_1 = \left(\frac{1}{2}\right) \cdot \pi y^2 \tag{65}$$

$$\mathbf{y} = r_p - r = r_p - \left(r_p \cdot \cos w\right) = r_p \cdot (1 - \cos w) \quad \forall \quad w < 90 \tag{66}$$

where y is the distance of the particle that is immersed into the steel.

Due to the small particle sizes involved, the particle Reynolds number, Re_p, will be quite small. Thus, the non-stationary drag force terms, such as virtual mass force and Basset force, are not important and therefore will not be considered.

b) **Lift force**

The lift force for a NMI was already defined by **Equation (18)** in **Section 1.1.2.2**. Here the lift force of a NMI adhered at a steel/gas interface will be approximated to the NMI adhered at a steel/refractory interface.

In this section, the deposition mechanims of a NMI towards a steel/gas interface was introduced. The attractive and detachment forces that act over the adhered NMI adhered at have been explained. The capillary force keeps the bubble adhered to the interface, but buoyancy, drag and lift act against its adhesion.

4.3 Detachment criteria

Two detachment criteria will be developed here:

(1) For a bubble adhered to a steel/refractory interface
(2) For a NMI adhered to a steel/gas interface.

The criteria are based on the force contributions already introduced in **Section 4.1.1** and **4.2.2**. See **Figure 46** and **53** for more detail. Three criteria in terms of force and torque balances will determine whether a bubble in contact with the wall or a NMI at the steel/gas interface will be detached from the interface or not. The same balances as in **Section 3.1** will be solved for each case. The final Equations are presented in **Table 23**.

Table 22. Detachment criteria for a gas bubble at a steel/refractory interface and a NMI at a steel/gas interface.

	Gas bubble at Steel/Refractory interface	**NMI at Steel/gas interface**
Normal movement	$R_N = \frac{F_L}{F_S}$ **(67)**	$R_N = \frac{F_L}{F_C}$ **(68)**
Parallel movement	$R_P = \frac{(F_D - F_B)}{\kappa_S (F_S - F_L)}$ **(69)**	$R_P = \frac{(F_D - F_B)}{\kappa_S (F_C - F_L)}$ **(70)**
Toque moment	$R_T = \frac{hF_D + aF_L - hF_B}{aF_S}$ **(71)**	$R_T = \frac{yF_D + bF_L - r_1 F_B}{r_b \sin \omega \, F_C}$ **(72)**

For the detachment of a bubble from the wall or a NMI from the bubble in the normal direction (**Equations (67)** and **(68)**), the lift force must overcome the attractive force. Since the lift force is directly dependent on the fluid flow conditions next to the wall, any increase in velocity at the near-wall region will increase the normal ratio. The resultant tangential force should overcome the friction between the surfaces, to move the bubble or the NMI in parallel direction (**Equations (69)** and **(70)**). The frictional force, F_F, is proportional to the normal force exerted by each surface on the other, directed perpendicular to the surface. Where F_n is the normal force (N), κ_s is the coefficient of friction defined as 0.1 for both cases. The torque moment (**Equation (71)** and **(72)**) defines the tendency of a force to rotate an object about an axis[256]. Drag and lift forces exerted on the bubble or in a NMI might induce a torque. The criterion indicates that the bubble or the NMI will be detached when one of the ratios (R_N, R_P or R_T) is greater than unity.

4.3.1 Results

First, the stability of argon-gas bubbles next to the wall will be studied by implementation of the detachment criteria, given by **Equations (67)**, **(69)**, and **(71)**. As a result, the smallest bubble that will be detached at certain steel velocity at its mass center is obtained. It is seen that an equivalent bubble with a radius of 810 μm will be detached when the velocity of the steel is at its mass center is 2 m/s by the parallel ratio. This size will be taken as the maximum bubble size that will be stable at the wall. It can be seen in **Table 17** that bubbles smaller than 1.9 mm lay inside the boundary layer when the maximum steel velocity is 2 m/s in a 30 mm SEN. Therefore, it can be assumed that the argon gas bubbles smaller than 810 μm may be inside the boundary layer and in addition, being stable at the interface. Even though, it is known that at certain point the bubbles tend to break out, this is not taken into account here.

The detachment criteria for a NMI adhered at a molten steel/gas interface will be implemented for NMIs that do not contact with the wall. This means that the immersion radius of the NMI in the bubble (r_1+r) smaller than the height of the bubble, h. The minimum size of the bubble for a NMI adhesion without touching the nozzle depends on the NMI size. In **Table 18**, the minimum and maximum bubble size for each NMI size is given and it was presented in **Figure 53-b)**.

Table 18. Minimum and maximum equivalent bubble size at the nozzle wall for Al_2O_3 NMIs.

r_1 μm	$r_{b,min}$ μm	$r_{b,max}$ μm
1	13	810
2.5	32	
5	63.5	
10	127.5	

The detachment criteria, given by **Equations (68)**, **(70)**, and **(72)**, will be implemented to study the detachment of NMIs adhered at a steel/argon interface. As a result, the minimum velocity needed for detaching an inclusion at the inclusion's center of mass by any of the force ratios is presented in **Figure 56**.

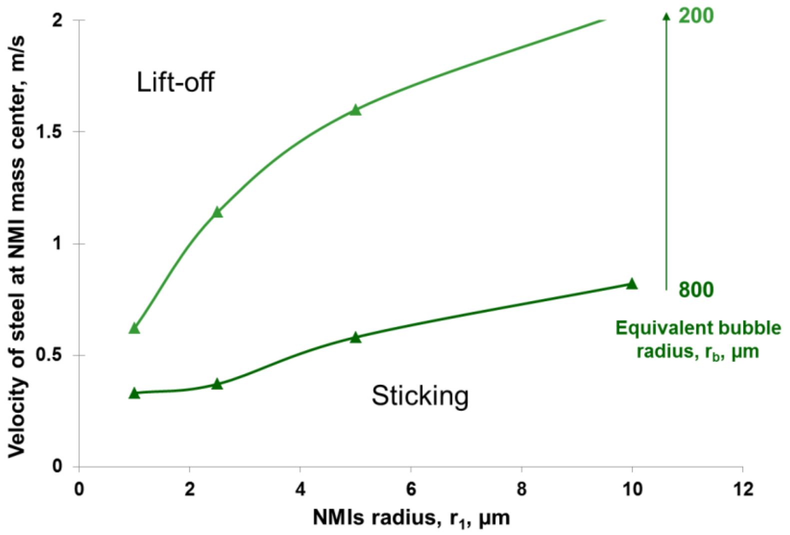

Figure 56. Regime discrimination between sticking/detachment conditions for NMIs in the relative velocity/diameter space for an alumina inclusion at a steel/argon interface for different bubble sizes according to detachment criteria given by **Equations (68)**, **(70)** and **(72)**.

The parallel ratio, given by **Equation (70),** uses a value of the friction coefficient of 0.1 and it is the limiting ratio for all cases. A 5 µm diameter inclusion attached to the steel/gas interface needs a minimum steel velocity at its mass center of 0.55 m/s to be detached from an 800 µm radius bubble and would need 1.65 m/s for a 200 µm bubble**.** From **Figure 56**, it can be seen that the decrease of the bubble size raises the steel velocity at the NMI mass center to detach it, since the capillary force rise with the decrease of the bubble volume**.** Furthermore, if the inclusion size increases from 1 to 10 µm, it becomes harder to detach the particle. As well, the capillary force rises with the particle size at a constant volume of the bubble. Both effects, the NMI size and the bubble volume, are in good agreement with **Figure 53** and **54-a)**.

The inclusions within the mention range, once separate and adhere at the steel/argon interface are not prone to be detached, since they are inside the boundary layer and the velocities in this area are low, in the range presented in **Table 5**. Thus, the argon bubbles attached to the SEN wall could act successfully as NMI collectors and protectors in order to avoid the direct contact and posterior sintering of the NMI to the wall.

In this section, the detachment criteria for and the lift-off a bubble from the steel/refractory interface and the lift-off NMI at a steel/gas interface have been derivated. The first model gives information regarding the maximum size of stable argon bubbles at the steel/refractory interface. The latter criteria give information regarding the critical conditions for the detachment of NMI for the interface based on the bubble volume.

4.4 Discussion

In the following section, parameters influencing the mechanism of deposition of NMIs at a steel/gas interface are discussed. Moreover, the comparison with the deposition of NMIs at a steel/refractory interface is performed. The following parameters are commented:

(1) Change of free energy for the separation of NMIs to an interface,
(2) Influence of the volume of the fluid phase of the adhesion step, and

A NMI separates from the metal bath to an interface in order to reduce its high interfacial energy. In this work, the free energy change for the adhesion of a NMI has been investigated for two different interfaces:

(1) Steel/refractory interface by **Equation (1)**.
(2) Steel/gas interface by **Equation (62)**.

While the tendency for separation at the steel/refractory interface can be reduced by improving the wettability of the solid phases (NMI or refractory). As it can be seen in **Figure 57**, from an initial situation of adhesion of an alumina inclusion at an alumina-based refractory in Point (A-A), the clogging tendency will be reduced:

(1) by the selection of refractories with better wettability with steel like in Point (Z-A) in **Figure 57.**
(2) by selection of refractories with certain reactivity like in Point (L-A) in **Figure 57.**
(3) by the modification of solid alumina inclusion in liquid inclusions by calcium treatment in Point (A-CA) in **Figure 57.**

However, the steel/gas interface behaves differently. The NMIs will separate more readily to an argon bubble (Point Ar-A in **Figure 57**) than to an alumina refractory wall (Point A-A in **Figure 57**). Thus, the argon purging has a double task:

(1) Protect the refractory wall, avoiding the direct contact of the NMIs with the wall
(2) Collect NMIs, avoiding them to pass on to the next processing stage, the casting process.

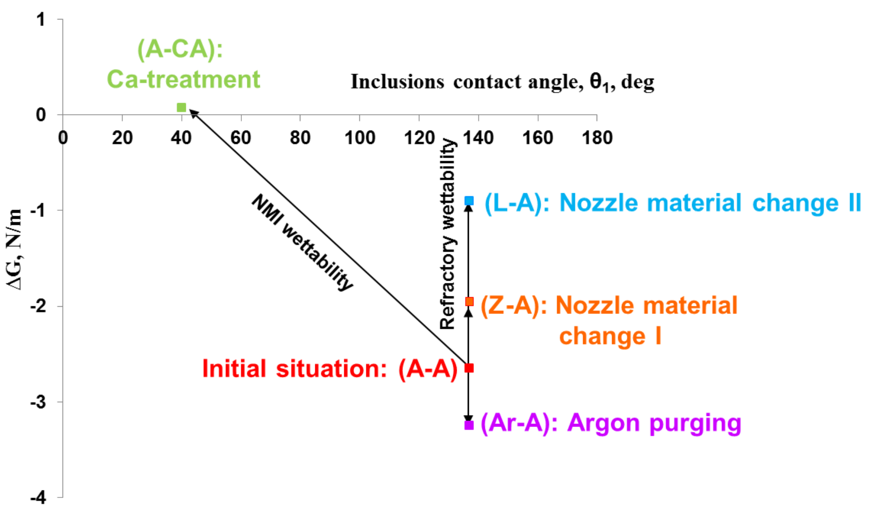

Figure 57. Change of free energy from the immersed state to the separated state for the cases studied in **Section 3** and **4.**

The attractive forces, such as adhesion force and capillary force, depend on the volume of the fluid phase. In **Figure 58** is represented the attractive force in function of the equivalent bubble radius of the fluid phase. The attractive force to keep a NMI at an interface decreases when the bubble volume increases. The dark-lines in the figure represent the capillary force for a NMI adhered at a steel/gas interface (**Equations (59)-(60)** in **Section 4.2.2.1**). The capillary force was calculated for the bubble sizes between the minimum and maximum values given in **Table 18**. The dots represent the adhesion force of a NMI adhered at a steel/refractory interface explained in **Section 1.2.1**. The volume and the equivalent bubble size of the bridge were calculated applying the procedure given in **Appendix D**. In addition, it is seen that the size of the NMI influences the attractive force. The attraction increases with the NMIs size for any of the interfaces.

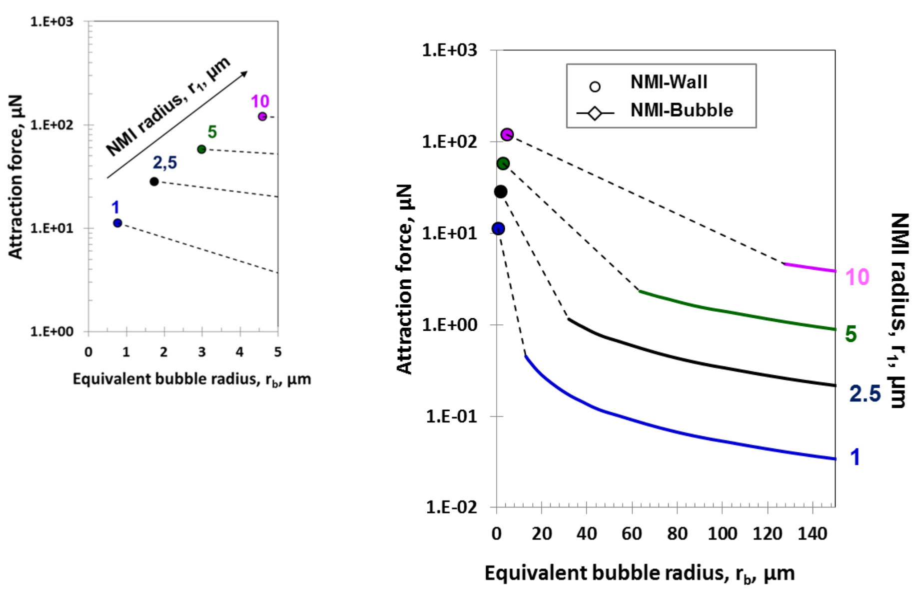

Figure 58. Comparison between attractive forces between: **(1)** NMI/Nozzle wall, and **(2)** NMI/Gas bubble.

In **Figure 59**, the comparison of the results from the detachment criteria for a NMI at a steel/refractory interface and for a NMI at a steel/gas interface is presented. In general, the following tendencies are observed:

(1) **At steel/refractory interface:** Smaller NMIs need a high steel velocity at their mass center to be lifted off from the interface. Hence, small inclusions are much more difficult to lift-off after coming into contact with the interface. Whereas bigger inclusions will be easier to lift off from the interface.

(2) **At steel/gas interface:** The big inclusions will feel more stable at the gas/bubble interface than small inclusions.

In general, it is seen that small inclusions present more risk to clog the SEN. This agrees with industrial practice results where the inclusions found in the clogging deposits are in a range of 1-10 µm. And thus, argon purging is needed in order to protect from the contact between the NMIs and the SEN wall, acting as a successful clogging countermeasure.

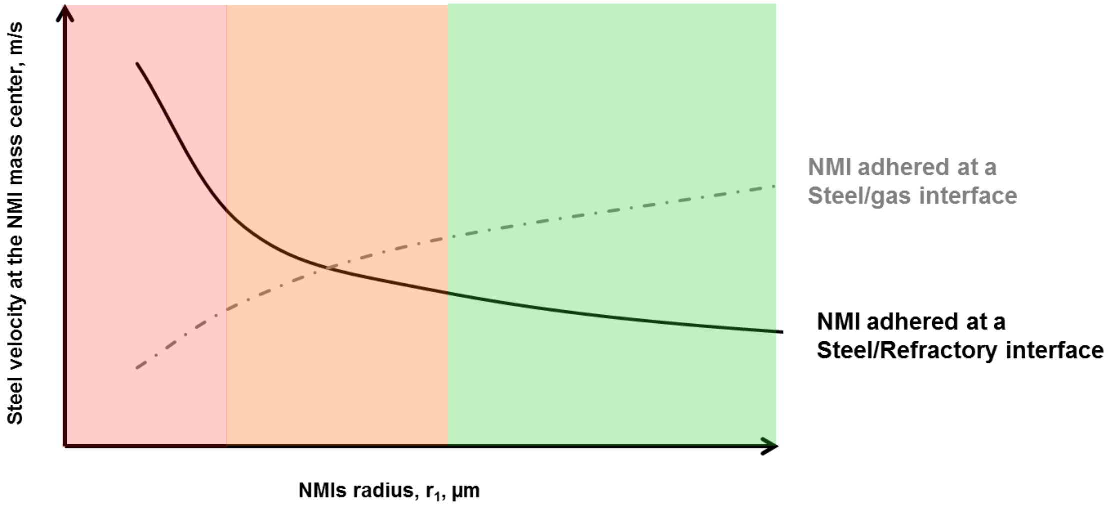

Figure 59. Comparison between the minimum steel flow velocities at the inclusion mass center needed to detach an inclusion from a steel/refractory and a steel/gas interface for different NMIs size.

5 Conclusions

The relevance of certain clogging parameters onto the NMIs deposition at steel/refractory and steel/gas interfaces is summarized here:

(1) Interfacial properties in the system NMI-steel-refractory

(a) The role of interfacial properties on clogging in continuous casting has been frequently addressed in literature. The present work focusses on the observation of the behavior of NMIs at steel/refractory systems by means of HT-LSCM and the quantitative determination of capillary forces which act between the particles. A theoretical model for the prediction of the capillary forces, with input values of wetting angles from own measurement with a HT-DSA apparatus, shows a notable consistence with the HT-LSCM results, in **Chapter 2**.

(b) In **Chapter 3**, the clogging tendency of particles at the interface steel/refractory is represented by deriving a model which predicts the critical conditions needed for detachment of NMIs. Here, the wetting of inclusions and refractories by the liquid steel are proved to be the key parameters. Thus, the significant role of interfacial properties can be considered as proven; not only for NMIs at the liquid steel surface but also for NMIs in the bulk.

(c) Non-wetting systems of steel/NMI result in high adhesion forces-and hence their attraction is promoted by the refractory/steel interface. This gives a good explanation for the usually high clogging sensitivity of Al_2O_3 particles. The modification of NMIs with e.g. addition of calcium results in (at least) partial liquification and consequently, the change from a non-wetting to a wetting system. Finally, a repulsive adhesion force that suppresses clogging is observed and proved in **Section 2.1.2.2.1**. This show consistence with the operational practice in steel plants over more than three decades.

(d) Besides the morphology of the inclusion also the steel composition and the refractory material may influence the clogging tendency. Alumina shows a wetting angle of 137 deg. with ULC steel and only 98 deg. with a Ca-treated steel (**Section 2.1.2.2**). Hence alumina particles should show a high clogging tendency in the casting of ULC steel whereas they are rather harmless in Ca-treated steels (where they should not exist through the calcium addition).

(e) In case of refractories, the potential for the reduction of the wetting angle with the liquid steel is a measure to lower the tendency of NMIs to clog. However, it should be noted that a non-wetting system between refractory and steel is needed to prevent the penetration of the steel into refractory porosities and avoid steel/refractory reactions and thus to control the SEN-erosion.

(f) A liquid neck between NMI and refractory, instead of the usually assumed gaseous neck helps to make the particle detachment much easier, as shown in **Section 3.2**. An already realized technology is the in-situ modification of NMIs at the steel/refractory interface: A refractory with selected reactivity with the Al_2O_3 particle may e.g. result in the formation of a liquid calcium aluminate as reaction product. This lowers the adhesion force between refractory and NMI by almost an order of magnitude.

(2) NMIs population

(a) The chemical composition of micro inclusions as well as their morphology are the consequence of the ladle treatment practice. Product quality demands may limit the modification of the NMIs morphology; e.g., when a Ca-treatment is strictly forbidden, as the resulting calcium aluminates are considered to be harmful for the product quality. For this reason, the effective Ca-treatment cannot always be selected to lower the clogging problems.

(b) Here, number and size distribution of the NMIs remain as influencing parameters: A high number of NMIs results in a higher number of collisions between inclusions and the steel/refractory interface. This is in accordance with the common opinion that a ‘clean’ steel is less clogging sensitive than an ‘unclean’ steel. A new perspective is, according to the detachment model, that small inclusions are harder to detach and consequently, a higher number of small inclusions should be more critical than a higher number of large inclusions. According to common definitions, the latter steel grade would be considered as ‘unclean’ but nevertheless be less critical to cast.

(3) Hydrodynamics, temperature and purging

(a) The present work does not consider in detail the hydrodynamics in the SEN. Local turbulences as well pressure drops due to changes of the cross-sectional area of the SEN may have a significant influence on clogging and may even be the dominating influencing factor. Turbulences may result in a higher number of collisions between NMIs and the steel/refractory interface but also promote the detachment of particles as predicted in this work. Local pressure drops may influence chemical equilibria and promote chemical reactions between steel and refractory. The suction of air into the fluid flow control system or the influencing of the pressure difference in the cavity between NMI and refractory are further possible consequences.

(b) Same as for the hydrodynamics, the temperature loss in the SEN was not taken into consideration here. The increasing driving force towards the nucleation of particles with decreasing temperature at the steel/refractory interface is evident but also the interfacial properties will be influenced by the temperature.

(c) Purging with argon results in the adhesion of bubbles at the steel/refractory interface. The driving force for separation at the steel/gas interface is higher compared to the steel/refractory interface, as shown in **Figure 57**. Nevertheless, NMIs are also easier to detach and the main benefit of this dynamic attachment/detachment system is that bubbles (or a gas film along the steel/refractory interface) prevent the NMIs from sintering to the refractory and thus the formation of a stable clog. The limit of the purging rate is related with the entrapment of bubbles in the solidifying shell and consequently with the worsening of the surface quality of the cast product.

Under all investigated clogging countermeasures, the modification (partial liquification) of inclusions and purging of the SEN should have the highest efficiency. Wetting in the steel/NMI and steel/refractory system are significant influencing parameters but may only be changed in-between certain limits. The in-situ modification of inclusions by reactive refractories results in the formation of a liquid layer between NMI and refractory. This is a further promising way to reduce the clogging tendency of certain steel grades. Small NMIs seem to be more harmful than larger ones. This may help to explain so far not sufficiently understood differences in the clogging behavior of otherwise similar steel grades but cannot be seen as an effective countermeasure.

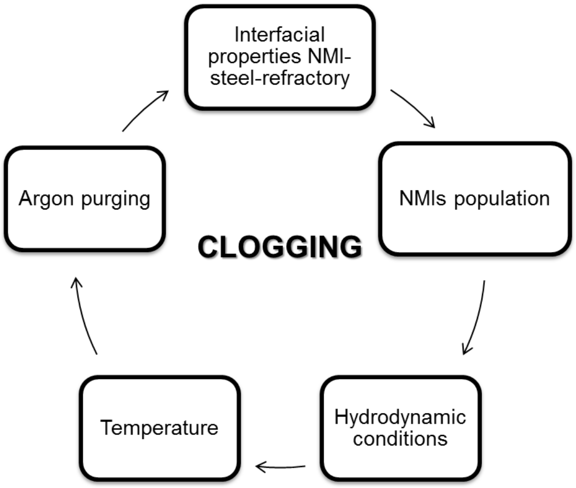

Figure 60. Clogging important parameters.

Appendix A. Free energy change for NMIs separation at different interfaces

The change in the Gibbs free energy of the system at constant temperature and pressure can be related to the change in the interfacial energies as the inclusion goes from the immersed state to the separated state[53–55,271,272]. The free energy change for separation of NMIs at different interfaces will be deduced here. Three different interfaces will be studied: (1) Molten steel/Nozzle wall, (2) Molten steel/slag, and (3) Molten steel/argon gas.

(1) Molten steel/Nozzle wall

The change in Gibbs free energy from a micro-oxidic inclusion immersed in molten steel to the separate state is:

$$\Delta G = \sigma_{i\text{-}r} - \sigma_{i\text{-}s} - \sigma_{r\text{-}s} \tag{A.1}$$

where σ is the surface tension between two materials, the subscript 'i-r' indicates inclusion-refractory, 'i-s' inclusion-molten steel and 'r-s' refractory-molten steel.

The Young's equation, given in **Equation (A.2)**, for a solid especimen over a solid substrate, allow to determine difference between the surface and interfacial tensions of the solid phase where 'i', 's' and 'g' denote the solid, molten steel and gas phases, respectively. See **Figure A.1-a)** and for more detail[7].

$$\sigma_{i\text{-}g} = \sigma_{i\text{-}s} + \sigma_{s\text{-}g}\cos(\theta_i) \tag{A.2}$$

Where θ_i is the contact angle between the solid phase and the molten steel.

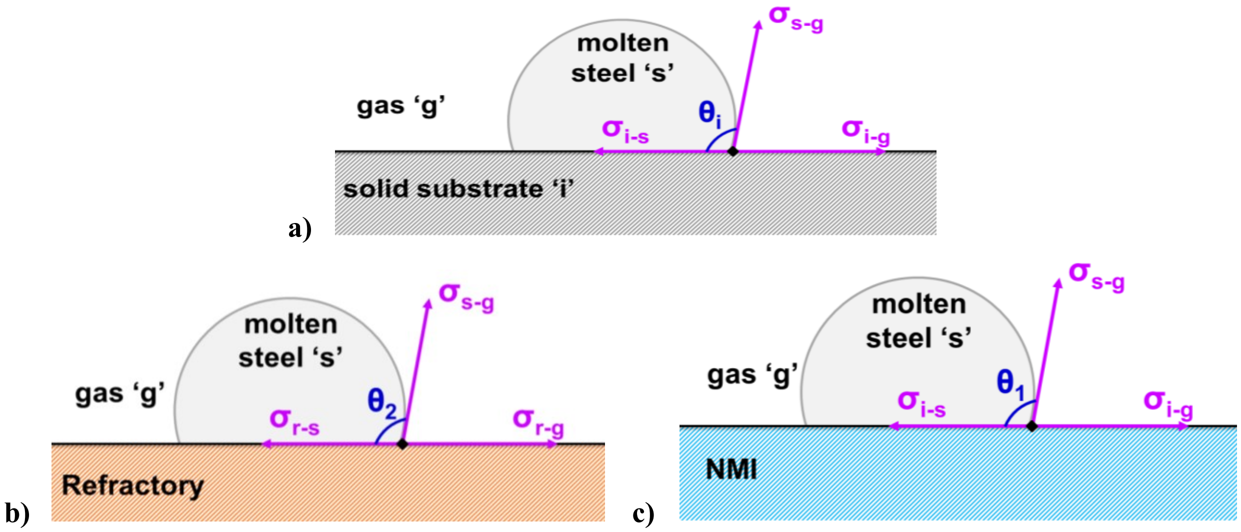

Figure A. 1.a) Graphic explanation of Young's equation. Modified from references[7,54], **b)** graphic explanation of Young's equation between molten steel and a solid refractory, and **c)** graphic explanation of Young's equation between molten steel and a solid NMI.

From **Equation (A.2)**, two special equations in function of the solid material 'i', will be obtained

(1) For a refractory (i=r), **Equation (A.2)** turns into:

$$\sigma_{r\text{-}g} = \sigma_{r\text{-}s} + \sigma_{s\text{-}g}\cos(\theta_2) \tag{A.3}$$

where θ_2 the contact angle between the refractory and the steel. See more detail on the graphic explanation given in **Figure A.1-b)**.

(1) For a solid NMI (i=i), **Equation (A.2)** turns into:

$$\sigma_{i\text{-}g} = \sigma_{i\text{-}s} + \sigma_{s\text{-}g}\cos(\theta_1) \tag{A.4}$$

where θ_1 the contact angle between the NMI and the steel. See more detail on the graphic explanation given in **Figure A.1-c)**.

Replacing **Equation (A.3)** and **(A.4)** in **Equation (A.1)** it is obtained:

$$\Delta G = \sigma_{i\text{-}r} - \left(\sigma_{i\text{-}g} - \sigma_{s\text{-}g}\cos(\theta_1)\right) - \left(\sigma_{r\text{-}g} - \sigma_{s\text{-}g}\cos(\theta_2)\right) \tag{A.5}$$

where

$$\sigma = \sigma_{i\text{-}g} + \sigma_{r\text{-}g} \tag{A.6}$$

Therefore the free energy change for separation of a solid non-metallic inclusion in the refractory wall is

$$\Delta G = \sigma_{s\text{-}g} \cdot [\cos(\theta_1) + \cos(\theta_2)] \quad \textbf{(A.7)}$$

(2) Molten steel/slag layer

If a NMI separates from the molten steel bath to a molten steel/slag interface, the free energy change in the system is given by[54]:

$$\Delta G = \sigma_{i\text{-slag}} - \sigma_{i\text{-s}} - \sigma_{s\text{-slag}} \quad \textbf{(A.8)}$$

For ‘i’ inclusion, ‘s’ steel and ‘slag’ slag phase.

The Young’s equation for a solid especimen over a solid substrate, allow to determine difference between the surface and interfacial tensions of the solid phase. **Equation (A.9)** represents the Young’s equation for a molten steel over a solid substrate, see **Figure A.2-a)**, and **Equation (A.10)** represents the Young’s equation for a liquid slag over a solid substrate, see **Figure A.2-b)**.

$$\sigma_{i\text{-g}} = \sigma_{i\text{-s}} + \sigma_{s\text{-g}} \cos(\theta_{i\text{-s}}) \quad \textbf{(A.9)} \qquad \sigma_{i\text{-g}} = \sigma_{i\text{-slag}} + \sigma_{slag\text{-g}} \cos(\theta_{i\text{-slag}}) \quad \textbf{(A.10)}$$

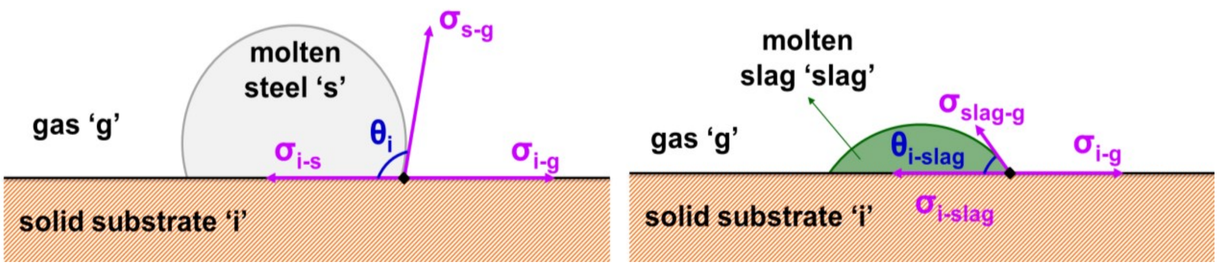

a) **b)**

Figure A. 2. Graphic explanation of Young's equation. a) Molten steel over a solid substrate, and b) Liquid slag over a solid substrate. Modified from references[7,54]

Substituting **Equation (A.9)** and **(A.10)** into **Equation (A.8)**, it is obtained:

$$\Delta G = [-\sigma_{slag-g} \cos(\theta_{i-slag})] - [-\sigma_{s-g} \cos(\theta_{i-s})] - \sigma_{s\text{-slag}} \quad \textbf{(A.11)}$$

Knowing that the $\theta_{i-slag} \rightarrow 0$, means that $\cos(\theta_{i-slag}) \rightarrow 1$, and thus, Equation (11) gets simplified:

$$\Delta G = -\sigma_{slag-g} + \sigma_{s-g}\cos(\theta_{i-s}) - \sigma_{\text{s-slag}} \tag{A.12}$$

The interfacial tension between two immiscible liquids, see **Figure A.3**, defined by Antonov's law, which is a simplification of the Young's law for $\cos\left(\theta_{\text{slag-s}}\right) \rightarrow 1 \; due \; to \; \theta_{\text{slag-s}} \rightarrow 0 \; deg.$

$$\sigma_{\text{s-slag}} = \sigma_{\text{s-g}} - \sigma_{\text{slag-g}}\cos\left(\theta_{\text{slag-s}}\right) \rightarrow \sigma_{\text{s-slag}} = \sigma_{\text{s-g}} - \sigma_{\text{slag-g}} \tag{A.13}$$

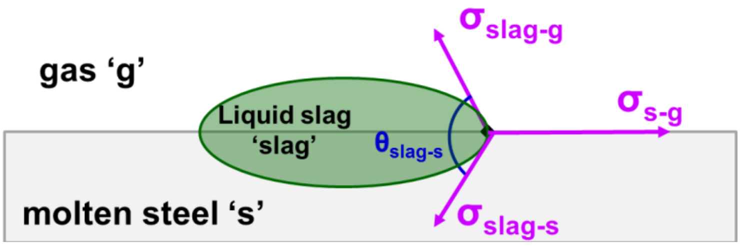

Figure A. 3. Graphic explanation of Antonov's equation between two immiscible fluids. Modified from references[7,54]

Substituting **Equation (A.13)** into **Equation (A.12)**, it is obtained:

$$\Delta G = -\left(\sigma_{slag-g} + \sigma_{\text{s-slag}}\right) + \sigma_{s-g}\cos(\theta_{i-s}) = -\left(\sigma_{\text{s-g}}\right) + \sigma_{s-g}\cos(\theta_{i-s}) \tag{A.14}$$

$$\Delta G = \sigma_{s-g} \cdot [\cos(\theta_{i-s}) - 1] \tag{A.15}$$

(3) Molten steel/argon gas layer

If a NMI separates from the molten steel bath to a molten steel/slag interface, the free energy change in the system is given by[54]:

$$\Delta G = \sigma_{\text{i-g}} - \sigma_{\text{i-s}} - \sigma_{\text{s-g}} \tag{A.16}$$

For 'i' inclusion, 'g' gas and 's' steel.

The Young's equation for a solid especimen over a solid substrates, allow to determine difference between the surface and interfacial tensions of the solid phase where 'i', 's' and 'g' denote the solid, molten steel and gas phases, respectively. See **Figure A.1** and **Equation (A.3)** for more detail[7]. Substituting

Equation (A.3) into **Equation (A.16)**, it is obtained the free energy change for the separation of a NMI at a metal-gas interface:

$$\Delta G = \left[\sigma_{i-s} + \sigma_{s-g} \cos(\theta_{i-s}) \right] - \sigma_{i\text{-}s} - \sigma_{s\text{-}g} = \sigma_{s-g} \cos(\theta_{i-s}) - \sigma_{s\text{-}g} \quad \textbf{(A.17)}$$

$$\Delta G = \sigma_{s\text{-}g} \cdot (\cos \theta_{i\text{-}s} - 1) \quad \textbf{(A.18)}$$

Appendix B. Effect of the cavity difference pressure on the adhesion force calculation.

As already mentioned in **Section 2.1.2.1.1**, the mean curvature of the fluid bridge and the pressure difference across the steel/cavity interface are not directly known due to the lack of in situ observations. Therefore, it was decided to approximated the cavity geometry and to estimate the difference pressure as $1.8 \cdot 10^5$ Pa[43].

However, there are no accurate measures of this pressure value. A way to confront this issue is to extract agglomerated inclusions and measured directly the cavity geometry radius in order to calculate the Young-Laplace equation given by **Equation (3)**. Nevertheless, due to shrinkage of the cavity this kind of analysis may only provide an approximation to the real value.

Ueshima and Mizoguchi et al.[48,49] performed different expeirments where they extrated alumina clusters from steel. They found that liquid FeO was acting as a binder of the inclusions. They suggest that the FeO would come from oxygen contamination from ferroalloy additives, residual steel adhering the the refractory surface of ladles and vessels, and air entraiment.

Pair (1)	Pair (2)	Pair (3)	Pair (4)
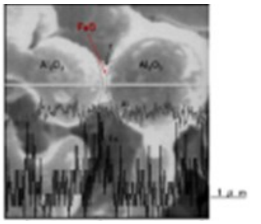	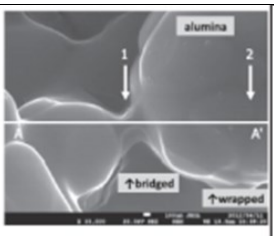	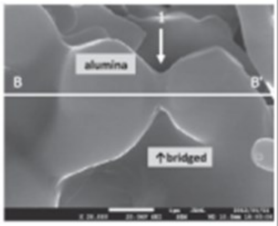	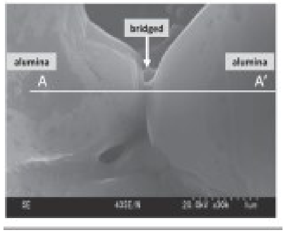

a)[49] **b)**[48] **c)**[48] **d)**[48]

Figure B. 1. Four SEN images of alumina clusters from molten steel using a slime method[48,49].

Four SEN images of alumina clusters[48,49] extrated from molten steel using a slime method are presented in **Figure B.1 a-d)**. From each image, the particle radii, r_1 and r_2, and the geometry radii, R_1 and R_2, have been measured and plotted in **Table B.1**. A surface tension of 0.68 N/m have been chosen to be the surface tension between the molten steel and the liquid FeO. From the Young-Laplace equation (**Equation**

(3)), it can be calculated the difference pressure when the geometry of the bridge and the surface tension of the molten steel are known, this value is shown in **Table B.1.**.

Table B. 1. Cluster geometry measured and different pressure calculated and estimated.

Pair	r_1 µm	r_2 µm	R_1 µm	R_2 µm	σ N/m	$\Delta P_{calculated}$ Pa	$\Delta P_{estimated}$ Pa
(1)	4.4	5.6	0.3	0.6	0,68	$8.46 \cdot 10^5$	$1.8 \cdot 10^5$
(2)	1.3	2.6	0.2	0.2		$11.3 \cdot 10^5$	
(3)	2.8	2.1	0.2	0.4		$23.8 \cdot 10^5$	
(4)	3.7	3.2	0.2	0.3		$21.9 \cdot 10^5$	

The difference pressure between the cavity and the molten steel calculated from the measured cavity radii, seen in **Table B.1.**, shows a higher pressure than the estimated presented in **Section 2.1.2.1.1.** The adhesion force, from the estimated and calculated difference pressure, is compared in **Figure B.2**. It is seen that the adhesion force values are in the same order of magnitude. From this figure it is suggested that the estimation of a pressure does not introduce a big error on the results. And therefore, the difference pressure will be estimated in the current work.

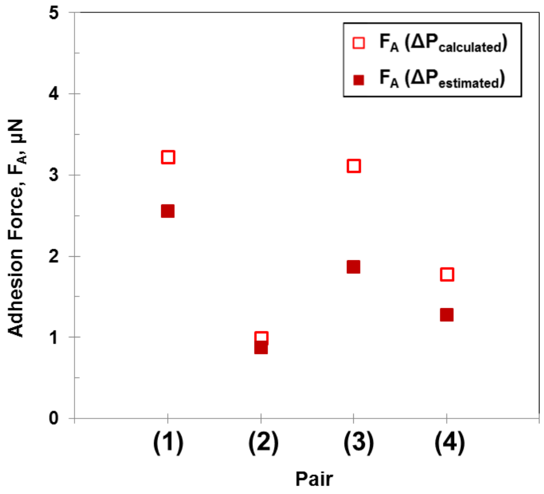

Figure B. 2. Adhesion force for different particles pairs: Adhesion force at $\Delta P_{estimated}$ and adhesion force at $\Delta P_{calculated}$.

Appendix C. Bridge geometry approximation

In order to calculate the geometry of the bridge, given by R_1 and R_2, two approximations can be done:

○ Approach (1): Toroidal approximation

The model is based on a geometrical approach based on the toroidal shape of the cavity. The steps for the calculation of the geometry of the bridge, R_1 and R_2, between two particles with different sizes and at certain distance from each other is given here[43,45]. Two special cases are simplified from the general model: **(1)** Two different particles sizes at zero distance, and **(2)** same particle type and same size.

When the distance between two spherical particles (with different size) is different from zero, the following steps are needed to calculated the adhesion force:

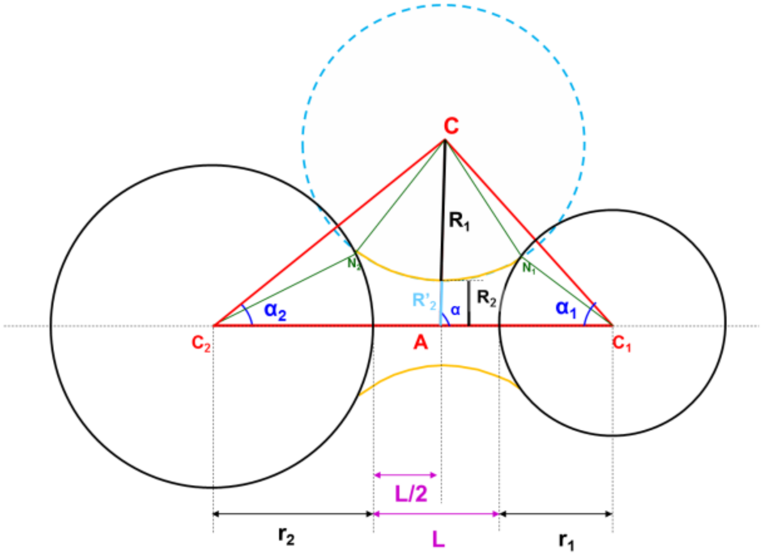

Figure C. 1. Scheme for the calculation of the geometry radii between two spheres of different sizes and at certain distance of each other.

Applying the cosine law for the Triangle A and B represented in **Figure C.2** the following **Equations (C.1) - (C.2)** are obtained:

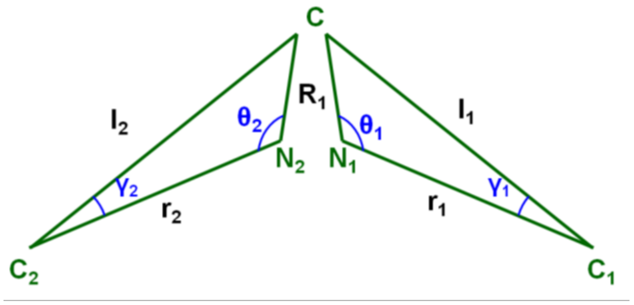

Figure C. 2. Triangle A (left) and B (right).

Triangle A:
$$l_2^2 = r_2^2 + R_1^2 - 2r_2R_1\cos\theta_2 \tag{C.1}$$

Triangle B:
$$I_1^2 = r_1^2 + R_1^2 - 2r_1R_1\cos\theta_1 \tag{C.2}$$

Applying again the cosine law to the Triangle C and D represented in **Figure C.3** the following **Equations (C.3) - (C.4)** are obtained:

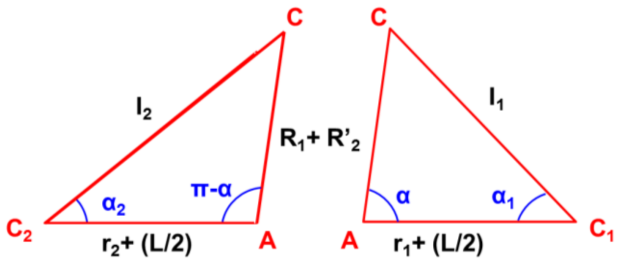

Figure C. 3. Triangle C (left) and D (right).

Triangle C:
$$l_2^2 = \left(r_2 + \frac{L}{2}\right)^2 + (R_1 + R'_2)^2 - 2\left(r_2 + \frac{L}{2}\right)(R_1 + R'_2)\cos\alpha \tag{C.3}$$

$$I_1^2 = \left(r_1 + \frac{L}{2}\right)^2 + (R_1 + R'_2)^2 - 2\left(r_1 + \frac{L}{2}\right)(R_1 + R'_2)\cos(\pi - \alpha)^*$$

$$\rightarrow$$

Triangle D:
$$l_1^2 = \left(r_1 + \frac{L}{2}\right)^2 + (R_1 + R'_2)^2 + 2\left(r_1 + \frac{d}{2}\right)(R_1 + R'_2)\cos\alpha \tag{C.4}$$

$$^*\cos(\pi - \alpha) = \cos\pi \cdot \cos\alpha + \sin\pi \cdot \sin\alpha = -\cos\alpha;\ \cos\pi = -1;\ \sin\pi = 0$$

Equation (C.2) and **Equation (C.4)** are equalized to obtain the expression for cos α in **Equation (C.5)**:

$$r_1^2 + R_1^2 - 2r_1R_1\cos\theta_1 = \left(r_1 + \frac{L}{2}\right)^2 + (R_1 + R'_2)^2 + 2\left(r_1 + \frac{L}{2}\right)(R_1 + R'_2)\cos\alpha \tag{C.5}$$

$$\rightarrow \cos\alpha = -\frac{\mathrm{R}_1(\mathrm{r}_2\cos\theta_2 - \mathrm{r}_1\cos\theta_1) - \mathrm{L}(\mathrm{r}_1 - \mathrm{r}_2)}{(\mathrm{R}_1 + \mathrm{R}_2')(\mathrm{r}_1 + \mathrm{r}_2 + \mathrm{L})}$$

Equation (C.1) and (C.3) are equalized and multiply by r$_2$ obtaining **Equation (C.6)**:

$$\begin{aligned}&\mathrm{r}_2\mathrm{r}_1^2 + \mathrm{r}_2\mathrm{R}_1^2 - \mathrm{r}_2 2\mathrm{r}_1\mathrm{R}_1\cos\theta_1\\ &\quad = \mathrm{r}_2\left(\mathrm{r}_1 + \frac{\mathrm{L}}{2}\right)^2 + \mathrm{r}_2(\mathrm{R}_1 + \mathrm{R}_2')^2 + 2\mathrm{r}_2\left(\mathrm{r}_1 + \frac{\mathrm{L}}{2}\right)(\mathrm{R}_1 + \mathrm{R}_2')\cos\alpha\end{aligned} \tag{C.6}$$

Equation (C.2) and **(C.4)** are equalized and multiply by r$_1$ obtaining **Equation (C.7):**

$$\begin{aligned}&\mathrm{r}_1\mathrm{r}_2^2 + \mathrm{r}_1\mathrm{R}_1^2 - \mathrm{r}_1 2\mathrm{r}_2\mathrm{R}_1\cos\theta_2\\ &\quad = \mathrm{r}_1\left(\mathrm{r}_2 + \frac{\mathrm{L}}{2}\right)^2 + \mathrm{r}_1(\mathrm{R}_1 + \mathrm{R}_2')^2 - 2\mathrm{r}_1\left(\mathrm{r}_2 + \frac{\mathrm{L}}{2}\right)(\mathrm{R}_1 + \mathrm{R}_2')\cos\alpha\end{aligned} \tag{C.7}$$

Summing **Equation (C.7) and (C.8)** and substituting **Equation (C.5)**, **Equation (C.8)** is obtained as follows:

$$\begin{aligned}&-2\mathrm{r}_1\mathrm{r}_2[\mathrm{R}_1(\cos\theta_1 + \cos\theta_2) + \mathrm{L}] - (\mathrm{r}_1 + \mathrm{r}_2)[\mathrm{L}^2 + 2\mathrm{R}_1 R_2' + \mathrm{R}_2'^2]\\ &\quad - 2\left[\frac{\mathrm{L}}{2}(\mathrm{r}_1 - \mathrm{r}_2)\right]\left[-\frac{\mathrm{R}_1(\mathrm{r}_2\cos\theta_2 - \mathrm{r}_1\cos\theta_1) - \mathrm{L}(\mathrm{r}_1 - \mathrm{r}_2)}{(\mathrm{r}_1 + \mathrm{r}_2 + \mathrm{L})}\right] = 0\end{aligned} \tag{C.8}$$

R$_1$ is obtained from the Young-Laplace equation, and expressed by **Equation (C.9)**

$$\Delta\mathrm{P} = \sigma\left(\frac{1}{\mathrm{R}_1} - \frac{1}{R_2'}\right) \rightarrow \mathrm{R}_1 = \frac{R_2'\sigma}{\sigma + \Delta\mathrm{P}\cdot R_2'} \tag{C.9}$$

Substituting now **Equation (C.9)** in **Equation (C.8)**. The following **Equation (C.10)** results:

$$\begin{aligned}&-\Delta\mathrm{P}(\mathrm{r}_1+\mathrm{r}_2)\cdot\mathbf{R}_2'^3\\ &- 3\sigma(\mathrm{r}_1+\mathrm{r}_2)\cdot\mathbf{R}_2'^2 + \Bigg\{[-2\mathrm{r}_1\mathrm{r}_2\sigma(\cos\theta_1 + \cos\theta_2)] - [2\mathrm{r}_1\mathrm{r}_2\mathrm{L}\Delta\mathrm{P}] - [\mathrm{L}^2(\mathrm{r}_1 + \mathrm{r}_2)\Delta\mathrm{P}]\\ &+ \left[\frac{\mathrm{L}\sigma(\mathrm{r}_1 - \mathrm{r}_2)(\mathrm{r}_2\cos\theta_2 - \mathrm{r}_1\cos\theta_1) + \Delta\mathrm{P}\mathrm{L}^2(\mathrm{r}_1 - \mathrm{r}_2)^2}{(\mathrm{r}_1 + \mathrm{r}_2 + \mathrm{d})}\right]\Bigg\}\mathbf{R}_2' + \mathrm{d}\sigma\Bigg[-2\mathrm{r}_1\mathrm{r}_2\\ &+ \mathrm{L}(\mathrm{r}_1 + \mathrm{r}_2) + \frac{\mathrm{L}(\mathrm{r}_1 - \mathrm{r}_2)^2}{(\mathrm{r}_1 + \mathrm{r}_2 + \mathrm{L})}\Bigg] = 0 \rightarrow \mathbf{R}_2'\end{aligned} \tag{C.10}$$

Equation (C.10) can be simplefied for two special cases:

i) Two different particles sizes at zero distance **(L=0)**:

$$\Delta P(r_1+r_2)\cdot \mathbf{R}_2'^2 + 3\sigma(r_1+r_2)\cdot \mathbf{R}_2' + 2r_1 r_2 \sigma(\cos\theta_1 + \cos\theta_2) = 0$$

$$\rightarrow \mathbf{R}_2' = \frac{-[3\sigma(r_1+r_2)] \pm \sqrt{[3\sigma(r_1+r_2)]^2 - 4[\Delta P(r_1+r_2)][2r_1 r_2 \sigma(\cos\theta_1 + \cos\theta_2)]}}{2[\Delta P(r_1+r_2)]} \quad \textbf{(C.11)}$$

ii) Same particle type ($\boldsymbol{\theta_1 = \theta_2 = \theta}$) and same size ($\mathbf{r_1 = r_2 = r}$):

$$\Delta P\cdot \mathbf{R}_2'^2 + 3\sigma\cdot \mathbf{R}_2' + 2r\sigma\cos\theta = 0 \rightarrow \mathbf{R}_2' = \frac{-3\sigma + \sqrt{(3\sigma)^2 - 4\cdot\Delta P\cdot(2r\sigma\cos\theta)}}{2\cdot\Delta P} \quad \textbf{(C.12)}$$

R_2 is calculated by solving the **Equation (C.13)** given by **Figure C.4**.

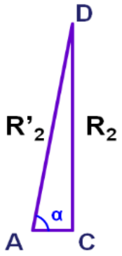

Figure C. 4. Triangle ADC for the calculation of R_2.

$$R_2 = R_2' \cdot \sin\alpha \quad \textbf{(C.13)}$$

○ Approach (2): Energy minimization

The geometry of the bridge is described by a circle. Its geometry will be represented by R_1 and R_2 expressed in function of the angle β. Zheng et al.[50,64] determined the filling angle, ß, by minimizing the Gibbs free energy of the gas cavity as expressed with **Equation (C.14)**:

$$G = P_o - Nk_B T \ln V + \sigma_{sg} A_{sg} + (\sigma_{ig} - \sigma_{is}) A_{ig} \quad \textbf{(C.14)}$$

where A_{sg} is the molten iron-gas area (m^2), A_{ig} is the inclusion-gas area (m^2), V is the volume of the gas cavity (m^3), P_o is the pressure in the molten iron and it is set to $1.013\cdot10^5$ Pa, and N is the number of gas molecules inside the cavity set to 0, considering that the partial pressure of molten iron and other elements, such as oxygen is very low.

Expressing V, A_{lg} and A_{sg} as a function of the filling angle ß, the equilibrium value of filling angle ß can be obtained from dG = f (ß) = 0. Then the attractive force can be calculated. This method is presented for two different cases: **(1)** Sphere-Sphere (S-S), and **(2)** Sphere-Plane (S-P). Both represented in **Figure C.5**.

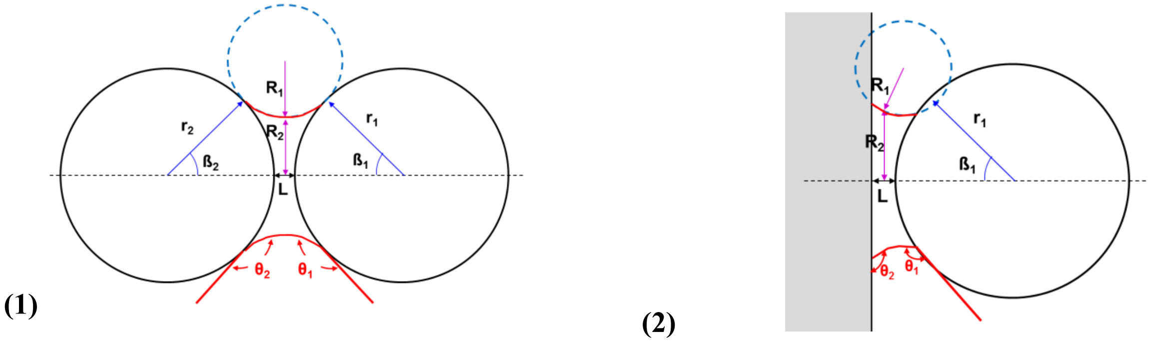

Figure C. 5. (1) Sphere-Sphere (S-S), and **(2)** Sphere-Plane (S-P).

(1) Sphere-sphere (S-S):

The cavity geometry parameters, R_1 and R_2, defined in function of the half-filling contact angles ß_1 and ß_2 are given in **Equation (C.15)** and **(C.16)**.

$$R_1 = -\frac{r_1(1-\cos \text{ß}_1) + r_2(1-\cos \text{ß}_2) + L}{\cos(\theta_1 - \text{ß}_1) + \cos(\theta_2 - \text{ß}_2)} \tag{C.15}$$

$$R_2 = r_1 \sin \text{ß}_1 - R_1[1 - \sin(\theta_1 - \text{ß}_1)] \tag{C.16}$$

Where r_1 and r_2 are the radii of the spheres 1 and 2, respectively, θ_1 and θ_2 are the contact angles of the sphere 1 and 2, respectively, and d is the interparticle distance.

The volume of the cavity, V_{S-S}, and the molten steel- gas area $A_{sg,S-S}$ and inclusion gas area $A_{ig,S-S}$ for two spherical particles are defined as

$$\begin{aligned} V_{S-S} = \pi \int_{R_1\cos(\theta_2-\text{ß}_2)}^{R_1\cos(\text{ß}_1-\theta_1)} \left(R_1 + R_2 - \sqrt{R_1^2 - y^2}\right)^2 dy \\ - \left[\left(\frac{\pi}{3} r_1^3 (2+\cos \text{ß}_1)(1-\cos \text{ß}_1)^2\right)\right. \\ \left. + \left(\frac{\pi}{3} r_2^3 (2+\cos \text{ß}_2)(1-\cos \text{ß}_2)^2\right)\right] \end{aligned} \tag{C.17}$$

$$A_{sg,S-S} = 2\pi \int_{\frac{3\pi}{2}-\theta_1+\text{ß}_1}^{\frac{\pi}{2}-\theta_2+\text{ß}_2} R_1(R_1 + R_2 + R_1\cos\theta)\, d\theta \tag{C.18}$$

$$A_{ig,S-S} = 2\pi r_1^2(1-\cos \text{ß}_1) + 2\pi r_2^2(1-\cos \text{ß}_2) \tag{C.19}$$

(2) Sphere-Plane (S-P):

The cavity geometry parameters, R_1 and R_2, defined in function of the half-filling contact angle ß_1, are given in **Equation (C.20)** and **(C.21)**.

$$R_1 = -\frac{r_1(1-\cos \text{ß}_1) + L}{\cos(\theta_1 - \text{ß}_1) + \cos(\theta_2)} \tag{C.20}$$

$$R_2 = r_1 \sin \text{ß}_1 - R_1[1 - \sin(\theta_1 - \text{ß}_1)] \tag{C.21}$$

Where r_1 are the radii of the sphere, θ_1 and θ_2 are the contact angles of the sphere and the plane, respectively, and d is the interparticle distance.

The volume of the cavity,V_{S-P}, and the molten steel- gas area $A_{sg,S-P}$ and inclusion gas area $A_{ig,S-P}$ for sphere-wall system are defined as

$$V_{S-P} = \pi \int_{R_1 \cos(\text{ß}_2)}^{R_1 \cos(\text{ß}_1 - \theta_1)} \left(R_1 + R_2 - \sqrt{R_1^2 - y^2}\right)^2 dy - \left[\left(\frac{\pi}{3} r_1^3 (2+\cos \text{ß}_1)(1-\cos \text{ß}_1)^2\right)\right] \tag{C.22}$$

$$A_{sg,S-P} = 2\pi \int_{\frac{3\pi}{2}-\theta_1+\text{ß}_1}^{\frac{\pi}{2}-\theta_2} R_1(R_1 + R_2 + R_1 \cos\theta)\, d\theta \tag{C.23}$$

$$A_{ig} = 2\pi r_1^2(1-\cos \text{ß}_1) + \pi(R_1 + R_2 - R_1\cos\theta_1)^2 \tag{C.24}$$

○ Comparison: Approach (1) vs. Approach (2)

Both approaches are compared in **Figure C.6**, for two different cases: **(1)** Sphere/Sphere (S/S) and, **(2)** Sphere/Wall (S/W). All the spherical bodies are alumina of 10 µm radius, and the wall is alumina with a radius much bigger than that of the sphere. In both cases, the surface tension chosen is set as 1.8 N/m and difference pressure as $1.013 \cdot 10^5$ Pa. As a result, a spherical body will adhere stronger to a plane wall than to another spherical body with the same size. In addition, it is observed that the force will decrease with the separation of the inclusions. Both approximations show good accuracy.

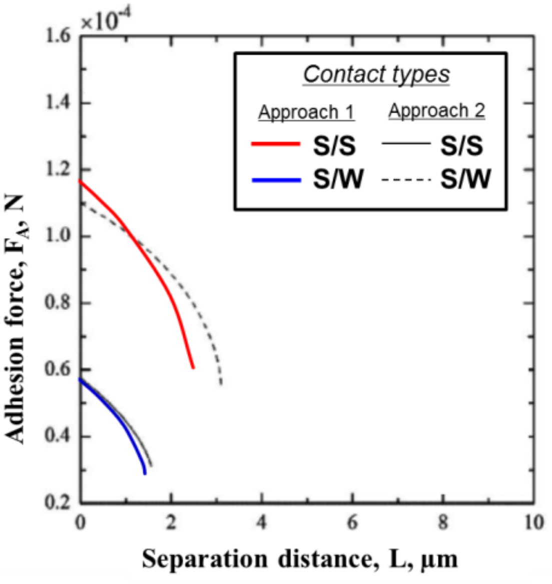

Figure C. 6. Adhesion force calculated applying **Approach (1)** (toroidal approximation) and **Approach (2)** (bridge volume approximation) for two cases: Sphere-Sphere (S-S) and Sphere-Plane (S-P) at certain separation distance.

Appendix D. Volume of the cavity bridge between NMI and nozzle wall using approach 1.

The volume of the bridge, V, between an adhered NMI and a nozzle wall can be calculated with the following equation**[50,64,273]**:

$$V = V_1 - V_2 \qquad \textbf{(D.1)}$$

$$V_1 = \int_{R_1 \cos\theta_1}^{R_1 \cos(\beta_1 - \theta_1)} \left(R_1 + R_2 - \sqrt{R_1^2 - x^2} \right)^2 dx \qquad \textbf{(D.2)}$$

$$V_2 = \frac{\pi}{3} r_1^3 (2 + \cos\beta_1)(1 - \cos\beta_1)^2 \qquad \textbf{(D.3)}$$

Where V_1 is the volume of the fluid in the cavity and V_2 is the volume of the NMI immersed in the bridge, $ß_1$ is the half-filling angle, R_1 and R_2 are the cavity radius (In this case the radius obtained in the **Approach 1: Toroidal approximation**, given in **Appendix C**, will be used for the following calculations), and r_1 is the NMI radius. In order to solve **Equations (D.1-D.3)**, it is needed the value of the half-filling angle, $ß_1$, which is obtained from the following equations (for a distance between the bodies equal to zero (L=0)):

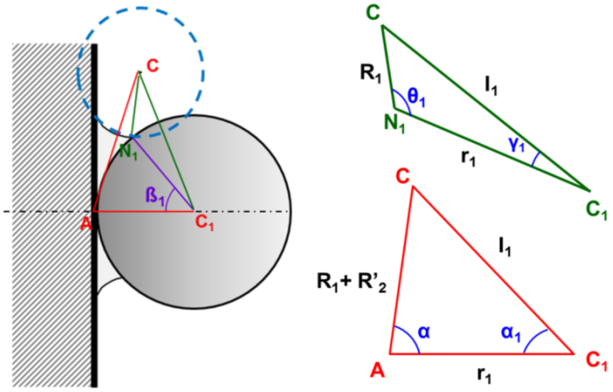

Figure D. 1. Geometrical scheme to calculate the half-filling angle β_1.

$$\mathrm{I}_1^2 = \mathrm{r}_1^2 + \mathrm{R}_1^2 - 2\mathrm{r}_1\mathrm{R}_1 \cos\theta_1 \tag{D.4}$$

$$\alpha_1 = \mathrm{acos}\left(\frac{(\mathrm{R}_1 + \mathrm{R}_2)^2 - \mathrm{r}_1^2 - \mathrm{I}_1^2}{-2\mathrm{r}_1\mathrm{I}_1}\right) \tag{D.5}$$

$$\gamma_1 = \mathrm{acos}\left(\frac{\mathrm{R}_1^2 - \mathrm{r}_1^2 - \mathrm{I}_1^2}{-2\mathrm{r}_1\mathrm{I}_1}\right) \tag{D.6}$$

$$\beta_1 = \alpha_1 - \gamma_1 \tag{D.7}$$

In order to be able to compare, the volume of the bridge with the case of the argon bubble attached to the SEN wall. A bubble equivalent radius of the bridge will be given as follows:

$$\mathrm{V} = \frac{4}{3}\pi r_b^3 \rightarrow r_b = \sqrt[3]{\frac{3V}{4\pi}} \tag{D.8}$$

Appendix E. Kralchevsky-Paunov's theoretical capillary attraction force. Procedure of calculation

The aim is to calculate the capillary force given in **Equation (38)**:

$$F = 2\pi\sigma\frac{Q_1Q_2}{L} \quad \forall \ c_k \ll L \ll q^{-1}; \quad k = 1,2 \tag{E.1}$$

The material parameters: surface tension, capillary distance, density ratio, and contact angles and the geometrical paramenters: radius, and inter-particle distance, are known (for k=1, 2). **Figure E.1** gives and schematic overview of the known parameters (mark in green) and the unknown parameters (given in red). The iterative procedure[45,251] is formed by 3 initial steps and after repeating the procedure from steps 2 until convergence is obtained.

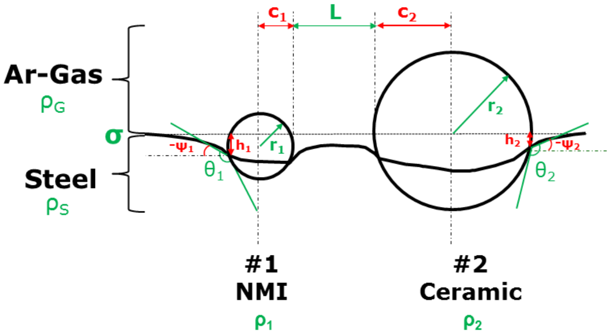

σ = surface tension (N/m)

r_k = particle radius (m)

θ_k = particle contact angle (rad)

ρ_S = steel density (kg/m^3)

ρ_G = gas density (kg/m^3)

ρ_k = particle density (kg/m^3)

L = interparticle distance (m)

c_k = radius of contact line (m)

h_k = meniscus height (m)

ψ_k= meniscus slope at contact line(rad)

(k = 1,2)

Figure E. 1. Schematic diagram of capillary meniscus around two spherical particles. The parameters given in green are known and in red are unknown. Modified from reference[247].

(1) **Step 1:** Starting values with index '0' are calculated for infinite separation between particles (single particle) from the following relations:

$$Q_k^{(0)} = Q_{k\infty} = \frac{1}{6} q^2 r_k^3 \left(2 - 4D_k + 3\cos\theta_k - \cos\theta_k^3\right) \tag{E.1}$$

$$c_k^{(0)} = c_{k\infty} = \frac{1}{2}\left[r_k \sin\theta_k + \left(r_k^2 \sin\theta_k^2 + 4Q_k r_k \cos\theta_k\right)^{\frac{1}{2}}\right] \tag{E.2}$$

$$D_k = \frac{\left(\rho_k - \rho_{II}\right)}{\left(\rho_I - \rho_{II}\right)} \tag{E.3}$$

$$\psi_k^{(0)} = \psi_{k\infty} = \sin^{-1}\left(\frac{Q_k^{(0)}}{c_k^{(0)}}\right) \tag{E.4}$$

$$h_k^{(0)} = h_{k\infty} = c_{k\infty} \sin\psi_{k\infty} \ln\left[\frac{4}{\gamma_e q c_{k\infty}\left(1 + \cos\psi_{k\infty}\right)}\right] \tag{E.5}$$

(2) **Step two:** Substitution $Q_k = Q_k^{(n)}$ and $c_k = c_k^{(n)}$

$$\begin{aligned} h_k^{(n+1)} &= Q_k^{(n)}\{\tau_k + 2\ln[1 - \exp(-2\tau_k)]\} \\ &\quad - \left(Q_1^{(n)} + Q_2^{(n)}\right)\ln(\gamma_e q a) + \left(Q_1^{(n)} + Q_2^{(n)}\right) x(A - B) \end{aligned} \tag{E.6}$$

$$A = \sum_{n=1}^{\infty} \frac{1}{n} \frac{\sinh n(\tau_1 - \tau_2)}{\sinh n(\tau_1 + \tau_2)} \qquad j, k = 1,2, j \neq k. \tag{E.7}$$

$$B = \sum_{n=1}^{\infty} \frac{2}{n} \frac{\exp(-n\tau_k)\sinh n\tau_j}{\sinh n(\tau_1 + \tau_2)} \qquad j, k = 1,2, j \neq k. \tag{E.8}$$

$$\tau_k = \ln\left(\frac{z}{c_k} + \sqrt{\frac{z^2}{c_k^2} + 1}\right), k = 1,2 \tag{E.9}$$

$$z = \frac{\sqrt{[L^2 - (r_1 + r_2)^2][L^2 - (r_1 - r_2)^2]}}{2L} \tag{E.10}$$

(3) **Step 3:** The next approximation of $Q_k^{(n+1)}$ is obtained from :

$$Q_k^{(n+1)} = Q_k^{(n)} - \frac{1}{2}\left(q c_k^{(n)}\right)^2 \left[h_k^{(n+1)} - h_k^{(n)}\right] \tag{E.11}$$

$$c_k^{(n+1)} = \frac{1}{2}\left[r_k \sin\theta_k + \left(r_k^2 \sin{\theta_k}^2 + 4Q_k^{(n+1)} r_k \cos\theta_k\right)^{\frac{1}{2}}\right] \tag{E.12}$$

$$\psi_k^{(n+1)} = \sin^{-1}\left(\frac{Q_k^{(n+1)}}{c_k^{(n+1)}}\right) \tag{E.13}$$

(4) **Step 4:** Repeat from **Step 2** to give $h_k^{(n+1)}$, until convergency is obtained. Finally, the theoretical capillary force is calculated from **Equation (32)**.

Appendix F. Bubble geometrical parameters

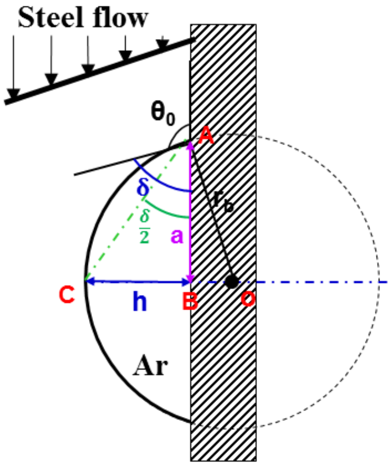

Figure F. 1. Bubble attached to the nozzle wall, parameters.

The bubble attached to the nozzle wall is approximated to a spherical shape, and thus the size of the bubble will be always referred to the equivalent bubble radius, r_b. Two paramenters are calculated here:

(1) The contact radius of the bubble, a, which is given by the following relation:

$$a = r_b \sin\theta_0 = \frac{h}{\tan\left(\frac{\pi - \theta_0}{2}\right)} \qquad \textbf{(F.1)}$$

In addition, by solving the triangle ABC another relation for the contact radius a, is obtained:

$$\tan\left(\frac{\delta}{2}\right) = \frac{h}{a} \rightarrow a = \frac{h}{\tan\left(\frac{\delta}{2}\right)} \qquad \textbf{(F.2)}$$

(2) The height of the bubble, h, is obtained by solving the triangle AOB:

$$r_b^2 = (r_b - h)^2 + a^2 \rightarrow a^2 = 2r_b h - h^2 \qquad \textbf{(F.3)}$$

By substituting **Equation (F.2)** in **(F.3)** the following relation is obtained:

$$\left(\frac{\mathrm{h}}{\tan\left(\frac{\delta}{2}\right)}\right)^2 = 2\mathrm{r_b}\mathrm{h} - \mathrm{h}^2 \rightarrow \mathrm{h} = 2\mathrm{r_b}\left(\tan\left(\frac{\delta}{2}\right)\right)^2 - \left(\tan\left(\frac{\delta}{2}\right)\right)^2 \mathrm{h} \rightarrow \mathbf{h} = \frac{\mathbf{2r_b}\left(\mathbf{tan}\left(\frac{\boldsymbol{\delta}}{\mathbf{2}}\right)\right)^{\mathbf{2}}}{\left[\mathbf{1} + \left(\mathbf{tan}\left(\frac{\boldsymbol{\delta}}{\mathbf{2}}\right)\right)^{2}\right]} \tag{F.4}$$

Now $\delta = \pi - \theta_0$, **Equation (F.5)** gives the height of the bubble:

$$\mathrm{h} = \frac{2\mathrm{r_b}\left(\tan\left(\frac{\pi - \theta_0}{2}\right)\right)^2}{\left[1 + \left(\tan\left(\frac{\pi - \theta_0}{2}\right)\right)^2\right]} = \mathrm{a} \cdot \tan\left(\frac{\pi - \theta_0}{2}\right) \tag{F.5}$$

Appendix G. Surface tension force

The force that acts to keep the bubble attached to the wall has two components as described in **Figure G.1-a)** [89,263]:

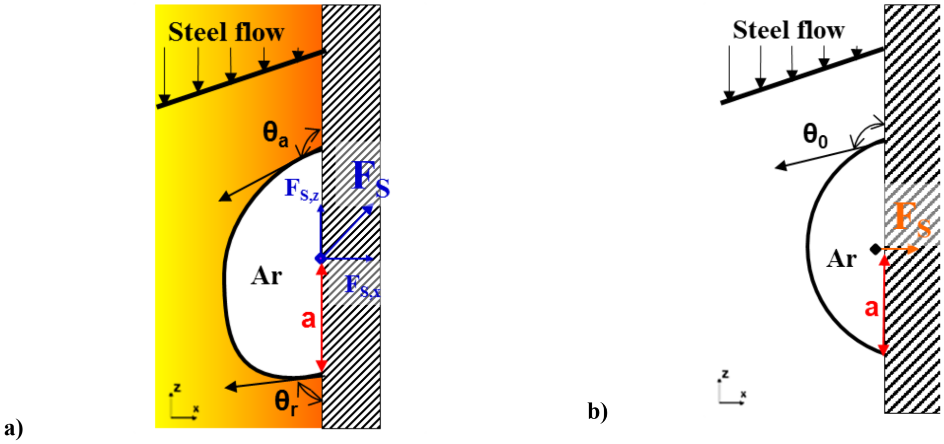

Figure G. 1. a) Surface tension force components in vertical ($F_{s,z}$) and normal directions ($F_{s,x}$), and b) surface tension force in a static bubble at the nozzle wall.

(1) The vertical component, $F_{s,z}$, which acts upward to resist drag of the bubble, makes the bubble to elongate below the gas injection hole, and it is defined as follows

$$F_{S,z} = \frac{\pi}{2}\sigma\, a(\cos\theta_r - \cos\theta_a) \qquad \textbf{(G1)}$$

(2) The normal component, $F_{s,x}$, acts to keep the bubble adhere to the wall

$$F_{S,x} = \frac{\pi}{2}\sigma\, a(\sin\theta_r + \sin\theta_a) \qquad \textbf{(G.273)}$$

For the case of a static bubble, where $\theta_r = \theta_a = \theta_o$, the vertical component is zero and the normal component will be transformed into the following:

$$F_{S,x} = \frac{\pi}{2}\sigma\, a(\sin\theta_o + \sin\theta_o) = \pi a\,\sigma\sin\theta_o \qquad \textbf{(G.3)}$$

Appendix H. Stability of a particle at the fluid interface

For a NMI to be stable at the Ar-molten steel interface layer the capillary pressure in the bubble acting on the contact area should be equal to the capillary pressure, as illustrated in **Figure H.1-a)** and the balance is given in **Equation (H.1)**:

$$F_C - F_P = 0 \rightarrow F_C = F_P \qquad \textbf{(H.1)}$$

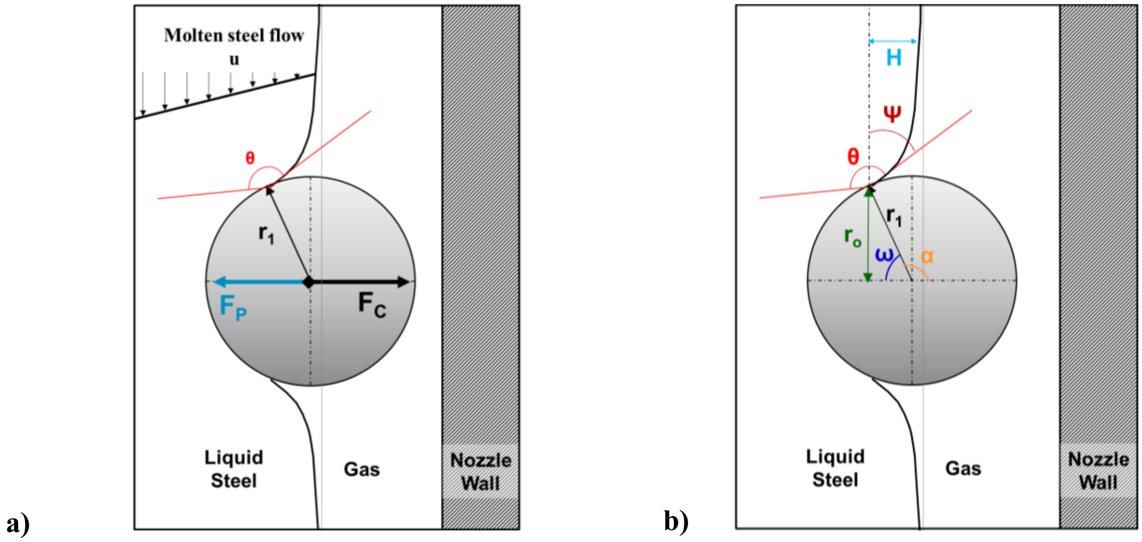

Figure H. 1. a) Stability balance of a NMI at a molten steel/gas bubble interface and **b)** Parameters needed for the stability balance calculation.

The capillary force, given by **equation (H.2)**:

$$F_C = 2\pi r_o \sigma \sin\psi \qquad \textbf{(H.2)}$$

The parameter, r_o, follows the next relation:

$$r_o = r_p \sin\alpha = r_p \sin(\pi - \omega) = r_p \sin\omega \qquad \textbf{(H.3)}$$

Taken into account that $\sin(\pi - \omega) = \sin \pi \cos \omega - \cos \pi \sin \omega = 0 - (-1) \sin \omega = \sin \omega$. The capillary force is given by

$$F_C = 2\pi\left(r_p \sin \omega\right) \cdot \sigma \sin \psi \tag{H.4}$$

Being the meniscus slope at the contact line[269], ψ,

$$\begin{aligned} &\psi = \omega + \theta - \pi \rightarrow \\ &\rightarrow \sin \psi = \sin(\omega + \theta - \pi) = \sin(\omega + \theta) \cos \pi - \cos(\omega + \theta) \sin \pi \\ &= (-1) \sin(\omega + \theta) \end{aligned} \tag{H.5}$$

Now the capillary force, in function of the center-angle, ω:

$$F_C = -2\pi r_p \sigma \sin \omega \sin(\omega + \theta) \tag{H.6}$$

Considering the capillary pressure in the bubble, F_P, acting on the contact area with the force whereby[266,274]

$$F_P = \pi r_1^2 \sin \omega^2 \left[\frac{2\sigma}{r_b} - 2 r_b \rho_S g\right] \tag{H.7}$$

The stability balance[266] is solved to calculate the center-angle when the particle is stable at the fluid interface, ω, is

$$F_C - F_P = 0 \rightarrow F_C = F_P \tag{H.8}$$

$$\begin{aligned} &-2\pi r_1 \sigma \sin \omega \sin(\omega + \theta) = \pi r_1^2 \sin \omega^2 \left[\frac{2\sigma}{r_b} - 2 r_b \rho_S g\right] \rightarrow \\ &\rightarrow -\sigma \cos \theta \sin \omega - \sigma \sin \theta \cos \omega = r_p \sin \omega \left[\frac{\sigma}{r_b} - r_b \rho_l g\right] \rightarrow \\ &\rightarrow -\sigma \sin \theta \cos \omega = \sin \omega \left[\frac{r_p \sigma}{r_b} - r_p r_b \rho_l g + \sigma \cos \theta\right] \rightarrow \\ &\rightarrow \frac{\sin(\omega)}{\cos(\omega)} = \tan \omega = \frac{-\sigma \sin \theta}{\left[\frac{r_p \sigma}{r_b} - r_p r_b \rho_l g + \sigma \cos \theta\right]} \end{aligned} \tag{H.9}$$

$$\omega = \tan^{-1} \frac{-\sigma \sin \theta}{\left[\frac{r_p \sigma}{r_b} - r_p r_b \rho_l g + \sigma \cos \theta\right]} \tag{H.10}$$

References

[1] R. Kiessling, *Non-metallic inclusions in steel*, London, UK **1978**.

[2] L. Zhang and B. G. Thomas, *National Steelmak. Symposium* **2003**, 1.

[3] S. K. Michelic, *Selected aspects of inclusion metallurgy in steelmaking*, Habilitation Thesis University of Leoben **2018**.

[4] T. B. Braun, J. F. Elliott and M. C. Flemings, *Metall. Trans. B* **1979**, *10B*, 171.

[5] L. Zhang, W. Puschkell and B. G. Thomas, *Steelmak. Conf. Proc.* **2002**, *85*, 463.

[6] S. K. Michelic, U. Dieguez-Salgado and C. Bernhard, *LMPC Conf. Proc.* **2015**, 1.

[7] S. Seetharaman, Fundamentals of metallurgy, CRC Press, New York **2005**.

[8] V. Vermeulen, B. Coletti, B. Blanpain, P. Wollants and J. Vleugels, *ISIJ. Int*. **2002**, *42*, 1234

[9] K. G. Rackers and B. G. Thomas, Iron and Steel Society, Warrendale, PA 1995, 78,723.

[10] M. Nadif, M. Burty, H. Soulard, M. Boher, C. Pusse, J. Lehmann and F. Meyer, IISI Study on Clean Steel, 1st Ed., IRSID Arcelor France **2004**.

[11] F. G. Wilson, M. J. Heeson and J. D. W. Rawson, *Technical Steel Research Final report* **1988**.

[12] S. N. Singh, *Metall.Trans.* **1974**, *5*, 2165.

[13] S. Ogibayashi, *Taikabutsu Overseas* **1995**, *15*, 3.

[14] J. Park, I. Jung and H. Lee, *ISIJ Int.* **2006**, *48*, 1626.

[15] B. F. Thomas and H. Bai, *Iron and Steel Society* **2001**, *18*, 895.

[16] E. S. Szekeres, *Int. Conf. on Clean Steel* **1992**.

[17] Y. K. Shin, I. R. Lee, D. S. Kim, S. K. Kim and K. S. Oh, *Ironmak. & Steelmak.* **1988**, *15*, 143.

[18] E. Roos, A. Karasev and P. G. Jönsson, *Steel Research Int.* **2015**, *86*, 1279.

[19] J. Poirier, B. Thillou, M. A. Guiban and G. Provost, *Steelmak. Conf. Proc.* **1995**, 451

[20] R. Tuttle, K. D. Peaslee and J. D. Smith, *AISTech Conf. Proc.* **2002**, 1.

[21] M. Suzuki, Y. Yamaoka, N. Kubo and M. Suzuki, *ISIJ Int.* **2002**, *42*, 248.

[22] S. Dawson, *Ironmak. & Steelmak.* **1990**, *17*, 33.

[23] H. Bai and B. G. Thomas, *Metall. Mater. Trans. B* **2001**, *32*, 707.

[24] H. Bai and B. G. Thomas, *Steelmak. Conf. Proc.* **2000**, 183.

[25] K. G. Rackers, *Mechanism and Mitigation of Clogging in continuous Casting nozzles. Master Thesis University of Illinois* **1995**.

[26] K. Sasai and Y. Mizukami, *ISIJ Int.* **1995**, *35*, 26.

[27] Y. Fukuda, Y. Ueshima and S. Mizoguchi, *ISIJ Int.* **1992**, *32*, 164.

[28] S. Ramachandran, K. D. Peaslee and J. D. Smith, *Steelmak. Conf. Proc.* **2001**,729.

[29] N. Kasai, M. Kawasaki, Y. Hayashi and H. Kawai, *Taikabutsu Overseas* **1991**, *11*, 22.

[30] H. Shikano, T. Harada, S. Iitisuka and K. Shin-Ichirou, *Taikabutsu Overseas* **1991**, *11*, 10.

[31] L. Zhang, *J. Iron and Steel Research Int.* **2006**, *13*, 1.

[32] S. Liu, S. Niu, M. Liang, C. Li, X. Zuo, L. Zhang and X. Wang, *AISTech Conf. Proc.* **2007**, *10*, 1.

[33] G. T. Moulden and R. Sabol, *Steelmak. Conf. Proc.* **2000**, 161

[34] V. Brabie, *ISIJ Int.* **1996**, *36*, 109.

[35] W. Höller, *Veitsch-Radex Rundschau* **1998**, *2*, 13.

[36] M. Nakamura, T. Yamamura, O. Nomura, R. Nakamura and E. Iida, *Taikabutsu Overseas* **1997**, *17*, 34.

[37] J. Lee, S. Kim, M. Kang and Y. Kang Y, *ECCC Conf. Proc.* **2017**, 1.

[38] J. Poirier, D. Verrelle, B. Thillou, G. Provost, C. Taffin and P. Tssot, *Unitecr conf. Proc.* **1991**, 226.

[39] J. Szekely and S. T. Dinovo, *Metall. Trans.* **1974**, *5*, 747.

[40] G. C. Duderstadt, R. K. Iyengar and J. M. Matesa, *J. Metals* **1968**, *4*, 89.

[41] J. W. Farrell and D. C. Hilty, *Electric Furnace Conf. Proc.* **1971**, 31.

[42] M. Andersson and O. Wijk, *Int. Conf. Refining Processes* **1992**, 175.

[43] K. Sasai and Y. Mizukami, *ISIJ Int.* **2001**, *41*, 1331.

[44] K. Uemura, M. Takahashi, S. Koyama and M. Nitta, *ISIJ Int.* **1992**, *32*, 150.

[45] E. Kawecka-Cebula, Z. Kalicka and J. Wypartowicz, *Arch. Metall. and Mater.* **2006**, *51*, 261.

[46] C. G. Aneziris, C. Schroeder, M. Emmel, G. Schmidt, H. P. Heller and H. Berek, *Metall. Mater.Trans. B* **2013**, *44B*, 954.

[47] K. Sasai, *ISIJ Int.* **2014**, *54*, 2780.

[48] T. Mizoguchi, Y. Ueshima, M. Sugiyama and K. Mizukami, *ISIJ Int.* **2013**, *53*, 639.

[49] Y. Ueshima, T. Mizoguchi, M. Sugiyama and K. Mizukami, *ICS Conf. Proc.* **2012**, 1.

[50] L. Zheng, A. Malfliet, P. Wollants, B. Blanpain and M. Guo, *ICS Conf. Proc.* **2015**, 731.

[51] L. Zheng, A. Malfliet, P. Wollants, B. Blanpain and M. Guo, *ISIJ Int.* **2016**, *56*, 926.

[52] C. Xuan, A. V. Karasev, P. G. Jönsson and K. Nakajima, *Steel Research Int.* **2017**, *88*, 911.

[53] G. Hassal and K. Mills, *Technical Steel Research Final report* **1990**.

[54] A. W. Cramb and I. Jimbo, *W. O. Philbrook Memorial Symp. Conf. proc.* **1988**, 259.

[55] C. Tian. *On the Removal of Non-Metallic Inclusions from Molten Steel through Filtration*, Ph.D. Thesis McGill University **1990**.

[56] J. Wikström, K. Nakajima, H. Shibata, A. Tilliander and P. Jönsson, *Ironmak. &Steelmak.* **2008**, *35*, 589.

[57] J. Hartmüller and S. Ripperger, *Filtrieren & Separieren* **2014**, *28*, 274.

[58] G. Lian, C. Thornton and M. J. Adams, *J. Colloid and Interface Sci.* **1993**, *161*, 138.

[59] R. A. Fisher, *J. Agri. Sci.* **1926**, 1.

[60] D. Rossetti and S. J. R. Simons, *Powder Technol.* **2003**, *130*, 49.

[61] A. Gladkyy and R. Schwarze, *Granular Matter.* **2014**, *16*, 911.

[62] H. P. Zhu, Z. Y. Zhou, R. Y. Yang and A. B. Yu, *Chem. Eng. Sci.* **2007**, *62*, 3378.

[63] M. A. Fortes, *Can. J. Chem.* **1982**, *60*, 2889.

[64] L. Zheng, A. Malfliet, P.Wollants, B. Blanpain and M. Guo, *ISIJ Int.* **2015**, *55*, 1891.

[65] J. N. Israelachvili, *Intermolecular and Surface Forces*, 2nd. Ed., Academic Press, New York **2011**.

[66] R. Clift, J. R. Grace and M. E. Weber, *Blubbles, drops and particles.* Academic press, New York **1978**.

[67] J. W. Cleaver and B. Yates, *J. Colloid Interface Sci.* **1973**, *44*, 464.

[68] R. J. Garde and K. G. Ranga Raju, *3rd Ed.,Taylor & Francis* **2000**.

[69] D. Leighton and A. Acrivos, *Z. angew. Math. Phys.* **1985**, *36*, 174.

[70] T. Hibiki and M. Ishii, *Chem. Eng. Sci.* **2007**, *62*, 6457.

[71] P. M. Benson, Q. K. Robinson and H. K. Part, *Steelmaking Conf. Proc.* **1993**, 533.

[72] E. Lührsen, A. Ott, W. Porbel, J. Piret, R. Ruddlestone and B. Short, *ECCC Conf. Proc.* **1991**, 137.

[73] A. R. McKague, R. Enger, M. A. Suer, D. J. Wolf, M. D. Garbowsky and L. E. Reed, *Iron and Steelmaker* **1998**, *25*.

[74] J. J. Vitlip and J. E. Roush, *Steelmaking Conf. Proc.* **2001**, 33.

[75] C. E. Cicutti, J. Madías and J. C. González, *Ironmak. & Steelmak.* **1997**, *24*, 155.

[76] C. Cicutti, M. Valdez, T. Pérez, R. Ares, R. Panelli and J. Petroni, *Steelmak. Conf. Proc.* **2001**, 871.

[77] N. Bannenber, *Steelmaking Conf. Proc.* **1995**, 457.

[78] G. M. Faulring, J. W. Farrell and D. C. Hilty, *Continuous casting Conf. Proc.* **1995**, *1*, 57.

[79] M. K. Sardar, S. Mukhopadhyay, U. K. Bandopadhyay and S. K. Dhua, *Steel Research* **2007**, *78*, 136.

[80] R. Heinke and K. Takahama, *Steel Research* **1987**, *58*.

[81] D. Janke, Z. Ma, P. Valentin and A. Heinen, *ISIJ Int.* **2000**, *40*, 31.

[82] G. Chen, S. He, Y. Guo, B. Shen, S. Zhao and Q. Wang, *J. Iron and Steel Research Int.* **2015**, *22*, 590.

[83] Y. Ren, L. Zhang and S. Li, *ISIJ Int.* **2014**, *54*, 2772.

[84] G. Yang and X. Wang, *ISIJ Int.* **2015**, *55*, 126.

[85] J. Yang, X. Wang, M. Jiang and W. Wang, *J. Iron and Steel Research Int.* **2011**, *18*, 8.

[86] D. Yang, X. Wang, G. Yang, P. Wei and J. He, *Steel Research Int.* **2014**, *85*, 1517.

[87] M. Alavanja, R. T. Gass, R. W. Kittridge and H. T. Tsai, *Steelmak. Conf. Proc.* **1995**, 415.

[88] B. G. Thomas, A. Dennisov and H. Bai, *ISS Steelmak. Conf.* **1997**, 375.

[89] H. Bai, *Argon bubble behavior in slide-gate tundish nozzles during continuous casting of steel slabs. Ph.D. Thesis University of Illinois (USA)* **2000**.

[90] N. Tsukamoto, Y. Kurashina and K. Yanagawa, *Taikabutsu Overseas* **1995**, *15*, 43.

[91] O. P. Cure, *Patent number: 4,850,572 U.S.* **1989**.

[92] T. Kawamura, S. Niwa, E. Hasebe and T. Simoda, *Unitcer Conf. Proc.* **1993**, 1107.

[93] S. Yokoya, S. Takagi, H. Souma, M. Iguchi, Y. Asako and S. Hara, *ISIJ Int.* **1998**, *38*, 1086.

[94] G. Hackl, G. Nitzl, D. Warrington, A. Westendorp and R. Bogert, *ECCC Conf. Proc.* **2011**, 1.

[95] S. Kobayashi, T. Ishige and M. Igata, *Taikabutsu Overseas* **1995**, *15*, 33.

[96] Y. Sahai and T. Emi, *Tundish Technology for Clean Steel Production*, World Scientific **2008**.

[97] R. Tsujino, A. Tanaka, A. Imamura, D. Takahashi and S. Mizoguchi, *ISIJ Int.* **1994**, *34*, 853.

[98] T. Nakamura, T. Aoki, H. Okumura and Y. Kondo, *Taikabutsu Overseas* **1991**, *11*, 38.

[99] F. Ohno, T. Muroi and K. Oguri, *J. Tech. Assoc. Refract.* **2002**, *22*, 63.

[100] K. Oguri, M. Ando, T. Muroi, T. Aoki and H. Okumura, *Unitecr* **1993**, 1119.

[101] T. Aoki, T. Nakamura, H. Ozeki and A. Elksnitis, *Steelmak. Conf. Proc.* **1991**, 357.

[102] W. Zhong, W. Li and X. Zhong, *Adv. in Refractories for the Metall. Ind. II* **1996**, 441.

[103] R. B. Tuttle, *Innovative refractories for preventing nozzle clogging in continuous cast aluminium-killed steels. Ph.D. Thesis University of Missouri at Rolla*, USA **2004**.

[104] O. Araromi, B. G. Thomas and E. Conzemius, *Mater. Sci. Techn. Conf.* **2009**, 1.

[105] Q. K. Robinson, H. K. Park, C. Dumazeau and T. Louchart, *Trans. Indian Ceramic Soc.* **1993**, *52*, 129.

[106] J. Poirier, *Metall. Res. Technol.* **2015**, *112*, 410.

[107] A. Memarpour, V. Brabie and P. Jönsson, *Ironmak. & Steelmak.* **2011**, *38*, 229.

[108] K. Goto, K. Kohno, T. Ikemoto, S. Hanagiri and T. Matsui, *Nippon Steel Technical report* **2013**, *104*.

[109] M. Nakamura, T. Kiwada, O. Nomura and K. Ichikawa, *Taikabutsu Overseas* **1995**, *15*, 28.

[110] T. Vert, *Chapter 10, in Refractory Material Selection for Steelmaking*, John Wiley & Sons, Inc., Hoboken, NJ, USA **2016**

[111] *ISO products*, https://www.rhimagnesita.com/solutions-services/casting/.

[112] N. Eustathopoulos and B. Drevet, *J. Phys. III* **1994**, *4*, 1985.

[113] G. Hackl, G. Nitzl, Y. Tang, C. Eglsäer and D. Chalmers, *AISTech Conf. Proc.* **2015**, 2436.

[114] X. Zheng, P. C. Hayes and H. Lee, *ISIJ Int.* **1997**, *37*, 1091.

[115] D. S. Kumar, T. Rajendra, R. Prasad, A. Sarkar and M. Ranjan, *Ironmak. & Steelmak.* **2013**, *36*, 470.

[116] Z. Meijie, G. Huazhi, H. Ao, Z. Hongxi and D. Chengji, *J. min. metall. Sect B-Metall.* **2011**, *47*, 137.

[117] H. W. Pielet and D. Bhattacharya, *Met. Trans. B* **1984**, *15*, 547.

[118] W. Fix, H. Jacobi and K. Wünnenberg, *Steel Research* **1993**, *64*, 71.

[119] Y. Hiraga, Y. Yashima and K. Fujii, *Taikabutsu Overseas* **1995**, *15*.

[120] A. Hamoen and W. Tiekink, *Steelmaking Conf. Proc.* **1998**, 229.

[121] R. Maddalena, R. Rastogi and A. W. Cramb, *Electric Furnace Conf. Proc.* **2000**, 811

[122] Y. Vermeulen, B. Coletti, P. Wollants, B. Blanpain and F. Haers, *Steel Research* **2000**, *71*, 391.

[123] R. Rastogi and A. W. Cramb, *Steelmak. Conf. Proc.* **2001**, 789.

[124] R. Dekkers, B. Blanpain, P. Wollants, F. Haers, B. Gommers and C. Vercruyssen, *Steel Research* **2003**, *74*.

[125] S. Basu, S. K. Choudhary and N. U. Girase, *ISIJ Int.* **2004**, *44*, 1653.

[126] S. Liu, X. Wang, X. Zuo, Y. Wang, L. Zhang, S. Niu, M. Liang and C. Li, *Rev. Met. Paris* **2008**, *105*, 72.

[127] H. Cui, Y.Bao, M. Wang and W. Wu, *Int J Miner Metall Mater* **2010**, *17*, 154.

[128] C. Bernhard, G. Xia, M. Egger, A. Pissenberger and S. Michelic, *AISTech Conf. Proc.* **2012**, 2191.

[129] A. Memarpour, V. Bravie and P. G. Jönsson, *Metec InSteel Conf. Proc.* **2011**, 1.

[130] E. Zinngrebe, C. van Hoek, H. Visser, A. Westendorp and I. Jung, *ISIJ Int.* **2012**, *52*, 52.

[131] J. Xu, F. Huang, X. Wang, C. Jing and X. Guo, *Ironmak. & Steelmak.* **2016**, *44*, 455.

[132] P. Dorrer, S. K. Michelic, G. Kloesch, J. Reiter, A. Paul and C. Bernhard, *AISTech Conf. Proc.* **2017**, 1555.

[133] C. Wang, N. T. Nuhfer and S. Sridhar, *Metall. Mater. Trans. B* **2010**, *41*, 1084.

[134] M. Sun, I Jung and H. Lee, *Metals and Mater. Int.* **2008**, *14*, 791.

[135] C. Wang, H. Matsuura, N. Kikuchi, G. Wen and S. Sridhart, *Rev. Met. Paris* **2008**, *105*, 22.

[136] P. Kaushik, D. Kruse and M. Ozgu, *Rev. Met. Paris* **2008**, *105*, 92.

[137] H. Matsuura, C. Wang, G. Wen and S. Sridhar, *ISIJ Int.* **2007**, *47*, 1265.

[138] T. Zhang, C. Liu, H. Mu, Y. Li, Y and M. Jiang, *Ironmak. & Steelmak.* **2017**, *83*, 1.

[139] D. Janis, A. Karasev, R. Inoue and P. G. Jönsson, *Steel Research Int.* **2015**, *86*, 1271.

[140] L. Trueba, K. D. Peaslee and J. D. Smith, *Steelmak. Conf. Proc.* **2001**, 913.

[141] K. Schwerdtfeger and H. Schrewe, *Electric Furnace Conf. Proc.* **1970**, *28*, 95.

[142] J. K. S. Svensson, A. Memarpour, S. Ekerot, V. Brabie and P. G. Jönsson, *Ironmak. & Steelmak.* **2017**, *44*, 117.

[143] R. B. Tuttle, J. D. Smith and K. D. Peaslee, *Metall. Mater. Trans B* **2007**, *38*, 101.

[144] P. R. Scheller and S. Lachmann, *Unitecr conf. Proc.* **2007**, 334.

[145] H. Yin, H. Shibate, T. Emi and M. Suzuki, *ISIJ Int.* **1997**, *37*, 946.

[146] H. Yin, H. Shibata, T. Emi and M. Suzuki, *ISIJ Int.* **1997**, *37*, 936.

[147] U. Diéguez-Salgado, S. Michelic and C. Bernhard, *Mater. Sci. Eng.* **2016**, *119*, 12003.

[148] C. G. Aneziris, C. Schroeder, U. Fischer, H. Berek, M. Emmel, J. Kortus, L. G. Amirkhanyan and T. Weißbach, *Adv. Eng. Mater.* **2013**, *15*, 1168.

[149] T. Emi, H. Shibata and H. Yin, *Belton Symposium Proc.* **2000**, 195

[150] S. Kimura, Y. Nabeshima, K. Nakajima and S. Mizoguchi, *Metall. Mater. Trans. B* **2000**, *31*, 1013.

[151] S. Kimura, K. Nakajima, S. Mizoguchi and H. Hasegawa, *Metall. Trans. A* **2002**, *33*, 427.

[152] H. Luo, *Scandinavian J. Metall.* **2001**, 212.

[153] K. Nakajima and S. Mizoguchi, *Metall. Mater. Trans. B* **2001**, *32B*, 629.

[154] B. Coletti, S. Vantilt, B. Blanpain and S. Sridhar, *Metall. Mater. Trans. B* **2003**, *34 B*, 533.

[155] S. Vantilt, B. Coletti, B. Blanpain, J. Fransaer, P. Wollants and S. Sridhar, *ISIJ Int.* **2004**, *44*, 1.

[156] M. Jiang, X. Wang, H. Yu J. Pak and P. Yuan, *ICS Conf. Proc.* **2015**, 789.

[157] G. Du, J. Li, Z. Wang and C. Shi, *Steel Research Int.* **2017**, *88*, 1600185.

[158] W. Mu, N. Dogan and K. S. Coley, *Metall. and Mater. Trans. B* **2017**, *48*, 2092.

[159] W. Mu, N. Dogan and K. S. Coley, *Metall. Mater. Trans. B* **2017**, *48*, 2379.

[160] S. K. Michelic and C. Bernhard, *Scanning* **2017**, *2017*, 1.

[161] Y. Kang, B. Sahebkar, P. R. Scheller, K. Morita and D. Sichen, *Metall. Mater. Trans. B* **2011**, *42*, 522.

[162] Y. Kang, B. Sahebkar, P. R. Scheller and D. Sichen, *Conf. Proc.* **2010**, 265.

[163] S. Feichtinger, S. K. Michelic, Y. Kang, C. Bernhard and C. Jantzen, *J. Am. Ceram. Soc.* **2014**, *97*, 316.

[164] S. Michelic, J. Goriupp, S. Feichtinger, Y. Kang, C. Bernhard and J. Schenk, *Steel Research Int.* **2015**, *86*, 1.

[165] J. Liu, M. Guo, P. T. Jones, F. Verhaeghe, B. Blanpain and P. Wollants, *J. European Ceramic Soc.* **2007**, *27*, 1961.

[166] J. Liu, L. Zhu, M. Guo, F. Verhaeghe, B. Blanpain and P. Wollants, *Rev. Met. Paris* **2008**, *105*, 255.

[167] J. Goriupp, J. Schenk, G. Klösch and A. Paul, *BHM* **2016**, *161*, 102.

[168] Z. Liu, Y. Kobayashi, J. Yang, K. Nagai and M. Kuwabara, *ISIJ Int.* **2006**, *46*, 847.

[169] X. Guo, Z. H. I. Sun, J. van Dyck, M. Guo and B. Blanpain, *Ind. Eng. Chem. Res.* **2014**, *53*, 6325.

[170] J. Liu, F. Verhaeghe, M. Guo, B. Blanpain and P. Wollants, *J. American Ceramic Soc.* **2007**, *90*, 3818.

[171] Z. H. I. Sun, X. Guo, J. van Dyck, M. Guo and B. Blanpain, *AIChE J.* **2013**, *59*, 2907.

[172] R. B. Tuttle, J. D. Smith and K. D. Peaslee, *Metall. Mater. Trans. B* **2005**, *36*, 885.

[173] Y. M. K. Sasai, *ISIJ Int.* **1994**, *34*, 802.

[174] N. Yamauchi, K. Yamaguchi and S. Takahashi, *ICS Conf. Proc.* **2005**, 149.

[175] A. Memarpour, V. Brabie and P. Jönsson, *Ironmak. & Steelmak.* **2013**, *38*, 229.

[176] X. Zhang, X. Jin, Y. Wang, K. Deng, and Z. Ren, *ISIJ Int.* **2011**, *51*, 581.

[177] X. Zuo, M. Long, J. Gao, Y. Wang and L. Zhang, *Iron & Steel Tech.* **2010**, 65.

[178] L. Zhang, Y. Wang and X. Zuo, *Metall. Mater. Trans. B* **2008**, *39*, 534.

[179] S. Kao, H. Kua, O. Wiens, W. Moßner, M. Reifferscheid, N. Vogl, G. Hackl and G. Nitzl, *Metec InSteel Conf. Proc.* **2011**, 1.

[180] H. Yu, G. Zhu, X. Wang, J. Zhang and W. Wang, *J. Univ. Sci. Technol. Beijing* **2005**, *12*, 303.

[181] R. Sambasivam, *Ironmak. & Steelmak.* **2006**, *33*, 439.

[182] B. G. Thomas, Q. Yuan. S. Sivaramakrishnan and S. P. Vanka, *JOM* **2003**, 1.

[183] E. Gutiérrez, S. Garcia-Hernandez and J. Jesús-Barreto, *Steel Research Int.* **2016**, *87*, 1406.

[184] B. G. Thomas, Q. Yuan, S. Mahmood, R. Liu and R. Chaudhary, *Metall. Mater. Trans. B* **2014**, *45*, 22.

[185] Y. Ren and L. Zhang, *Ironmak. & Steelmak.* **2017**, *28*, 1.

[186] C. Bernhard, S. Schider, A. Sormann, G. Xia and S. Ilie, *BHM* **2011**, *156*, 161.

[187] N. Fuchs, P. Krajewski and C. Bernhard, *BHM* **2015**, *160*, 214.

[188] S. Griesser, *In-situ study of the influence of alloying elements on the kinetics and mechanism of the peritecti phase transition in steel, Ph. D. Thesis University of Wollongong (Australia)* **2013**.

[189] S. Griesser. R. Pierer. M. Reid and R. Dippenaar, *J. Microscopy* **2012**, *248*, 42.

[190] N. McDonald and S. Sridhar, *MEKU* **2005**, *96*, 304.

[191] N. J. McDonald and S. Sridhar, *Electric Furnace Conf. Proc.* **2002**, 353.

[192] N. J. McDonald and S. Sridhar, *Metall. Mater. Trans. B* **2003**, *34*, 1931.

[193] H. Nassar and H. Fredriksson, *Metall. Mater. Trans. A* **2010**, *41*, 2776.

[194] D. Phelan, M. Reid and R. Dippenaar, *Mater. Sci. Eng. A* **2008**, *477*, 226.

[195] D. Phelan, M. H. Reid and R. J. Dippenaar, *MAM* **2005**, *11*.

[196] R. Dippenaar, *ICS Conf. Proc.* **2012**,1 .

[197] H. Shibata, Y. Arai, M. Suzuki and T. Emi, *Metall. Mater. Trans. B* **2000**, *31*, 981.

[198] N. J. McDonald and S. Sridhar, *TMS* **2003**, 381.

[199] H. Chen, M. Long, J. Cao, D. Chen, T. Liu and Z. Dong, *Metals* **2017**, *7*, 288.

[200] D. Loder, S. K. Michelic and C. Bernhard, *MS&T Conf. Proc.* **2014**, 1.

[201] D. Loder, S. K. Michelic, A. Mayerhofer, C. Bernhard and R. J. Dippenaar, *Junior Euromat Conf. Proc.* **2014**, 1.

[202] D. Loder, S. K. Michelic, A. Mayerhofer and C. Bernhard, *Metall. Mater. Trans B* **2017**, *48*, 1992.

[203] X. Wan, K. Wu, G. Huang and R. Wei, *Steel Research Int.* **2014**, *85*, 243.

[204] X. Wan, K. Wu, L. Cheng and R. Wei, *ISIJ Int.* **2015**, *55*, 679.

[205] X. K. Wan, K. M. Wu, K. C. Nune, Y. Li and L. Cheng, *Sci. Technol. Welding and Joining* **2015**, *20*, 254.

[206] D. Zhang, T. Hidenori and Y. Komizo, *Acta Materialia* **2010**, *58*, 1369.

[207] B. Wen and B. Song, *J. for Manuf. Sci. Prod.* **2013**, *13*, 61.

[208] B. Wen and B. Song, *Steel Research Int.* **2012**, *83*, 487.

[209] C. Yang, M. Jiang, X. Wang and T. Ou, *Adv. Mater. Rerserach* **2012**, 620.

[210] Z. Adabavazeh, W. S. Hwang and Y. H. Su, *Scientific reports* **2017**, *7*, 1.

[211] C. Lin, Y. Pan, W. Hwang, Y. Fang, Y. Su, G. Lin and Y. Wu, *Ironmak. & Steelmak.* **2017**, *48*, 1.

[212] X. F. Zhang, P. Han, H. Terasaki. M. Sato and Y. Komizo, *J. Mater. Sci. Technol.* **2012**, *28*, 241.

[213] M. Enomoto and X. L. Wan, *Metall. Mater. Trans. A* **2017**, *48*, 1572.

[214] N. Yan, S. Yu and Y. Chen, *J. Rare Earths* **2017**, *35*, 203.

[215] X. Wan, K. Wu, G. Huang, R. Wei and L. Cheng, *Int. J. Miner. Metall. Mater.* **2014**, *21*, 878.

[216] F. Liu, G. Xu, Y. Zhang, H. Hu, L. Zhou and Z. Xue, *Int. J. Miner. Metall. Mater.* **2013**, *20*, 1060.

[217] Y. Komizo, H. Terasaki, M. Yonemura and T. Osuki, *Welding in the World- Research Suplement* **2013**.

[218] Y. Li, G. Wen. L. Luo, J. Liu and P. Tang, *Ironmak. & Steelmak.* **2015**, *42*, 41.

[219] X. Li, T. Zhang, T. Min, Y. Liu, C. Liu and M. Jiang, *Ironmak. & Steelmak.* **2017**, *23*, 1.

[220] X. F. Zhang, H. Terasaki and Y. Komizo, *Philosophical Magazine Letters* **2011**, *91*, 491.

[221] S. Zhang, S. Morito and Y. Komizo, *ISIJ Int.* **2012**, *52*, 510.

[221] D. Zhang, Y. Shintaku, S. Suzuki and Y. Komizo, *Metall. Mat. Trans. A* **2012**, *43*, 447.

[223] Y. Komizo, *Trans. JWRI* **2011**, *40*, 7.

[224] H. Chikama, H. Shibata, T. Emi and M. Suzuki, *Mater. trans. JIM* **1996**, *37*.

[225] H. Yin, T. Emi and H. Shibata, *ISIJ Int.* **1998**, *38*, 794.

[226] H. Yin, T. Emi and H. Shibata, *Acta Materialia* **1999**, *47*, 1523.

[227] S. Clark, V. Janik, A. Rijkenberg and S. Sridhar, *Materials Characterization* **2016**, *115*, 83.

[228] D. M. Benati, K. Ito, K. Kohama, H. Yamamoto and E. J Zoqui, *Metall. Mater. Trans. B* **2017**, *48*, 2293.

[229] D. Phelan and R. Dippenaar, *ISIJ Int.* **2004**, *44*, 414.

[230] G. Jin, S. Chen, Q. Li, G. Chang and X. Yue, *J. Iron and Steel Research Int.* **2013**, *20*, 94.

[231] J. Hamada, M. Enomoto, T. Fujishiro and T. Akatsuka, *Metall. Mater. Trans. A* **2014**, *45*, 3781.

[232] J. Yan, W. Zhang and A. Borgenstam, *Metall. Mater. Trans. A* **2013**, *44*, 4143.

[233] S. Li, Y. Kang, G. Zhu and S. Kuang, *J. Cent. South Univ.* **2015**, *22*, 1203.

[234] S. Wu, G. Sun and Q. Ma, *J. Wuhan Univ. Technol.-Mat. Sci. Edit.* **2015**, *30*, 152.

[235] W. Mu, H. Shibata, P. Hedström, P. G. Jönsson and K. Nakajima, *Steel Research Int.* **2016**, *87*, 10.

[236] W. Mu, H. Shibata, P. Hedström, P. G. Jönsson and K. Nakajima, *Metall. Mater. Trans. B* **2016**, *47*, 2133.

[237] X. F. Zhang and Y. Komizo, *Mater. Sci. and Technol.* **2013**, *29*, 631.

[238] Y. Zhao, Y. Sun, X. Li and F. Song, *ISIJ Int.* **2017**, *57*, 1637.

[239] Z. Hu, G. Xu, H. Hu, L. Wang and Z. Xue, *Int. J. Miner. Metall. Mater.* **2014**, *21*, 371.

[240] J. H. Park, J. G. Park, D. J. Min, Y. E. Lee and Y. Kang, *J. European Ceramic Soc.* **2010**, *30*, 3181.

[241] P. Yan, M. Guo and B. Blanpain, *Metall. Mater. Trans. B* **2014**, *45*, 903.

[242] P. Yan, *Formation and behaviour of Mn-containing oxysulphide inclusions during desulphurisation, deoxidation and alloying*, Ph.D. Thesis University of Leuven (Belgium) **2014**.

[243] J. Appelberg, K. Nakajima, H. Shibata, A. Tilliander and P. Jönsson, *Mater. Sci. Eng. A* **2008**, *495*, 330.

[244] H. Yin, H. Shibate, T. Emi and M. Suzuki, *ISIJ Int.* **1997**, *37*, 936.

[245] H. Yin, H. Shibata, T. Emi and J. S. Kim, *Proc. Int. Conf. High Temperature Capillarity* **1997**.

[246] Y. Kang, *Some aspects of non-metallic inclusions during vacuum degassing in ladle treatment- with emphasize on liquid CaO-Al2O3 inclusions.* Ph.D. Thesis Royal Institute Technology (Sweeden) **2007**.

[247] S. Kimura, K. Nakajima and S. Mizoguchi, *Metall. Mater. Trans. B* **2001**, *32*, 79.

[248] D. Y. C. Chan, J. D. Henry and L. R. White, *J. Colloid Interface Sci.* **1981**, *79*, 410.

[249] P. A. Kralchevsky, V. N. Paunov, N. D. Denkov, I. B. Ivanov and K. Nagayama, *J. Colloid and Interface Sci.* **1993**, *155*, 420.

[250] V. N. Paunov, P. A. Kralchevsky, N. D. Denkov, I. B. Ivanov and K. Nagayama, *Colloids and Surfaces* **1992**, *67*, 119.

[251] V. N. Paunov, P. A. Kralchevsky, N. D. Denkov and K. Nagayama, *J. Colloid and Interface Sci.* **1993**, *157*, 100.

[252] P. A. Kralchevsky, V. N. Paunov, I. B. Ivanov and K. Nagayama, *J. Colloid and Interface Sci.* **1992**, *151*, 79.

[253] M. M. Nicolson, *Proc. Cambridge Philos. Soc.* **1949**, *45*, 288.

[254] D. Munz and T. Fett T, *Ceramics: mechanical properties, failure behaviour materials selection*, Springer Science & Business Media **2013**.

[255] A. Karasangabo and C. Bernhard, *J. Adhesion Sci. and Technol.* **2012**, *26*, 1141.

[256] L. Shi and D. J. Bayless, *Powder Technol.* **2007**, *173*, 29.

[257] M. Andersson, *Some aspects of oxygen and sulphur reactions towards clean steel production. PhD Thesis Royal Institute Technology (Sweeden)* **2000**.

[258] R. Dekkers, *Non-Metallic Inclusions in Liquid Steel. Ph.D. Thesis University of Leuven (Belgium)* **2002**.

[259] C. Toulouse, A. Pack, A. Ender and S. Petry, *ECCC Conf. Proc.* **2011**, 1.

[260] K. Asano, A. Ishii and K. Kasai, *Unitecr conf. Proc.* **1991**, 229.

[261] L. Luyckx and S. Robinson, *McLean Symp. Proc.* **1998**, 111.

[262] K. Ogino, S. Hara, T. Miwa and S. Kimoto, *Trans. ISIJ* **1984**, *24*, 522.

[263] R. H. S. Winterton, *Chem. Eng. Sci.* **1972**, *27*, 1223.

[264] V. A. Lubarda and K. A.Talke, *J. Surfaces Colloids* **2011**, *27*, 10705.

[265] E. Loth, *Powder Technology* **2008**, *182*, 342.

[266] H. J. Schulze, *Int. J. Mineral Processing* **1977**, *4*, 241.

[267] J. Ralston, D. Fornasiero and R. Hayes, *Int. J. Mineral Procesing* **1999**, *56*, 133.

[268] P. Stevenson, S. Ata and G. M. Evans, *Ind. Eng. Chem. Res.* **2009**, *48*, 8024.

[269] C. F. Gontijo, D. Fornasiero and J. Ralston, *Can. J. Chem. Eng.* **2007**, *85*, 739.

[270] U. Dieguez Salgado, C. Weiss, S. K. Michelic and C. Bernhard, *Metall. Mater. Trans B* **2018**, *Published online*.

[271] P. Kozakevitch and M. Olette, *Rev. Met. Paris* **1971**, *68*, 635.

[272] P. Kozakevitch and L. D. Lucas, *Rev. Met. Paris* **1968**, *65*, 589.

[273] C. Gögelein, M. Brinkmann, M. Schröter and S. Herminghaus, *J. surfaces colloids* **2010**, *26*, 17184.

[274] T. Miettinen, J. Ralston and D. Fornasiero, *Minerals Eng.* **2010**, *23*, 420.

Abbreviations

NMI(s)	Non-metallic inclusion(s)
SEN(s)	Submerged Entry Nozzle(s)
HT-LSCM	High-Temperature Laser Scanning Confocal Microscopy
Al-killed steel	Aluminium killed steel
Ca-treatment	Calcium treatment
T	Transport
A	Adhesion
S	Sintering
A	Al_2O_3
Z	ZrO_2
M	MgO
CA	$CaO \cdot Al_2O_3$
HT-DSA	High-Temperature Drop Shape Analyzer
SEM	Scanning Electron Microscopy
ECD	Equivalent Circle Diameter
mass-%	Mass percentage
wt. %	Weight percentage
ULC	Ultra Low Carbon
Ca-treated	Calcium treated

List of parameters

Chapter 1

ΔG	Free energy change for separation of a solid NMI at the refractory wall (N/m)
θ_1	Contact angle between a NMI and molten steel (deg.)
θ_2	Contact angle between a refractory and molten steel (deg.)
σ	Surface tension of molten steel (N/m)
F_A	Adhesion force (N)
ΔP	Difference pressure between the cavity and molten steel (Pa)
r_1	NMI radius (m)
r_2	Refractory radius (m)
R_1	Cavity geometry radii (auxiliary parameters) (m)
R'_2	Cavity geometry radii (auxiliary parameters) (m)
R_2	Cavity geometry radii (auxiliary parameters) (m)
α	Auxiliary angle (deg.)
L	Separation distance (m)
F_{vdW}	Van der Waals Force (N)
A_H	Hamaker constant (J)
F_B	Buoyancy force (N)
d_1	Inclusion diameter (m)
ρ_s	Density of the molten steel (kg/m^3)
ρ_1	NMI density (kg/m^3)
g	Gravity acceleration (m/s^2)
Re	Reynolds number
u_{avg}	Average flow velocity (m/s)
ϕ_{SEN}	SEN diameter (m)
υ	Kinematic viscosity of the steel (m^2/s)
x	Radial distance from the centerline of the SEN (m)
u_{avg}	Average velocity in the flow cross section (m/s)
u (x)	Velocity profile (m/s)
x	Radial distance from the centerline of the SEN (m)
u	Velocity (m/s)
y	Velocity from the wall (m)
u^*	Friction velocity (m/s)

τ_w	Shear stress (kg/ms^2)
μ	Dynamic viscosity of steel (kg/ms)
$\dot{u}$	Velocity gradient in the laminar layer (s^{-1})
δ	Thickness of the laminar sublayer (m)
u_δ	Velocity in the laminar layer (m/s)
u_{max}	Maximum steel velocity at the centerline of the SEN (m/s)
F_D	Drag force (N)
C_D	Drag coefficient for a spherical particle at the SEN wall
A_1	Projected area of the inclusion toward the flow direction (m^2)
u_r	Relative velocity between the inclusion and the molten steel at the inclusion's mass center (m/s)
Re_p	Particle Reynolds number
F_L	Lift force (N)
Re_G	Shear Reynolds number

Chapter 2

$F_{HT-LSCM}$	Attractive force from HT-LSCM experiments
m_1	Mass of the 'guest particle' (kg)
a_1	Acceleration of the 'guest particle' (m/s^2)
m_2	Mass of the 'host particle' (kg)
r_1	Radius of the 'guest particle' (m)
d_1	Length of the long axis (m)
d_2	Length of the short axis (m)
ρ_1	Density of 'guest particle'
ρ_G	Gas density (kg/m^3)
q^{-1}	Capillary length (m)
W	Energy of the system (J)
W_g	Gravitational energy (J)
W_w	Wetting energy (J)
W_m	Liquid meniscus energy (J)
ΔW	Interaction energy (J)
W_∞	Free energy when the two particles are far apart (J)
F_{cap}	Capillary interation force (N)
θ_k	Contact angle between NMI (k=1) or Ceramic-particle (k=2) and the liquid steel (deg.)
r_k	Radius NMI (k=1) or ceramic-particle (k=2) (m)
h_k	Height of the contact line for the NMI (k=1) or the ceramic-particle (k=2) (m)
Q_k	Capillary charge for NMI (k=1) or Ceramic-particle (k=2) (m)
c_k	Half of the contact line between NMI (k=1) and steel and between ceramic-particle and steel (k=2) (m)
γ_e	Constant of Euler-Masceroni
$K_0(x)$	Modified Bessel function of zero order
L	Interparticle distance (m)
$h_{k\infty}$	Height of the contact line for the NMI (k=1) or the ceramic-particle (k=2) far from the body (m)

$c_{k\infty}$	Half of the contact line between NMI (k=1) and steel and between ceramic-particle and steel (k=2) far from the body (m)
$\psi_{k\infty}$	Mensicus slope for the NMI (k=1) or the ceramic-particle (k=2) far from the body (m)
$K_1(x)$	Modified Bessel function of first order
$Q_{k\infty}$	Capillary charge for NMI (k=1) or ceramic-particle (k=2) far from the body (m)
D_k	Density ratio

Chapter 3

R_N	Normal ratio
R_p	Parallel ratio
F_F	Friction force (N)
F_n	Normal force (N)
κ_s	Coefficient of friction
R_T	Torque ratio
a	Contact radius (m)
K	Elastic constant (Pa)
ν_i	Poisson's ratio of a particle (i=1) and a refractory wall (2)
E_i	Young's modulus of a particle (1) and a refractory wall (2) (Pa)

Chapter 4

θ_a	Advancing contact angle (deg.)
θ_r	Receding contact angle (deg.)
θ_O	Static contact angle (deg.)
r_b	Equivalent bubble radius (m)
h	Height of the bubble (m)
a	Contact radius of the bubble (m)
F_S	Surface tension force (N)
V_b	Volume of the argon droplet (m^3)
ρ_b	Density bubble (kg/m^3)
$C_{D,ns}$	Drag coefficient for non-spherical particles at intermediate Reynolds numbers
C_D^*	Dimensionless Clift-Gauvin expression for the drag coefficient for shapes with circular cross section
C_{Shape}	Newton drag correction
Re_p^*	Corrected particle Reynolds number
E	Spheroid is defined by an aspect ratio
$d_{\parallel}$	Parallel diameter (m)
$d_{\perp}$	Normal diameter (m)
f_{shape}	Stokes correction factor for prolate spheroids
A_{surf}^*	Surface area ratio for a prolate spheroid (m^2)

F_C	Capillary force (N)
ω	Center-angle between the rear part of the attached sphere and three-phase contact line projection area on the sphere (deg.)
y	Immersed part of the NMI into the steel (m)
b	Contact radius between the NMI and the bubble (m)
h	Height of the cup.
A_1	Projected area towards the fluid flow
ρ_1	Density NMI (kg/m^3)
ρ_2	Density nozzle material (kg/m^3)
F_P	Capillary pressure in the bubble (N)
$F_{B,immersediGnas}$	Buoyancy force of the particle immersed in the gas (N)
$F_{B,immersedinSteel}$	Buoyancy force of the particle immersed in the steel (N)

Appendix A-H

G	Gibbs free energy of the gas cavity (J)
A_{sg}	Molten iron-gas area (m^2)
A_{ig}	Inclusion-gas area (m^2)
V	volume of the cavity (m^3)
P_o	Pressure in the molten iron $=1{,}013\cdot10^5$ Pa
N	Number of gas molecules inside the cavity = 0
$ß_i$	Half-filling angle, i=1,2 (deg.)
V_{S-S}	Volume of the cavity for sphere-sphere contact (m^3).
$A_{sg,S-S}$	Molten steel- gas area for sphere-sphere contact (m^2).
$A_{ig,S-S}$	Inclusion gas area for sphere-sphere contact (m^2).
V_{S-P}	Volume of the cavity for sphere-wall contact (m^3).
$A_{sg,S-P}$	Molten steel- gas area for sphere-wall contact (m^2).
$A_{ig,S-P}$	Inclusion gas area for sphere-wall contact (m^2).
V_1	Volume of the fluid in the cavity (m^3).
V_2	Volume of the NMI immersed in the bridge (m^3).
$ß_1$	Half-filling angle for the inclusion (deg.)
γi	i=1,2 (deg.)
α_1	i=1,2 (deg.)
σ_{i-r}	Surface tension between i-r inclusion-refractory, i-s inclusion-molten steel (N/m)
σ_{i-s}	Surface tension between i-s inclusion-molten steel (N/m)
σ_{r-s}	Surface tension between r-s refractory-molten steel (N/m)
σ_{s-g}	Surface tension between molten steel-gas (N/m)
σ_{S-s}	Surface tension between solid and molten steel (N/m)
σ_{s-g}	Surface tension between molten steel and gas (N/m)
θ_S	Contact angle of the solid phase (deg.)

$\sigma_{r\text{-}g}$	Surface tension between refractory-gas (N/m)
$\sigma_{i\text{-}g}$	Surface tension between i-g inclusions-gas (N/m)
I_i	i=1,2

List of figures

Apendix A-H

List of tables

Apendix A-H